Master's thesis

NTNU
Norwegian University of Science and Technology
Faculty of Natural Sciences
Department of Chemical Engineering

Vilde Gahr Sturtzel Lunde

Influence of Inorganic Nanoparticles on Drug Release from Stimuli-Responsive Nanogels

Master's thesis in Nanotechnology
Supervisor: Sulalit Bandyopadhyay
Co-supervisor: Karthik Raghunathan
July 2023

NTNU
Norwegian University of
Science and Technology

Vilde Gahr Sturtzel Lunde

Influence of Inorganic Nanoparticles on Drug Release from Stimuli-Responsive Nanogels

Master’s thesis in Nanotechnology
Supervisor: Sulalit Bandyopadhyay
Co-supervisor: Karthik Raghunathan
July 2023

Norwegian University of Science and Technology
Faculty of Natural Sciences
Department of Chemical Engineering

NTNU
Norwegian University of
Science and Technology

Abstract

Targeted drug delivery is a promising alternative to systemic cancer treatment, having the potential to improve the therapeutic effect and decrease side effects. Stimuli-responsive nanogels incorporated with inorganic nanoparticles are promising as drug carriers, having the ability to load large amounts of drugs that can be released in response to stimuli. However, there are challenges with obtaining a controlled release, currently limiting their clinical applicability. In this project, iron oxide nanoclusters and gold nanoparticles were incorporated into nanogels synthesized from acrylamide and acrylic acid to investigate the release in response to stimuli. The main objective was to obtain an externally controlled release. The heating efficiency of the magnetic nanoparticles was optimized and the stimuli-responsiveness of nanogels with different synthesis parameters was investigated. One hydrophobic and one hydrophilic model drug was loaded, and release experiments were conducted under both static and pulsed conditions. The effect of magnetic heating from iron oxide nanoparticles on the release was examined by applying an alternating magnetic field using the nanoTherics magneTherm.

Clinically relevant alternating magnetic field limits were used to obtain high heating efficiencies for the magnetic nanoparticles, presumably because of interactions between the particles in the clusters or reduced surface oxidation. All the nanogels collapsed in response to an increase in temperature, decrease in pH, and the combination of both, and were able to load both the hydrophobic and hydrophilic drug. Magnetic and optical properties of the inorganic nanoparticles were conserved when incorporated into the nanogels, but the incorporation of the magnetic nanoparticles proved challenging. Consequently, applying an alternating magnetic field did not increase the drug release. The release studies in the magneTherm were limited due to difficulties with the set-up, but there was generally a small increase in release upon externally changing the temperature and pH, and several studies had kinetics close to zero-order. Still, there was a high leakage of drugs in the absence of stimuli, resulting in unreliable release.

The experimental results suggest that the system has a potential for targeted drug delivery. However, there is a need for improved incorporation of the magnetic nanoparticles for increased heat generation and more release studies to obtain a more reliable system with a controllable release. These aspects should be the focus of potential future work.

Sammendrag

Målrettet medisinering er et lovende alternativ til systemisk kreftbehandling, som har potensiale til å øke den terapeutiske effekten og redusere bivirkninger. Stimuli-responsive nanogeler som er inkorporert med uorganiske nanopartikler er lovende legemiddeltransportører, da de kan laste store mengder legemidler som kan frigjøres som respons på stimuli. Imidlertid er det utfordringer knyttet til å kontrollere frigjøringen, noe som begrenser den kliniske anvendeligheten. I dette prosjektet ble jernoksid-nanoklynger og gullnanopartikler inkorporert i nanogeler som var syntetisert fra akrylamid og akrylsyre, for å undersøke frigjøringen som respons på stimuli. Hovedmålet for oppgaven var å kunne kontrollere frigjøringen eksternt. Varmeeffektiviteten til de magnetiske nanopartiklene ble optimalisert, og stimuli-responsen til nanogeler med ulike synteseparametere ble undersøkt. Ett hydrofobt og ett hydrofilt modell-legemiddel ble lastet, og frigjøringseksperimenter ble utført under statiske og pulserende forhold. Effekten av magnetisk oppvarming fra jernoksid-nanopartiklene på frigjøringen ble undersøkt ved bruk av et alternerende magnetfelt påført av en nanoTherics magneTherm.

De magnetiske nanopartikler hadde høy varmeeffektivitet ved bruk av klinisk relevante grenser for det alternerende magnetfeltet. Alle nanogelene kollapset som respons på økt temperatur, redusert pH og en kombinasjon av begge, og var i stand til å laste begge legemidlene. De magnetiske og optiske egenskapene til de uorganiske nanopartiklene var bevart etter inkorporering i nanogelene, men inkorporeringen av de magnetiske nanopartiklene var utfordrende. Som et resultat ble ingen økt frigjøring av legemiddelene observert ved bruk av det alternerende magnetfeltet. Frigjøringen i magneTherm var begrenset på grunn av utfordringer med oppsettet, men ekstern endring av temperatur og pH førte til en liten økning i frigjøringen, og ga en frigjøringskinetikk nær nulte orden. Likevel var frigjøringen upålitelig, med en betydelig lekkasje av legemidler i fravær av stimuli.

De eksperimentelle resultatene antyder at systemet har potensial for å bli brukt til målrettet legemiddellevering, men det er fortsatt behov for forbedret inkorporering av de magnetiske nanopartiklene for å oppnå økt varmegenerering, samt utføring av flere studier på frigjøringen for å oppnå et mer pålitelig system med mer kontrollert frigjøring. Disse aspektene bør være fokus for fremtidige undersøkelser.

Preface

This thesis was written as a conclusion to a Master of Science in Nanotechnology with a specialization in Nanotechnology for Materials, Energy and the Environment, at the Norwegian University of Science and Technology. The experimental work was carried out at Ugelstand Laboratory and the Particle Engineering Core fascilities at the Department of Chemical Engineering. The aim of this project was to investigate the different components in a targeted drug delivery system, and the drug release using different release mediums. The experimental work in this project was performed in the spring of 2023 and built on the work of the *TKP4570 Nanotechnology, specialization project* conducted on the same topic, which was performed in the fall of 2022. Certain parts of this work's theory and materials and methods sections are adapted from the thesis concluding the specialization project. All the experimental work in this master's project was performed by me, with the exception of the synthesis of gold nanoparticles and nanogels incorporated with the gold nanoparticles, which was performed by Karthik Raghunathan. The work was performed under the supervision of Professor Sulalit Bandyopadhyay and the cosupervision of Karthik Raghunathan.

VILDE GAHR STURTZEL LUNDE

Vilde Gahr Sturtzel Lunde
3rd July 2023

Acknowledgements

First of all, I want to thank my supervisors for their support in this project. I want to thank my supervisor Professor Sulalit Bandyopadhyay for his guidance, experimental suggestions, and valuable feedback. A huge thanks to my cosupervisior Karthik Raghunathan for taking the time for discussion, training, feedback, and consistently following up, even after he didn't have to anymore. Furthermore, thanks to the people in Ugelstad Lab and the Particle Engineering Core for instrumental training, help in the lab, suggestions, and academic discussions helping to bring different perspectives to my attention.

I also want to thank my friends and family for their support and encouragement, both academic and non-academic, through these years. I want to thank everyone in Timini Kull 18 for five fantastic years together. You are the most supportive and entertaining group of people I have ever known. Thank you for everything from sharing academic tips and tricks in every course we took together, to endless breaks, fun activities, and adventures, always keeping my motivation up. Thank you for helping us all finish this study program for social reasons and making it worth it. Thanks to Vilde for being my design consultant and making me the figures for this thesis illustrating the release set-ups. A particular thanks to Amalie for always taking the time to listen to my discussions and to play with me. And lastly and most importantly, a huge thanks to Andreas for an incredible emotional and scientific support. I owe you a big cake.

Acronyms and Symbols

Acronyms

AAc = Acrylic acid
AMF = Alternating magnetic field
AR = Aspect ratio
ATR = Attenuated total reflectance
AsA = Ascorbic acid
AuER = Etched gold nanorod
AuNP = Gold nanoparticle
BF = Bright field
BIS = N,N’-methylenebisacrylamide
CNT = Classical nucleation theory
Cyt C = Cytochrome C
CTAB = Cetrimonium bromide
DLS = Dynamic light scattering
DLVO = Derjaguin–Landau–Verwey–Overbeek
EE = Encapsulation efficiency
ELS = Electrophoretic light scattering
EM = Electromagnetic
FCC = Face-centered cubic
FDA = The United States Food and Drug Administration
FM = Ferrimagnetic
FTIR = Fourier transform infrared
ILP = Intrinsic loss power
IONP = Iron oxide nanoparticle
KPS = Potassium persulphate
LCST = Lower critical solubility limit
LE = Loading efficiency
LSPR = Localized surface plasmon resonance
MWCO = Molecular weight cut-off
MPS = Mononuclear phagocytic system
MQ = Milli-Q
MRI = Magnetic resonance imaging
NC = Nanocluster

NG = Nanogel
NS = Nanosphere
NIPAM = N-isopropylacrylamide
NIR = Near-infrared
NP = Nanoparticle
OA = Oleic acid
PDI = Polydispersity index
PMMA = Poly(methyl methacrylate)
PTA = Phosphotungstic acid
RPM = Rounds per minute
SA = Salicylic acid
SAR = Specific absorption rate
SDS = Sodium dodecyl sulfate
SPM = Superparamagnetism
S(T)EM = Scanning (transmission) electron microscope
TREA = Triethanolamine
TREG = Tri(ethylene glycol)
VCE = Volumetric collapse efficiency
VPTT = Volume phase transition temperature
VSM = Vibrating sample magnetometer

Symbols

μ = Chemical potential
μ_1 = Chemical potential dissolved species
μ_2 = Chemical potential crystal
μ_0 = Standard chemical potential
R = Gas constant
T = Temperature
S = Supersaturation
a = Activity
a^* = Activity at equilibrium
c = Concentration
c^* = Concentration at equilibrium
γ_a = Activity factor
ΔG = Change in free energy
ΔG_V = Change in volume free energy
ΔG_S = Change in surface free energy
ΔG^* = Energy barrier of nucleation
γ = Surface tension
V_m = Molecular volume
k_B = Boltzmann's constant
ν = Number of moles ions per mole solute
r^* = Critical radius
ΔG^*_{het} = Energy barrier of heterogeneous nucleation

ϕ = Contact angle factor
ΔG^*_{hom} = Energy barrier of homogeneous nucleation
c^*_{min} = Minimum concentration of nucleation
c_S = Minimum concentration of growth
V_{tot} = Electrostatic potential
V_R = Repulsive electrostatic potential
V_A = Attractive electrostatic potential
ζ = Zeta potential
d = Diameter
λ = Wavelength
$\epsilon(\omega)$ = Dielectric function
ϵ_1 = Real dielectric function
ϵ_2 = Complex dielectric function
ω = Frequency
ϵ_m = Medium dielectric constant
E = Electric field
α_p = Polarizability
σ_{sca} = Scattering
σ_{abs} = Absorbance
k = Wavevector
B = Magnetic flux density
$\mu_{0,B}$ = Permeability of vacuum
H = Magnetic field strength
M = Magnetization
μ = Magnetic moment
N = Number
V = Volume
χ = Susceptibility
L_m = Orbital angular momentum
S_m = Spin angular momentum
$\mu_{l,z}$ = Orbital angular moment
e = Elementary charge
m_e = Electron mass
m_l = Orbital magnetic quantum number
$\hbar$ = Reduced Planck's constant
$\mu_{s,z}$ = Spin magnetic moment
m_s = Spin magnetic quantum number
J_m = Total angular momentum
M_S = Saturation magnetization
d_{hyd} = Hydrodynamic diameter
D = Diffusion
η = Viscosity
$d_{swollen}$ = Hydrodynamic diameter of swollen NG
$d_{collapsed}$ = Hydrodynamic diameter of collapsed NG

pK_a = Acidic protonation constant
$L(x)$ = Langevin function
$M_{s,bulk}$ = Bulk saturation magnetization
τ_N = Néel relaxation time
τ_0 = Relaxation time constant
K = Magnetic anisotropy constant
V_{dry} = Dry volume
τ_B = Brownian relaxation time
V_{hyd} = Hydrodynamic volume
τ = Effective relaxation time
ρ = Density
f = Frequency
C_w = Specific heat capacity of water
m = Mass
c_0 = Concentration of drug added
c_{sup} = Concentration of drug in supernatant
c_{NG} = Concentration of nanogel
A = Absorbance
ϵ = Molar absorption coefficient
l = Length of path light
J = Flux
Q = Amount of released drug
Q_0 = Initial amount of drug
k_0 = Zero-order release constant
t = Time
k_1 = First-order release constant
α = Swelling ratio
d_0 = Diameter at 25 °C
L_{dry} = Dry length
d_{dry} = Dry diameter
M_R = Remnant magnetization
H_C = Coercivity
d_{mag} = Magnetic diameter
R^2 = Goodness of fit

Contents

List of Figures

Chapter 1

Introduction

Cancer is the leading global cause of mortality, characterized by uncontrolled cell growth, forming tumors [1]. Chemotherapy involves using drugs to target rapidly dividing cells and is frequently utilized in cancer therapy. However, chemotherapy lacks specificity and can result in severe side effects since it affects rapidly dividing cells in healthy tissue [2, 3]. Thus, more effective cancer treatments are needed. Targeted drug delivery is the selective delivery of drugs to the target site, giving improved therapeutic efficacy and reduced toxicity and side effects [3]. The approval of Doxil® by the United States Food and Drug Administration (FDA) in 1995 marked a breakthrough in this field, being the first cancer nanomedicine administered through targeted drug delivery [4]. In targeted drug delivery, a carrier can transport the drug to the target site while protecting it from physical and chemical degradation and the clearance systems in the body. Inorganic nanoparticles (NPs) [5], polymer NPs [6], lipids [7], and colloidal hydrogel particles in the nano size-range, also known as nanogels (NGs) [8], have been extensively researched as carriers.

Stimuli-responsive NGs are promising drug carrier candidates due to their ability to load large amounts of drugs and selectively release them in response to external stimuli [8]. The pH-responsive monomer acrylic acid (AAc) and the temperature-responsive monomer N-acrylamide (NIPAM) can provide stimuli-responsiveness to NGs, which can be utilized to release a loaded drug upon exposure to the acidic environment in tumors and endosomal compartments [9], or optical or magnetic heating.

Superparamagnetic (SPM) iron oxide nanoparticles (IONP) can generate heat when subjected to an alternating magnetic field (AMF) due to relaxation mechanisms. Thermal decomposition is commonly used to synthesize SPM IONPs with precise control over the size, size distribution, and crystallinity, allowing control over the magnetic properties and heating efficiency. NPs synthesized through thermal decomposition are generally only dispersible in organic solvents. However, utilizing a hydrophilic organic solvent like tri(ethylene glycol) (TREG), they become dispersible in aqueous solutions [10]. Alternatively, the inclusion of triethanolamine (TREA) in addition to TREG can result in the formation of nanoclusters (NC) with high heating efficiencies [11].

Gold nanoparticles (AuNPs) have size- and shape-dependent optical properties, making them desirable for imaging, sensors, and targeted drug delivery applications. AuNPs that absorb electromagnetic (EM) irradiation in the near-infrared region (NIR) can generate heat by a phenomenon called the photothermal effect [12]. Both these magnetic and optical heating phenomena can be utilized in hyperthermia cancer treatment or targeted drug delivery to trigger a drug release when the IONPs or AuNPs are incorporated into temperature-responsive NGs [4].

The aim of this study was to achieve a controlled drug release using external stimulus in the form of an AMF. To achieve this objective, a targeted drug delivery system was synthesized by combining the stimuli-responsive properties of NGs with the heating properties of IONPs or AuNPs. The focus was on understanding the components of the system and their interactions as well as their influence on drug release under relevant physiological conditions.

Stimuli-responsive NGs were synthesized through co-precipitation polymerization of NIPAM and AAc. IONPs and AuNPs were incorporated into the NGs, and the hydrophobic molecule salicylic acid (SA) and the hydrophilic protein Cytochrome C (Cyt C) were utilized as model drugs to investigate the loading and release properties of the NGs. SA was selected due to its similarity in molecular weight to many cancer drugs and its distinct absorbance peak in the UV-Vis spectrum, as well as its partial solubility in water [13, 14, 15]. Cyt C is commonly used as a model drug [16], and was selected to enable a comparison of the drug loading of a hydrophobic and hydrophilic drug. The drug release was studied in both static and pulsed release mediums. Furthermore, the release of the NGs incorporated with IONPs was studied under the influence of an AMF.

Various techniques were employed to characterize the NGs and IONPs to understand their properties. These include scanning (transmission) electron microscopy (S(T)EM) for determining the dry size and shape, dynamic light scattering (DLS) for colloidal size, ZetaSizer for evaluating particle stability based on zeta potential, vibrating sample magnetometer (VSM) for measuring the magnetization curve of IONPs, and magneTherm for analyzing their heating properties. A Langevin fitting was performed on the VSM results to estimate the magnetic size of the IONPs. Fourier transformation infrared spectroscopy (FTIR) was used to analyze the chemical bonding, and UV-Vis spectroscopy was used to characterize the drug loading and release. A magneTherm coupled with a UV-Vis was utilized to study the real-time effects of pH, temperature, and AMFs on drug release.

Chapter 2

Theory and Literature Review

This section is divided into the theory and the literature review. The theory covers the theoretical foundation needed to understand the work performed in this project. This includes the optical properties of gold nanoparticles, the magnetic properties of iron oxide nanoparticles, and the stimuli-responsiveness of certain nanogels. The literature review discusses previously reported studies in these fields for the application of targeted drug delivery. The theory begins with an introduction to the fundamental principles of crystallization, as explained by the classical nucleation theory (CNT).

2.1 Crystallization

The CNT explains crystallization through thermodynamics, as the formation of a crystalline material through the assembly of monomeric units. Properties like composition, shape, surface charge, size, polydispersity, and crystallinity can be tuned by controlling the crystallization process. For example, magnetic properties are often strongly influenced by the crystallinity, i.e., the degree of the long-range ordering of the atoms in the lattice [17]. Consequently, understanding the process is crucial for precisely controlling these properties, especially for particles intended for biomedical applications [18]. The crystallization process with a focus on the synthesis of gold and magnetic nanoparticles for biomedical applications will now be presented. [19]

2.1.1 Nucleation and Growth

Crystallization is a phase transformation driven by the reduction of free energy. In solution, this can be expressed as the difference in chemical potential between the two phases, as

$$\Delta\mu = \mu_1 - \mu_2 \tag{2.1}$$

where μ_1 and μ_2 are the chemical potentials of the substance in the solution and in the solid phase, respectively. The chemical potential can be represented as

$$\mu = \mu_0 + RT\ln(a) \tag{2.2}$$

where μ_0 is the standard chemical potential, R is the gas constant, T is the temperature, and a is the activity. Combining Equations 2.1 and 2.2, one can write

$$\frac{\Delta\mu}{RT} = \ln\left(\frac{a}{a^*}\right) = \ln(S) \tag{2.3}$$

where a^* is the equilibrium activity and S is the supersaturation. The a is the effective concentration in the system and is used instead of the concentration for real and non-ideal solutions. It is defined by correcting the concentration, c, with the activity factor, $a = \gamma_a c$. The value of a depends on the interactions in the solution and becomes close to c for dilute solutions. Consequently, the supersaturation can be expressed as

$$S = \frac{a}{a^*} \sim \frac{c}{c^*} \tag{2.4}$$

where c^* is the equilibrium concentration. The supersaturation gives the tendency of the system to precipitate, and for a supersaturated system, $S > 1$. [19]

The solubility of a solid in a solution depends on the temperature. At constant temperature, an increased concentration can supersaturate the system. This is illustrated in Figure 2.1 as moving vertically up from the stable zone, crossing the solubility curve, and entering the metastable zone. Here, the system can lower its energy by forming an ordered system, i.e., spontaneously undergoing crystallization. Further increasing the concentration of the species in the solution, the system crosses the supersolubility curve and enters the labile zone. Here, crystallization can happen rapidly and is challenging to control. [19]

The monomeric units in a supersaturated system will constantly collide and come apart. The total free energy, ΔG, is a sum of the bulk free energy and the surface free energy, $\Delta G = \Delta G_V + \Delta G_S$. ΔG_V arises from the supersaturation of the system and is lowered by precipitation, while ΔG_S comes from the energy cost of creating a new surface and works against precipitation. When the precipitates reach a certain size, ΔG reaches a maximum, called the critical energy. This is the energy barrier of nucleation. The radius of the precipitates reaching the critical energy is called the critical radius and is given by

$$r^* = \frac{2\gamma V_m}{\nu k_B T lnS} \tag{2.5}$$

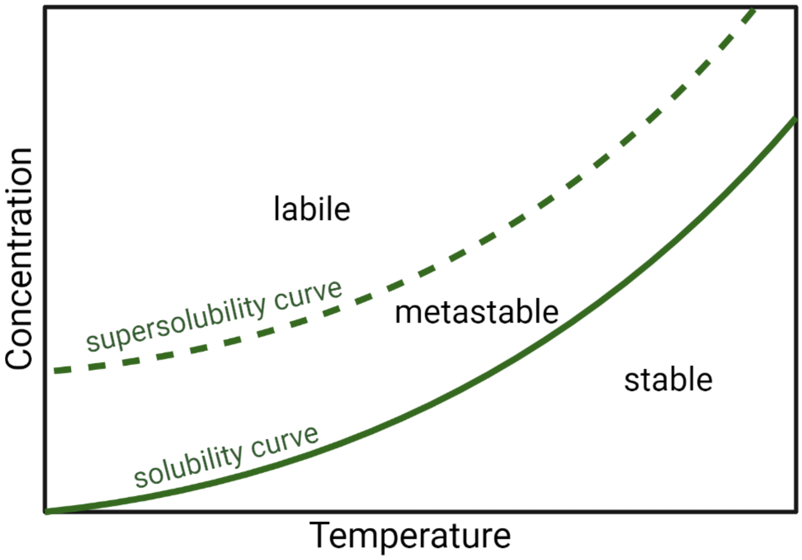

Figure 2.1: The stable, metastable, and labile zone, defined from the temperature and concentration of monomeric units in the system. The zones are separated by the solubility and supersolubility curves, respectively. Nucleation can occur in the metastable and labile zones. Figure created with Biorender [20] and adapted from Mullin [19].

and the critical energy is found when the first derivative of ΔG with respect to r is equal to zero:

$$\Delta G^* = \frac{16\pi\gamma^3 V_m^2}{3k_B^3 T^3(\nu \ln(S))^2} \tag{2.6}$$

where γ is the interfacial tension between liquid and solid, V_m is the molecular volume, k_B is Boltzmann's constant, and ν is number of moles ions per mole solute. The precipitates overcoming the critical energy will phase separate out of the solution and form nuclei. This process is called nucleation and is the first step of crystallization. The rate at which this happens is called the nucleation rate and increases with increasing S. [19, 21]

Nucleation can be classified into homogeneous and heterogeneous nucleation. Homogeneous nucleation is the process of monomeric units coming together in a supersaturated solution, which has just been explained. On the other hand, in heterogeneous nucleation, a surface is introduced to the medium, lowering the energy barrier of nucleation, as illustrated in Figure 2.2. Despite the difference in ΔG^* between the two processes, the r^* is the same. The relationship between the free energies can be expressed by $\Delta G^*_{het} = \phi \Delta G^*_{hom}$, where ϕ is a factor between zero and one and depends on the contact angle between the particle and the solution. Heterogeneous nucleation has a lower critical energy due to the smaller surface area needed for nucleus formation and the lower interfacial energy between particles compared to liquid-solid phases. Heterogeneous nucleation can be induced through seeding, where small particles of the same material that is intended to be crystallized are added into the supersaturated solution. [19]

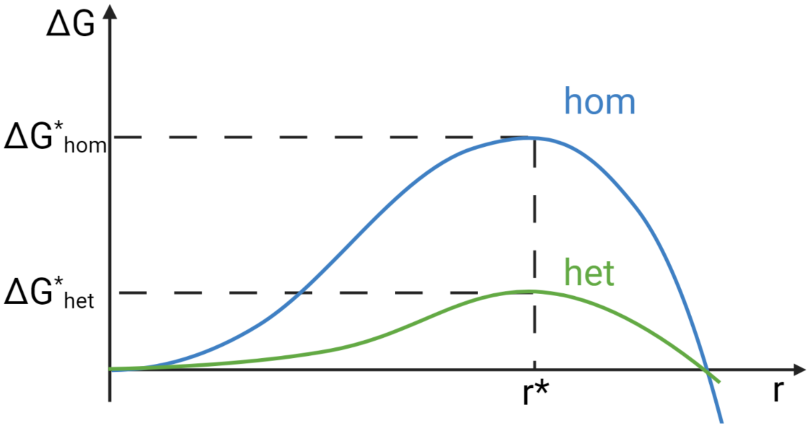

Figure 2.2: The free energy of homogeneous and heterogeneous nucleation as a function of the precipitate radius. The critical radius is the same, while the critical energy is significantly higher for homogeneous nucleation. Figure created with Biorender [20] and adapted from Bandyopadhyay [21].

The system will remain dynamic after the first nuclei are formed, with attachment and detachment of building units happening continuously. The attachment rate depends on the monomeric unit concentration, while the detachment rate depends on temperature and the bonding strength between the monomeric units. If the system remains supersaturated, growth of the nuclei occurs if the attachment rate exceeds the detachment rate. According to the CNT, growth happens via monomer addition, i.e., incorporation of monomeric building units into the nuclei. This process is driven by the lowering of energy, as the monomeric units in the solution possess higher energy compared to those incorporated into the solid. The growth rate increases with increasing S, similarly to the nucleation rate. [19]

The state with the lowest energy is considered to be thermodynamically stable. However, metastable phases with lower energy barriers may form initially due to kinetic factors, delaying the formation of the stable form. This phenomenon is described by Ostwald's rule of stages and explains why amorphous phases may form instead of crystalline phases. Magnetite is an example of a thermodynamically stable form of iron oxide that does not necessarily initially form. [19]

2.1.2 Size and Size Distribution

The properties of NPs are strongly size-dependent as a result of their high surface-to-volume ratio. As an example, AuNPs have interesting optical properties when the particle diameter is less than the wavelength of incoming irradiation [12], while magnetite goes from ferrimagnetic to superparamagnetic when the particle size is sufficiently reduced [22]. Additionally, the size of NPs intended for drug delivery applications should be above 10 nm and below 200 nm to avoid being removed by the glomerular filtration barrier or the mononuclear phagocytic system (MPS), respectively [4]. Consequently, sufficient control over the NP size and size distribution is essential.

The LaMer diagram, illustrated in Figure 2.3, is useful for understanding how the size and size distribution of NP populations can be controlled. The diagram shows an example of how the monomer concentration in a system can change with time, dividing the process into the prenucleation zone (I), nucleation zone (II), and growth zone (III). The minimum concentrations needed for nucleation and growth are denoted c^*_{min} and c_S, respectively. In zone I, the monomeric units are generated, and the concentration increases as no nucleation can occur. Entering zone II, supersaturation is established and the critical energy of nucleation is overcome, resulting in the generation of nuclei. Once nuclei are generated, subsequent growth can occur. Since both the nucleation and growth processes consume monomeric units, the monomer concentration decreases if no new units are introduced. Moving below c^*_{min}, only growth can occur in zone III until c_S is reached. This diagram shows a simplified crystallization process, and the different steps will realistically overlap. [23]

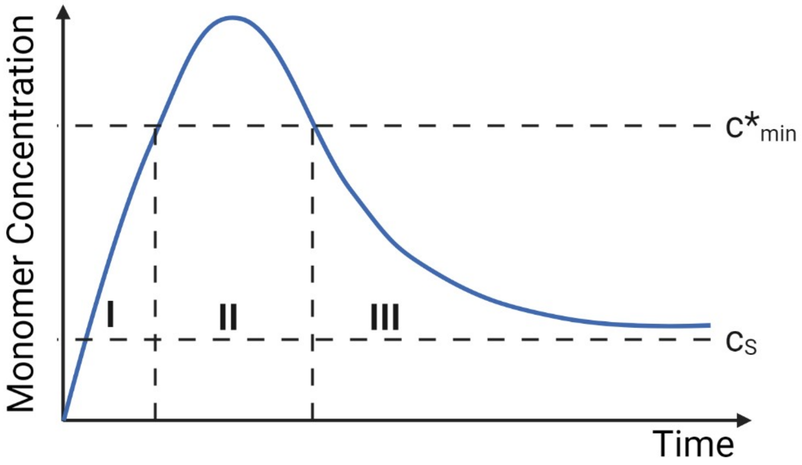

Figure 2.3: LaMer diagram representing a simplified kinetic formation of nanoparticles. The process is divided into the prenucleation zone (I), nucleation zone (II), and growth zone (III). c^*_{min} and c_S are the minimum concentrations for nucleation and growth to occur, respectively. Diagram adapted from LaMer [24] and made using Biorender [20].

The relative nucleation and growth rates determine the final particle size, as the nucleation and growth mechanisms compete over monomeric unit consumption. Consequently, a dominating nucleation rate will result in more monomeric units being consumed by generating new nuclei, resulting in many small particles. On the other hand, a dominating growth rate will lead to more monomeric units being consumed by existing particles and result in larger particles. Supersaturation is an important factor influencing these relative rates. Only growth can occur at low supersaturation, between c^*_{min} and c_S, while a high supersaturation will result in a high nucleation rate. Kinetic factors like capping agents can also influence particle size through spatial confinement. [23]

A narrow size distribution gives particles with similar properties and is desirable for many applications. This can be achieved by separating the nucleation and growth processes, for example by rapidly generating a high supersaturation to form nuclei, and then lowering the supersaturation below c^*_{min} to prevent further nucleation. Simultaneously generating all the nuclei ensures they are formed under the same conditions, leading to similar subsequent growth processes and uniform particle size. [23]

2.1.3 Morphology

The NP morphology also affects its properties, and results from the relative growth rates of the particle faces, where a difference in growth rates will result in anisotropic particles. Both internal and external factors can influence these rates. [19]

Internal factors result from intrinsic properties, like the crystal structure and bonding. Certain facets will have a higher roughness and more kink sites. This results in more available bonds, leading to a higher surface energy and faster growth. The Wulff construction is a theoretical model of the equilibrium morphology of a crystal depending on pressure and temperature but no other external factors. The construction is based on the relative energies of the different faces and gives the morphology that minimizes the overall surface energy. [19]

Also external factors like supersaturation and additives influence the final shape of the particle. Well-faceted crystals with a shape close to the one predicted by the Wulff construction can be formed at lower supersaturation. However, if the supersaturation is high, monomeric units will be incorporated into all facets, not only the ones with the highest energy. Furthermore, additives like site-specific capping agents can adsorb onto high-energy facests and inhibit growth. The final morphology depends on both internal and external factors. External growth factors are most dominating, so different reaction conditions give differently shaped particles. [19]

2.1.4 Stability

Their high surface-to-volume ratio makes NPs colloidally unstable and prone to aggregate as a result of their high surface energy. To avoid this, the particles must be stabilized. Stability is crucial for drug delivery applications of NPs to ensure sufficient circulation time, and because aggregated particles in the body can form blood clots [4]. Stabilization is achieved by introducing an energy barrier that prevents the particles from aggregating through kinetic stability, and is mainly done by electrostatic or steric stabilization. [25]

The DLVO (Derjaguin–Landau–Verwey–Overbeek) theory describes electrostatic stabilization as the introduction of equal electric charge to the particle surface. This results in repulsive Coulomb forces counteracting the attractive van der Waals forces and can be represented as $V_{tot} = V_R + V_A$. The zeta potential (ζ) is the electric potential at the Stern layer surrounding the particle. A higher ζ indicates higher electrostatic stability. However, there are potential challenges associated with the use of charged NPs in the body. For instance, strongly negative particles repel the negatively charged cell membrane, hindering endocytosis, while strongly positive particles may interact too strongly with the cell membrane, causing damage. Additionally, the immune system more easily recognizes positive particles due to faster opsonization. [4, 18, 25]

Functionalizing polymers onto particle surfaces can create steric stabilization due to the steric hindrance that prevents particles from coming close enough to aggregate. Sufficient coverage of the surface will prevent opsonization, as opsonins absorb to the naked particle surface. [18, 23, 25]

2.2 Optical Properties of Gold Nanoparticles

Certain metallic NPs exhibit interesting optical properties, with AuNPs being an important example. In this section, the theoretical background for these properties will be presented.

When the AuNP diameter becomes much smaller than the wavelength of incoming EM irradiation, $d \ll \lambda$, all the surface electrons will experience a uniform EM field. This is called the quasi-static approximation and is generally valid for particles with dimensions less than 100 nm [26]. Due to their high surface-to-volume ratio, AuNPs have a large number of conduction electrons on their surface. These electrons will interact and form an electron cloud which can absorb the incoming EM radiation and be displaced relative to the center of the particle, as illustrated in Figure 2.4. Restoring Coulomb forces will pull the electron cloud back, causing coherent oscillation. Resultingly, there is a high extinction in the incoming EM irradiation. At certain frequencies, these oscillations result in resonance, and this effect is called localized surface plasmon resonance (LSPR). [12]

A spherical particle of diameter d fulfilling the quasi-static approximation will have a dielectric function $\epsilon(\omega)$, where ω is the frequency. If the particle is surrounded by a non-absorbing and isotropic medium with a dielectric constant ϵ_m, the particle will have a polarizability upon the application of a static EM field, expressed as

$$\alpha = 4\pi d^3 \frac{\epsilon(\omega) - \epsilon_m}{\epsilon(\omega) + 2\epsilon_m} \tag{2.7}$$

representing the response of the electron cloud to the field. There is a high extinction

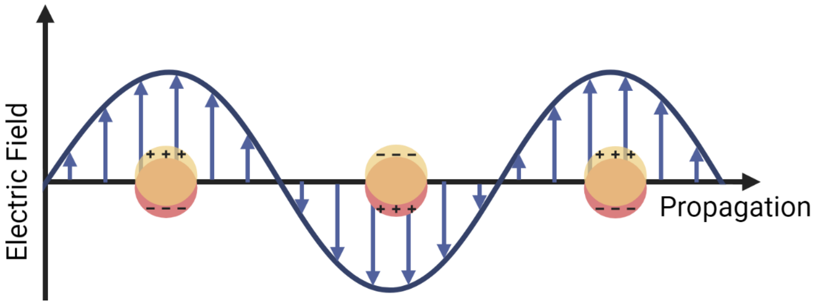

Figure 2.4: Displacement of the surface electrons of an AuNP upon EM irradiation, forming a dipole. Figure adapted from Kelly et al. [26] and created with Biorender [20].

when $\mathrm{Re}[\epsilon(\omega)] = -2\epsilon_m$, as the polarizability of the electron cloud diverges. Damping processes, anisotropy, and particle interactions will lead to minor corrections to the expression. The extinction is given by the sum of the scattering and absorbance. These are individually defined as

$$\sigma_{sca} = \frac{k^4}{6\pi}|\alpha|^2 \tag{2.8}$$

$$\sigma_{abs} = k\,\mathrm{Im}(\alpha) \tag{2.9}$$

where k is the wavevector of the EM radiation. The resonance condition is the same as before and is fulfilled at a specific frequency called the dipole plasmon resonance. This depends on the type of metal, size, shape, surface functionalization, and chemical environment [26]. AuNPs generally exhibit a high extinction coefficient within the visible light region due to their LSPR properties. The maximum absorbance is typically found at higher wavelengths, i.e., smaller energies, for larger particles due to charge separation. Applications of AuNPs are generally based on this resonance wavelength, like imaging and biosensing. [12]

Another important application of AuNPs is the ability to generate heat when the absorbance maximum is in the NIR region of the EM spectrum [4]. This is called the photothermal effect and will be elaborated in the literature review. As an alternative, the magnetic properties of IONPs can be used to generate heat.

2.3 Magnetic Properties of Iron Oxide Nanoparticles

In this section, the theoretical background for the magnetic properties of IONPs will be presented using a macroscopic and microscopic description. The macroscopic description relates a material response upon the application of an external field. The magnetic flux density in a material upon an applied magnetic field, $\boldsymbol{H}$, is given by

$$\boldsymbol{B} = \mu_{0,B}(\boldsymbol{H} + \boldsymbol{M}) \tag{2.10}$$

where $\mu_{0,B}$ is the permeability of vacuum, and $\boldsymbol{M}$ is the macroscopic magnetization of the material. The bold letters are used to indicate vectors. In vacuum, $\boldsymbol{M} = 0$, leading to $\boldsymbol{B} = \mu_0\boldsymbol{H}$. The magnetization is the number N of magnetic moments $\boldsymbol{\mu}$ per volume V:

$$\boldsymbol{M} = \boldsymbol{\mu}\frac{N}{V} \tag{2.11}$$

A parallel alignment of the magnetic moments will result in increased magnetization, while oppositely aligned moments will cancel each other out. The susceptibility is defined as $\chi = \boldsymbol{M}/\boldsymbol{H}$, and is a dimensionless quantity which describes the magnetization in response to an applied field. [27]

The formation of solid crystalline materials was presented in Section 2.1 through the crystallization process. The magnetic behavior of crystalline materials is determined by the arrangement of the magnetic moments associated with the atoms or ions in the crystal lattice. The collective behavior of these magnetic moments can result in different types of magnetic ordering. Consequently, the crystallinity of the material will greatly affect its magnetic properties. To describe magnetism at a microscopic level, it is necessary to consider the atomic structure. One can simplify by considering an atom with a single orbiting electron. The nucleus will possess a magnetic moment due to nuclear spin. However, the magnitude scales inversely with the mass, resulting in the nuclear magnetic moment often being one-hundredth to one-thousandth of the electronic magnetic moment, and is generally neglected. Consequently, magnetic contributions are attributed to the electrons. [27]

An atom will have a magnetic moment as a result of the orbital angular momentum $\boldsymbol{L_m}$ and the spin $\boldsymbol{S_m}$ of the electrons, giving rise to the orbital magnetic moment $\boldsymbol{\mu_l}$ and spin magnetic moment $\boldsymbol{\mu_S}$, respectively. A quantum mechanical description is used due to the quantized energy levels of the electrons. The electron precession around the nucleus will give rise to the orbital magnetic moment

$$\boldsymbol{\mu_l} = -\frac{e\hbar}{2m_e}\boldsymbol{L_m} \tag{2.12}$$

where e is the elementary charge, $\hbar$ is the reduced Planck's constant, m_e is the electron mass. The spin is an intrinsic electron property which can be expressed as:

$$\boldsymbol{\mu_s} = -\frac{e\hbar}{m_e}\boldsymbol{S_m} \tag{2.13}$$

The orbital and spin moments are not independent properties, but interact with each other. The total angular magnetic moment, denoted $\boldsymbol{J_m}$, is the sum of the orbital and spin magnetic moments. Since the moments have a direction, there must be an asymmetry in the electron distribution for the electrons to possess a net magnetic moment that does not cancel out. Consequently, atoms with fully filled electron levels do not exhibit a magnetic moment. For the rest of this work, the vector notation will not be used, since the direction of the vectors will not be considered. [22, 27, 28]

The chemical formula of magnetite is Fe_3O_4, where the O^{2-} ions have a completely filled outer electron shell and do not have a magnetic contribution. Fe_3O_4 has an inverse spinel structure, with an equal number of Fe^{3+} and Fe^{2+} ions occupying the octahedral sites, and the remaining half of Fe^{3+} ions occupying the tetrahedral sites. The ions occupying the octahedral and tetrahedral sites have antiparallel magnetic moments, making the moments of the Fe^{3+} ions cancel each other out. This leaves a net moment attributed to the Fe^{2+} ions. This magnetic arrangement of two sublattices with opposite magnetic orientations but unequal strength is known as ferrimagnetism (FM). [22]

The magnetic moments in FM materials align parallel or antiparallel to an easy axis of magnetization. Flipping the magnetic moment from one direction to the opposite requires overcoming an energy barrier. The FM alignment is not continuous throughout the crystal but is split into domains with different directions, where the size of these depends on the balance between the domain wall energy and the demagnetization energy. Below a certain size, the domain wall energy becomes dominating and makes the particle a single domain. This is estimated to be the case for magnetite particles below 100 nm. Further reducing the particle size leads to the energy barrier for flipping the magnetic moments becoming smaller than the thermal energy at room temperature. As a result, the magnetic moments of the particles undergo rapid thermal fluctuations, giving a zero net measured magnetization in the absence of an external magnetic field. This is defined as superparamagnetism. [22]

SPM NPs obtain a magnetization parallel to an applied magnetic field, as illustrated in Figure 2.5. The magnetization increases until reaching a maximum value, i.e., the saturation magnetization, M_S. When the field is turned off, there is no remnant magnetization, as illustrated by the lack of hysteresis in the curve, due to the rapid relaxation of the magnetic moments once the field is turned off [28]. This relaxation results in a heat generation. This heat can be utilized to can induce conformational changes in temperature-responsive NGs. [22]

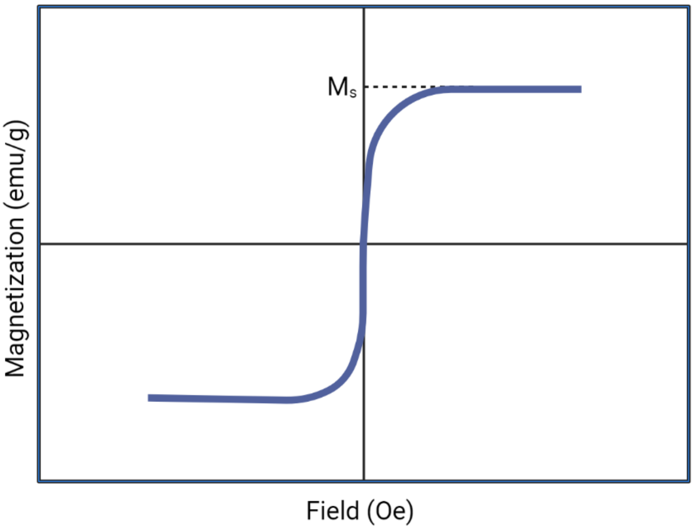

Figure 2.5: The magnetization of superparamagnetic particles upon applying an external magnetic field. M_S is the saturation magnetization. Figure created with Biorender [20].

2.4 Stimuli-Responsive Nanogels

Hydrogels are three-dimensional cross-linked networks of polymers that can reversibly absorb large amounts of water due to hydrophilic functional groups [4]. Nanogels are hydrogel particles with nano-scale dimensions, defined as under 200 nm [9]. Due to the high water content of NGs, their size is challenging to characterize using electron microscopy. However, their hydrodynamic diameter, d_{hyd}, can be characterized using DLS, where the intensity of scattered light is measured as a function of time. Using an auto-correlation function, the changes in the intensity are used to calculate the diffusion (D) from the decay of the auto-correlation function [21]. The d_{hyd} of the particles is then found using the Stokes-Einstein equation:

$$D = \frac{k_B T}{3\pi\eta d_{hyd}} \tag{2.14}$$

where η is the viscosity of the medium. Note that the technique assumes spherical particles [29]. Certain NGs can respond to external stimuli by collapsing, and this property can be used to release a loaded drug. The ability of a stimuli-responsive NG to undergo collapse is characterized using the volumetric collapse efficiency (VCE), given by

$$\text{VCE}[\%] = \frac{d_{swollen}^3 - d_{collapsed}^3}{d_{swollen}^3} \cdot 100 \tag{2.15}$$

where $d_{swollen}$ is the hydrodynamic diameter of the swollen NGs, while $d_{collapsed}$ is the hydrodynamic diameter of the collapsed NGs [21, 30]. Due to their physiological relevance, two common stimuli of particular interest for biomedical applications are changes in pH and temperature. [21]

2.4.1 pH-Responsive Nanogels

The pH within the human body varies across organs, tissues, and physiological conditions. For instance, the pH is around 7.4 in healthy tissue, between 5.8 and 7.2 in extracellular tumor environments, and around 5.5 in endosomal compartments [4, 9]. Therefore, NGs responding to low pH can utilize physiological pH gradients to deliver cargo when in the presence of a tumor or internalized by a cell.

The responsiveness of an NG is a result of the properties of its monomeric constituents. Consequently, pH-responsive NGs can be synthesized using monomers with acidic groups, such as AAc with a pK_a of 4.3 [30]. At higher pH values, the carboxylic functional groups will deprotonate and attribute a negative charge. This will cause electrostatic repulsion between the groups, causing the NGs to swell [8]. On the other hand, at pH below pK_a, the carboxylic groups are protonated, and the NGs will collapse. [21]

2.4.2 Temperature-Responsive Nanogels

Temperature-responsive NGs are well-suited for biomedical applications due to their ability to respond to temperature gradients, which are naturally present in biological systems due to physiological processes or pathological conditions. Moreover, the temperature can be externally increased by AuNPs exposed to EM irradiation or SPM NPs exposed to an AMF [8, 18].

Temperature-responsive NGs can be synthesized from polymers with temperature-dependent solubility. The lower critical solution temperature (LCST) of a polymer is defined as the temperature that the polymer is soluble below and insoluble above. One commonly used temperature-responsive polymer is pNIPAM, which has an LCST close to 32 °C [8, 9]. Below the LCST, the polymer-solvent interactions dominate, and the amide groups of pNIPAM form hydrogen bonds with the surrounding water [8]. Above the LCST, polymer-polymer interactions dominate, and the polymer undergoes a coil-to-globule transition, driven by the entropy-favored release of the water molecules [8]. The volumetric phase transition temperature (VPTT) of NGs is analogous to the LCST of polymers. At temperatures below the VPTT, the NGs are hydrophilic and swollen, but above the VPTT they become hydrophobic and collapse, driven by the reduction of Gibbs free energy. The VPTT is defined at a single temperature by convention but is realistically most often a temperature range due to nonuniform chain lengths. NIPAM NGs typically exhibit a slightly higher VPTT than their polymer counterparts. [4, 21, 31, 32]

Note that the mechanisms for temperature- and pH-induced collapse are different, which will affect the properties of the collapsed NGs. For example, for temperature-induced collapse, the charge per NG will be constant, increasing the electrophoretic mobility and ζ. On the other hand, for pH-induced collapse, the charge per NG will change due to the protonation of functional groups [8]. A dual stimuli-response can be obtained through copolymerizing pH- and temperature-dependent monomers. The subsequent sections will elaborate on the use of such NGs in drug delivery applications.

2.5 Targeted Drug Delivery Systems

The theoretical foundation needed to understand the properties of AuNPs, IONPs, and stimuli-responsive NGs has now been presented. The following section is a literature review that will focus on the application of these particles in a hybrid targeted drug delivery system.

2.5.1 Gold Nanoparticles for Biomedical Applications

There is controversy regarding the cytotoxicity of AuNPs, which poses a challenge for their use in biomedical applications. Some studies have found AuNPs to be non-toxic for sizes between 14 and 100 nm [33], while another study found the uptake of 14 nm AuNPs into cells to damage internal cell activities [34]. Therefore, the toxicity of AuNPs must be considered a possibility and is found to depend on physiochemical properties, like size and concentration [35, 36], and surface charge and functionalization [37, 38]. In general, smaller AuNPs and larger concentrations have been found to have increased toxicity, and anionic particles are considered more toxic than neutral or cationic ones [35, 37]. Gold nanorods are anisotropic nanostructures which have shown longer circulation time in the human body than gold spheres [18]. Controlling these parameters is therefore crucial when synthesizing AuNPs for biomedical applications. Furthermore, the size and morphology are essential for their optical properties.

Synthesis of Gold Nanoparticles

AuNPs are often synthesized using a reducing agent to reduce an ionic metallic precursor to an elemental form and a passivating ligand to stabilize and introduce functional properties [23]. Different shapes can be achieved through seeded growth by tuning the reaction parameters, and etched nanorods (AuER) can be synthesized using a binary surfactant mixture of cetrimonium bromide (CTAB) and oleic acid (OA) [39].

Chloroauric acid ($HAuCl_4$) is a commonly used precursor for AuNPs, where the gold is present in Au^{3+} ions [21]. Strong reducing agents have a high reduction potential, and generate high S compared to weak reducing agents, generally resulting in smaller particles, as explained in Section 2.1.2 [23]. Ascorbic acid (AsA) is a weak reducing agent and is only able to reduce gold from Au^{3+} to Au^{+}, which is insufficient for homogeneous nucleation to occur. However, as mentioned in Section 2.1.1, heterogeneous nucleation has a lower energy barrier, and can be achieved through seeded growth, by the addition of Au^0 seeds formed using a strong reducing agent like $NaBH_4$. [39]

AuNPs have a face-centered cubic (FCC) unit cell crystal structure, which means {111} have the highest packing density, {100} have intermediate packing density, and {110} have the lowest packing density. As the surface energy increases inversely with the packing density, this leaves {110} with the highest surface energy [23]. As explained in Section 2.1.3, this will favor anisotropic structures. However, the final morphology will also be influenced by external factors, such as surface-directing agents like CTAB, which preferentially binds onto {110}, making growth preferentially happening on the {100} facets, leading to the formation of rods [40, 41, 42]. CTAB also stabilizes the particles, slowing the overall growth and preventing aggregation and ripening, resulting in smaller particles. However, a drawback with CTAB is its cytotoxicity [41]. The molecular structure of CTAB is shown in Figure 2.6, where the tail is hydrophobic and the head is hydrophilic [41]. The use of binary surfactant mixtures can also influence the shape of the particles. As an example, using OA as a co-surfactant with CTAB results in shapes such as rods, etched rods, and nanomakura [39]. Additionally, silver-assisted growth through the addition of silver nitrate ($AgNO_3$) has resulted in more anisotropic particles and increased shape selectivity [21].

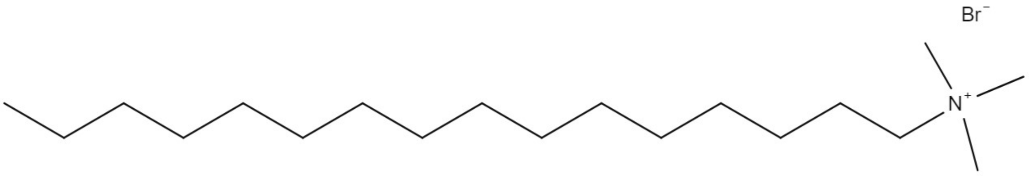

Figure 2.6: Molecular structure of CTAB.

The Photothermal Effect

AuNPs irradiated with EM irradiation at their resonance frequency will have a high scattering and absorbance, as explained in Section 2.2. This property is useful for imaging the particles. The absorbance phenomenon can also generate heat, which can be utilized by combining the AuNPs with temperature-responsive NGs. Anisotropic AuNPs generally have a larger extinction coefficient and scatter more light than spherical AuNPs. Furthermore, anisotropic particles will have multiple LSPR peaks, corresponding to the different axes. Depending on the chemical environment, the longitudinal mode of highly anisotropic AuNPs can have a maximum absorbance in the NIR part of the EM spectrum. i.e. between 650 and 900 nm [4, 43]. This is the 'optical window' of biological tissue [44], where there is less absorption from the constituents of the tissue, like hemoglobin, melanin, and water [43, 45]. This gives a maximum penetration, which is found to be up to 10 cm [4]. Magnetic heating, on the other hand, is not constrained by a penetration depth limit and can reach tumors deeper in the body [46].

2.5.2 Iron Oxide Nanoparticles for Biomedical Applications

IONPs are highly relevant for biomedical applications due to their biocompatibility and low cytotoxicity [17]. Because of its high saturation magnetization, magnetite has been researched for both magnetic resonance imaging (MRI), hyperthermia cancer treatment, and targeted drug delivery [47]. As mentioned in Section 2.3, the magnetic properties of magnetite are strongly size-dependent at the nanoscale. This makes a synthesis granting sufficient control over the particle size distribution essential.

Synthesis of Iron Oxide Nanoparticles

Co-precipitation and thermal decomposition are two commonly used synthesis routes to form IONPs. Co-precipitation has the advantage of directly forming IONPs dispersed in water, but has the drawback of the particles generally having low crystallinity and a broad size distribution. More crystalline and monodisperse NPs can be formed through thermal decomposition, using higher temperatures than co-precipitation. However, a downside of thermal decomposition is the formation of particles dispersed in organic solvents. [48]

In thermal decomposition, an iron precursor such as tris(acetylacetonate) iron(III) ($Fe(acac)_3$) is decomposed into growth species using heat. The decomposition is performed in an organic solvent with a high boiling point and in the presence of a surfactant. The particle size can be tuned by controlling the temperature, heating rate, reaction time, precursor-to-surfactant ratio, and solvent [49]. The high monodispersity of the particles formed from thermal decomposition is due to the separation of the nucleation and growth steps in the LaMer diagram in Figure 2.3, as the two processes occur at different temperatures [50, 51, 52]. Nucleation occurs once the precursor is thermally degraded and supersaturation is generated, while growth happens at a higher temperature [52].

NPs dispersed in water can be formed using a water-miscible organic solvent through thermal decomposition [10, 11, 53]. TREG is a water-miscible organic solvent, which can work as both solvent, reducing agent, and stabilizer in a thermal decomposition synthesis route, as demonstrated by Maity et al [10]. Upon heating, TREG breaks down into a $R{-}O^-$ part that adsorbs to the Fe^{2+} and Fe^{3+} of the Fe_3O_4 particles, while H^+ associates to the surface of the particle, making it positively charged. Consequently, the H^+ ions provide electrostatic stabilization, while the adsorbed $R{-}O^-$ provide steric stabilization. The synthesized IONPs were monodisperse, crystalline, and SPM. [10]

Maity et al. have demonstrated another thermal decomposition synthesis, where NCs are formed [11]. Clusters are generally used to denote small particles before nucleation, with a size below 2 nm [54]. In this work, the term will be used for a collection of individual NPs that cluster together and form a larger unit, as used in the work by Maity et al. The NCs were found to exhibit a high heating efficiency and to be cytocompatible. The NCs were formed using a 1:4 ratio of TREG:TREA, where TREA is introduced to reduce the stabilization of the particles, making them cluster together to reduce their surface energy. Furthermore, it has been shown that particle diameter increases with increasing solvent boiling point [51], and TREA has a much higher boiling point than TREG. The chemical structures of TREG and TREA are shown in Figure 2.7. [11]

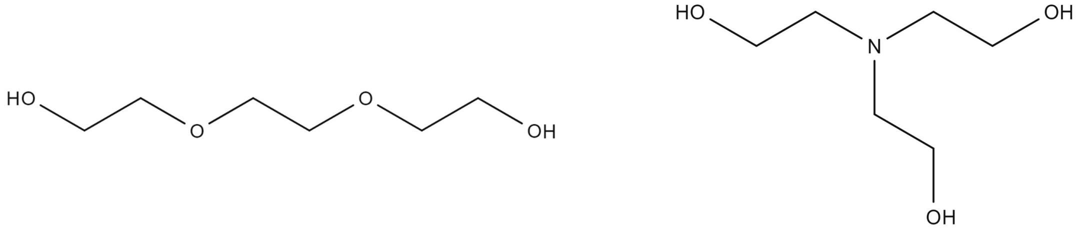

(a) TREG (b) TREA

Figure 2.7: Molecular structures of TREG and TREA.

As explained in Section 2.1.4, NPs in solution must be stabilized to prevent aggregation. For in situ stabilization, as in the synthesis routes described, the stabilizing ligands will bind to the particle surfaces during the reaction and inhibit growth, leading to smaller and more monodisperse particles [55]. Functionalization can affect the magnetic properties of NPs, where the M_S of SPM NPs is reduced by added non-magnetic weight, altering of the surface of the particles, and shielding from the applied field [56, 57, 58].

For magnetite NPs, oxidation poses a challenge. Maghemite (Fe_2O_3) is an iron oxide with a lower M_S than magnetite, and can form upon oxidation of magnetite. The two phases have very similar crystal structures and can be hard to distinguish with characterization techniques like X-ray diffraction, but some argue they can be possible to distinguish using FTIR [10, 53, 59, 60]. To avoid oxidation of magnetite, synthesis is often performed in a non-oxidizing environment, for example under an argon (Ar) atmosphere [17].

Size-Determination of Magnetic Nanoparticles

SPM NPs can behave like Langevin paramagnets at room temperature [28]. Assuming ideal and non-interacting paramagnetic particles, the magnetization in response to a magnetic field can be expressed using the Langevin function, $L(x)$, as

$$M(H) = M_S L(x) = M_S \left(\coth(x) - \frac{1}{x} \right) \tag{2.16}$$

where $x = \frac{\mu H}{k_B T}$. Furthermore, $\mu = V M_{S,bulk}$, where V is the volume and $M_{S,bulk}$ is the saturation magnetization of the bulk material (92 emu/g for magnetite) [61]. Assuming spherical particles, this relationship can be used to find the magnetic diameter of SPM magnetite NPs. [62, 63, 64]

Magnetic NPs have a reduced magnetization per volume with respect to the bulk. This is due to a lower ordering of the μ on the particle surface, an effect called spin canting, resulting in a surface layer with a lower magnetization than the bulk [56, 65, 66]. As the particle size decreases, the surface-to-volume ratio increases, making this non-magnetic layer, which is generally assumed to be around 0.6 nm, a more significant fraction of the total particle volume [55]. Consequently, the magnetic diameter of SPM NPs is generally smaller than the dry diameter.

Magnetic Heating

As explained in Section 2.3, magnetite transitions from FM to SPM when the particle is under a specific size, which is estimated to be around 20 nm [67]. The magnetic moments of SPM NPs relax rapidly when an applied magnetic field is switched off, releasing excess energy as heat. These release mechanisms are divided into Brownian and Néel relaxation. Néel relaxation is the reorientation of the magnetization vector to the axis of easy magnetization without mechanical rotation, and thermal energy is dissipated due to the rearrangement of the magnetic moments. Brownian relaxation is the return of the particle itself to its easy axis of magnetization, and thermal energy is dissipated through shear stress between the particle and the surrounding medium. The time for Brownian and Néel relaxation, in addition to the effective relaxation time, are given as

$$\tau_N = \frac{\tau_0}{2}\sqrt{\pi\frac{k_BT}{KV_{dry}}}e^{KV_{dry}/k_BT} \tag{2.17}$$

$$\tau_B = \frac{3\eta V_{hyd}}{k_BT} \tag{2.18}$$

$$\frac{1}{\tau} = \frac{1}{\tau_N} + \frac{1}{\tau_B} \tag{2.19}$$

where τ_0 is 10^{-9} to 10^{-13} s [68], K is the magnetic anisotropy constant (25 kJ/m^3 for spherical magnetite NPs), V_{dry} is the dry volume of the particles, and V_{hyd} is the hydrodynamic volume [69]. η is 8.9 $\cdot 10^{-4}$ Pa·s for water at physiological temperatures. K includes both the shape anisotropy and crystalline anisotropy and has been found to increase for interacting particles [70]. τ is generally in the order of 10^{-8} to 10^{-6} s [71]. Néel and Brownian relaxation take place in parallel, and the one with the shorter relaxation time dominates. [70]

FM particles generate heat through a hysteresis loss, which is proportional to the area of the hysteresis loop. This is negligible for perfectly SPM NPs, as shown in Figure 2.5, and relaxation mechanisms generally dominate for particles below around 15 nm [69, 71, 72]. However, interactions between magnetic particles can increase the blocking temperature and lead to higher magnetic anisotropy, increasing the hysteresis [66, 68].

The heating efficiency of SPM NPs upon exposure to an AMF is characterized by the specific absorption rate (SAR),

$$\mathrm{SAR} = \pi \mu_{0,B} \chi H^2 f \frac{1}{\rho} \tag{2.20}$$

where ρ is the density of the material. χ increases with increasing magnetic interactions [66]. The expression for SAR can be rewritten as

$$\mathrm{SAR} = \frac{8\pi^3 \mu_{0,B}^2 M_S^2 r^3 H^2 f^2 \tau}{3\rho k_B T (1 + 2\pi f \tau)^2} \tag{2.21}$$

which is optimized when when $\omega \cdot \tau = 1$, where $\omega = 2\pi f$ [58, 69]. The heating efficiency of SPM NPs can be experimentally characterized using a nanoTherics magneTherm. This instrument applies a radio frequency AMF to a sample and records the resulting heat generation using a temperature probe. The SAR has units W/g, and is experimentally determined by the temperature gradient achieved when heating a colloidally dispersed magnetic material, as

$$\mathrm{SAR} = \frac{C_w}{m} \left(\frac{\Delta T}{\Delta t} \right) \tag{2.22}$$

where C_w is the specific heat capacity of the dispersion medium (4185 J/kg°C for water), m is the mass of the sample, and $\Delta T / \Delta t$ is the rate of the temperature change with respect to time. The temperature slope would be linear for an adiabatic set-up, but since this is not generally the case for laboratory set-ups, only the initial slope is normally used [73]. The SAR has experimentally been found to increase with increasing r and M_S, as predicted by Equation 2.21, but also with increasing monodispersity and colloidal stability [58]. The influence of the surface coating on the SAR depends on the coupling between the magnetic core and the surface coating [74, 75]. From Equation 2.22, the SAR is normalized by the mass of the IONPs, indicating an independency of the concentration. However, different studies have reported contradictory results on the effect of concentration on SAR due to particle interactions [68, 69].

A drawback with the SAR parameter is its dependency on H and f, making it challenging to compare different laboratories using different AMF strengths. Kallumadil et al. have suggested the intrinsic loss power (ILP) [73], also called the effective SAR [69], as an alternative parameter, which is found by normalizing the SAR with H^2 and f:

$$\mathrm{ILP} = \frac{\mathrm{SAR}}{H^2 f} \tag{2.23}$$

using units W/kg for SAR, kA/m for H, and kHz for f, and nHm^2/kg for ILP. The parameter is valid for f between 100 and 1000 kHz, and when the polydispersity index (PDI) of the NPs is more than 0.1. The ILP is an attempt at an intrinsic parameter not affected by the experimental conditions, but the SAR parameter is more widely used. [73]

Magnetic heating is a non-invasive method [47], with no penetration depth limit [46]. Magnetic fields do generally not influence biological processes and are therefore promising for biomedical applications. However, strong AMFs can generate Eddy currents in biological tissue and consequently cause irreversible damage [2]. Therefore, there are clinical limitations regarding their strengths. The conventional limit is called the Atkinson–Brezovich limit, which was experimentally determined from patient discomfort upon the exposure of an AMF around the torso for an hour [72]. The heat generation in tissue was assumed proportional to $(H \cdot f \cdot r)^2$, with r being the radius of the exposed region [76]. For the torso, the limit was set to $(H \cdot f)$ not exceeding $4.85 \cdot 10^8$ A/(m · s). However, several more recent studies argue that the limit could be adjusted to $4.85 \cdot 10^9$ A/(m · s) when using shorter exposure times or smaller body parts [74, 77, 78]. Individual limits for the maximum H and f have been proposed to be 15 kA/m and 1.2 MHz, respectively [2].

Based on the presented limits, a high SAR value obtained using low H and f values is desirable. SAR values in the lab will often be higher than in human tissue due to heat dissipation mechanisms in the body [79]. Still, limits considering the temperature increase in the body as a result of the heating particles must also be considered. The local temperature should not be increased past 45 °C as irreversible damage of healthy cells occurs above 46 °C [80]. Cancer cells can be killed at temperatures around 42-45 °C [81], but the temperature needs to stay above 42 °C for 30 min [2]. Consequently, efficiently heating SPM NPs are needed to use magnetic heating to kill cancer cells. Lower temperatures over shorter time intervals can be used to induce collapse in temperature-responsive NGs. This will be elaborated on in the following chapter.

2.5.3 Hybrid Nanogels for Targeted Drug Delivery

A targeted drug delivery system can be developed by combining the optical or magnetical heating properties of AuNPs or IONPs with stimuli-responsive NGs. The synthesis of hybrid NGs incorporated with these inorganic NPs will now be presented.

Synthesis of NIPAM-AAc Nanogels

NIPAM-AAc NGs can be synthesized through co-precipitation polymerization at temperatures above the LCST of NIPAM, causing them to be insoluble in water and precipitate out [30]. The NG properties will depend on the reactants, and the relative mole percentage of the two monomers [30].

Monomers are the fundamental building blocks constituting the NGs. Keeping the concentration of other reactants constant, increasing monomer concentration increases particle size, as more monomer units are incorporated into each particle [21]. NIPAM, with an LCST near physiological temperature, is attractive for biomedical applications where temperature responsiveness is utilized. The VPTT of NIPAM NGs can be increased by co-polymerization with a hydrophilic monomer, like AAc. This also provides pH responsiveness to the NGs, since AAc is an acidic monomer [82]. The VPTT can also be modified by adding additives and is influenced by cross-linking density, the balance of hydrophobic-hydrophilic interactions, solvent composition, and ionic strength [8].

For the NIPAM-AAc NG synthesis, one can use potassium persulphate (KPS) as an initiator, sodium dodecyl sulfate (SDS) as a surfactant, and N,N'-methylenebisacrylamide (BIS) as a cross-linker. The relative concentration of these reactants will influence the final NG properties. Initiators form free radicals, which determine the number of particles formed, analogous to the number of nuclei formed in the CNT. Consequently, more initiators will generally result in smaller particles, since the monomers will be divided between a higher number of particles [83]. Surfactants stabilize the particles that have formed [84], leading to a reduced aggregation and forming a smaller and more narrow particle distribution [83]. Monodispersity is generally an important property, and a PDI lower than 0.2 is often considered acceptable for polymeric particles [85]. Furthermore, surfactants increase the viscosity of the medium and prevent precipitation, leading to fewer monomers being incorporated into each particle [86]. Cross-linkers form more compact particles, and the particle size decreases with increasing cross-linking density [87]. An increased cross-linking density also decreases the mobility of the macromolecular chains, giving less free volume for water absorption, resulting in lower swelling of the particles [88]. However, one must be careful when comparing exact values between different polymeric systems, as significant batch-to-batch variations of the monomers are common, leading to different results [89].

The LSPR peaks of AuERs have been found to remain the same upon incorporation into NGs [90], and magnetic NPs have been found to remain SPM upon incorporation into NGs [91]. Therefore, by incorporating AuNPs or IONPs into the temperature-responsive NGs, the collapse of the NGs can be externally triggered using EM irradiation or an AMF, respectively. This can be used to trigger the release of a loaded drug.

Drug Loading Using Hybrid Nanogels

Model drugs are substances used to study the factors influencing drug delivery. The hydrophilicity of the drug is an important property, which influences its interactions with the carrier and the solvent. SA is a small and hydrophobic molecule with a molecular weight of 138 g/mol [92], which mainly binds to the lipophilic branches of NGs [13]. However, it has a slight solubility of around 2 mg/mL in water at 25 °C and neutral pH. SA is acidic, having a pK$_a$ of 3.01, and exhibits multiple absorbance peaks in the ultraviolet (UV) part of the EM spectrum, where one is located at 296 nm [14]. As a result of its small size and hydrophobicity, it can be used to mimic hydrophobic cancer drugs [13, 14, 15, 93]. The protein Cyt C has a molecular weight of 12 kDa, and has a positive charge at neutral pH, having an isoelectric point at 10.1 [16, 94]. In the literature, there are several studies using Cyt C as a model drug in NGs [30, 94, 95]. NIPAM-AAc NGs contain both hydrophobic and hydrophilic domains. This allows for studying the loading and release of both hydrophilic and hydrophobic drugs. Utilizing both SA and Cyt C as model drugs provides valuable insights into how the size, charge, and hydrophilicity of a drug can affect its interactions with the delivery system and the mechanisms of drug loading and release.

NGs can load drugs through a breathing-in mechanism, where the freeze-dried NGs are dispersed in a solution containing the drug [30]. The primary loading mechanism is assumed to be the physical encapsulation of the drugs into the pores of the polymer matrix [21, 94]. However, there can also be electrostatic or hydrophobic interactions between the drug and the NGs [8, 96]. As an examples, the positively charged Cyt C can form a polymer-protein complex with the negatively charged AAc [94, 95]. Additionally, SA has been shown to interact with hydrophobic branches of the NGs, but also to have van der Waals interactions with the hydrophilic branches [13]. Hybrid NGs generally have lower loading than bare NGs, due to the NPs occupying space and reducing binding sites [94]. The drug loading can be characterized using the loading efficiency (LE) [%] and encapsulation efficiency (EE) [mg drug/mg NG] [30]. If the drug-loaded NGs are separated from the unloaded drug through centrifugations, the LE and EE can be calculated using

$$\mathrm{LE} = \frac{c_0 - c_{sup}}{c_0} \cdot 100 \tag{2.24}$$

$$\mathrm{EE} = \frac{c_0 - c_{sup}}{c_{NG}} \tag{2.25}$$

where c_0 is the concentration of drug added to the gel, c_{sup} is the drug concentration measured in the supernatant, and c_{NG} is the concentration of NGs [30]. c_{sup} can be found by obtaining a calibration curve, utilizing the linear relationship between the absorbance and concentration of the drug given by Beer-Lambert's law

$$A = \epsilon l c \tag{2.26}$$

where A is the absorbance, ϵ is the molar absorption coefficient, l is the optical path length, and c is the concentration [21]. Assuming that ϵ and l are constant, a linear relationship exists between c and A. As a general rule, this is valid for absorbance below 1.

Hybrid Nanogel-Based Drug Delivery Systems

Drug-loaded NGs injected into the body can act as drug delivery vehicles, protecting the drug from chemical and mechanical degradation. Furthermore, the carrier can transport the drug to the target site via passive targeting, accumulating in tumor tissue as a result of the enhanced permeability and decreased retention compared to healthy tissue [21]. Biocompatibility is an essential property for particles used for targeted drug delivery in order to avoid triggering dangerous immune responses in the patient or being removed by the body before reaching the target site. Particle size is an important property, as presented in Section 2.1.2, and so is the surface of the particles, as particles with a hydrophobic surface undergo opsonization more slowly than hydrophilic ones [8]. Additionally, control over the biodistribution is essential, and the particles must either be biodegradable or removed by the clearance systems in the body after the drug release, in order to avoid triggering an immune reaction or accumulating and becoming cytotoxic after time. Removal of the NPs is important, as they can cross critical barriers and cause cytotoxicity after being exocytosed [18]. Collapsed NGs will become small and hydrophobic and will therefore be faster cleared out by the kidneys or the MPS system than the swollen particles [18]. The potential of stimuli-responsive NGs to selectively release a loaded drug can lead to a higher therapeutic effect and fewer side effects than systemic administration. This is illustrated in Figure 2.8, with temperature and pH as stimuli.

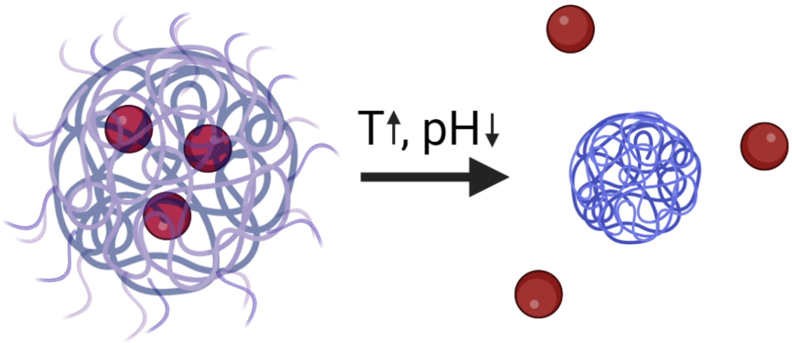

Figure 2.8: Nanogel collapsing as a response to a decrease in pH and increase in temperature, leading to the release of a loaded drug. Figure created with Biorender [20] and adapted from Nayak et al. [8].

Incorporating AuNPs into NGs can improve imaging, as well as enhance stimulus-triggered release upon irradiation, providing interesting properties to the hybrid drug delivery systems [8, 43, 90, 94, 95]. Bandoypadyhay et al. and Raghunathan et al. have performed studies comparing the effect of differently shaped AuNPs on the properties of the NGs [90, 95]. The etched rods (AuER) were found to give a VPTT of almost 40 °C and high loading and release properties [90]. Kawano et al. incorporated gold nanorods with a peak in the NIR region into NIPAM NGs to make the NGs respond to the generated heat [43]. A rapid shrinkage of the NGs was observed upon irradiation with a laser at 807 nm and a power of 3.4-4.2 W/cm^2. Furthermore, Wu et al. have reported Ag-Au hybrid temperature-responsive NGs with a photothermal targeted drug release using a 1.5 W/cm^2 NIR light for 5 min [97].

Drug release kinetics can be studied in vitro using the magneTherm, which also allows the application of an AMF to the drug delivery system. There are several examples of drug delivery systems consisting of NGs incorporated with IONPs that have reported an increased drug release upon application of an AMF [46, 98, 99]. Hua et al. compared the release of polymeric poly(lactic-co-glycolic acid) NPs encapsulated with 100 nm magnetic NPs with and without the application of an AMF [98]. The drug release increased two-fold in the presence of the AMF, attributed to both the heating and mechanical disruption of the polymer through the movement of the particles, since the release increased even when the field was weak and little to no heat was generated. Hu et al. studied the drug release of pH-responsive hydrogels incorporated with magnetic NPs at both pH of 4.5 and using an AFM [99]. An increase in drug release was observed, attributed to the effect of low pH to give weaker electrostatic interactions between drug and carrier, and due to the stress that was induced to the polymeric network by the magnetic particles in the AMF. Cazares-Cortez et al. physically entrapped drugs in NGs incorporated with magnetic NPs, and applied AMF pulses of 30 min [46]. The increased release was explained by the magnetic NPs creating hot spots in the polymer matrix, making the temperature increase above the VPTT of the NGs and triggering release. The magnetic NPs also induced conformational changes in the NGs, which released twice as much drug with the pulsed AFM compared to without it.

The results reported in the literature show the potential of hybrid NGs for targeted drug delivery. However, several studies use magnetic fields far exceeding clinical limits [99], or obtain magnetic particles with low SAR values [46], limiting their applicability. Despite the many promising studies, hybrid NGs have still not reached the clinical stage, and a deeper understanding of the release mechanisms is crucial for developing more predictable drug delivery systems [100]. Achieving a sustainable release is a common issue, with many systems having an initial rapid release or a very slow overall release, where a continuous stimulus is often used to trigger NG collapse and subsequent drug release. A pulsed stimulus has been proposed to enhance the release, since the collapsing NGs might form a polymer skin on the surface, preventing the drugs from escaping [90, 101]. The final section of this literature review will provide a description of release profiles that describe the release from hybrid NGs.

Drug Release Models

Understanding the mechanics and kinetics of drug release is essential to predict the therapeutic effect. The release depends on the mechanism between the carrier, drug, and medium [102]. Interactions between the drug and the carrier can slow down the release, where hydrogen bonds or electrostatic and hydrophobic interactions are important examples [8, 103]. Alternatively, the drug can be physically encapsulated. Burst release is the rapid initial release of drugs from their carrier and can happen for poorly bound drugs [104]. The concentration profile of the drug within the carrier, and the solubility of the drug in the release medium will also influence the release [105]. Several models have been proposed to describe drug release, with Fickian release, zero-order release, first-order release, Peppas [106], and Higuchi [107] being among the most common ones. These models are based on phenomena like swelling, diffusion, dissolution, erosion, and degradation, or combinations of these [105]. Peppas model describes the drug release behavior from polymeric systems [104, 106], while the Higuchi model describes the release from a matrix system based on Fick's law of diffusion [107, 108]. These models assume a constant size of the drug delivery system, and can consequently not be used to describe drug release from collapsing NGs.

Fickian release explains release through diffusion, as a result of a drug concentration gradient. Fick's first law of diffusion gives the flux as

$$J = -D\frac{\partial c}{\partial x} \tag{2.27}$$

where D is the diffusion, c is the concentration, and x is the distance in one direction [21].

Zero-order release refers to a constant drug release rate that is independent of time and the remaining drug concentration. The amount of the released drug is given by

$$Q = Q_0 k_0 t \tag{2.28}$$

where Q_0 is the initial amount of drug (usually zero), k_0 is the zero-order release constant, and t is the time. This can be achieved through various mechanisms, including diffusion, erosion, and osmosis. Since the clearance mechanisms in the body will remove the drug, a zero-order release can, at an equilibrium, give a constant drug concentration in the medium, and is consequently the desired release kinetics. [104, 108]

First-order release describes a drug release rate proportional to the concentration of the drug remaining in the drug delivery system, as

$$Q = Q_0 \cdot \exp(-k_1 t) \tag{2.29}$$

where k_1 is the first-order release constant, and the drug release rate decreases exponentially over time as the concentration of the drug in the formulation decreases.

Zero-order release is desirable, but first-order and burst release are more commonly reported in drug delivery systems. [104, 108]

Physically encapsulated drugs can be released from the pores of NGs through diffusion [95, 100]. For small molecules, the release can be faster at T<VPTT than at T>VPTT due to larger pores, when diffusion is a release mechanism [8]. It has been hypothesized that release from NIPAM-AAc NGs upon dual stimuli is mainly through a squeezing-out mechanism due to the collapse, where the drug is expelled from the pores of the polymer matrix [94, 30]. Chemical bonds between the NGs and the drug would give a lower release than purely physical encapsulation [21].

This work will study a system consisting of AuNPs or IONPs incorporated into NGs. AuERs will be used due to promising reported drug loading and release properties [39], and IONCs will be used due to high reported heating efficiencies [11]. Co-polymerized NIPAM-AAc NGs will be used due to the dual responsiveness and high collapse [30]. The heating efficiency of the IONPs will be optimized, and the drug loading of a hydrophilic and hydrophilic drug will be compared. Finally, the drug release will be studied under conditions with varying temperatures, pH, and AMFs. The project aims to synthesize a hybrid targeted drug delivery system that can obtain a zero-order release upon external stimuli.

Chapter 3

Materials and Methods

This section provides a description of the materials, syntheses, and characterization techniques used in this work. First, the materials used for the syntheses are presented. Then, the synthesis routes and characterization techniques are described. Lastly, the methods used to evaluate drug loading and drug release are explained.

3.1 Materials

Table 3.1 displays the chemicals that were used for the syntheses. Cyt C and SA were obtained from Sigma-Aldrich, and Milli-Q (MQ) water was obtained from NTNU.

Table 3.1: List of chemicals used for the AuER [39], IONP, and NG synthesis, respectively.

Synthesis	**Chemical**	**Manufacturer**	**Purity**
AuNE	Cetyltrimethylammonium bromide (CTAB)	Acros Organics	$\geq$99 %
	Ascorbic acid (AsA)	Fluka	$\geq$99 %
	Silver nitrate ($AgNO_3$)	Sigma-Aldrich	$\geq$99 %
	Gold(III) chloride trihydrate ($HAuCl_4 \cdot 3H_2O$)	Sigma-Aldrich	99.9 %
	Oleic acid (OA)	Sigma-Aldirch	$\geq$99 %
	Sodium borohydride ($NaBH_4$)	Sigma-Aldrich	$\geq$98 %
IONP	Iron(III)acetylacetonate ($Fe(acac)_3$)	Sigma-Aldrich	$\geq$97 %
	Triethylene glycol (TREG)	Sigma-Aldrich	99 %
	Triethanolamine (TREA)	Sigma-Aldrich	$\geq$99 %
	Absolute ethanol	VWR	96 %
	Ethyl acetate	VWR	99.9 %
NG	Acrylic acid (AAc)	Sigma-Aldrich	-
	N-isopropylacrylamide (NIPAM)	Sigma-Aldrich	100 %
	N,N'-methylenebis(acrylamide) (BIS)	Sigma-Aldrich	99 %
	Sodium dodecylsulphate (SDS)	Sigma-Aldrich	99 %
	Potassium persulphate (KPS)	Sigma-Aldrich	99 %

3.2 Synthesis

Figure 3.1 illustrates a schematic representation of the synthesis steps for the targeted drug delivery system. These syntheses will now be described.

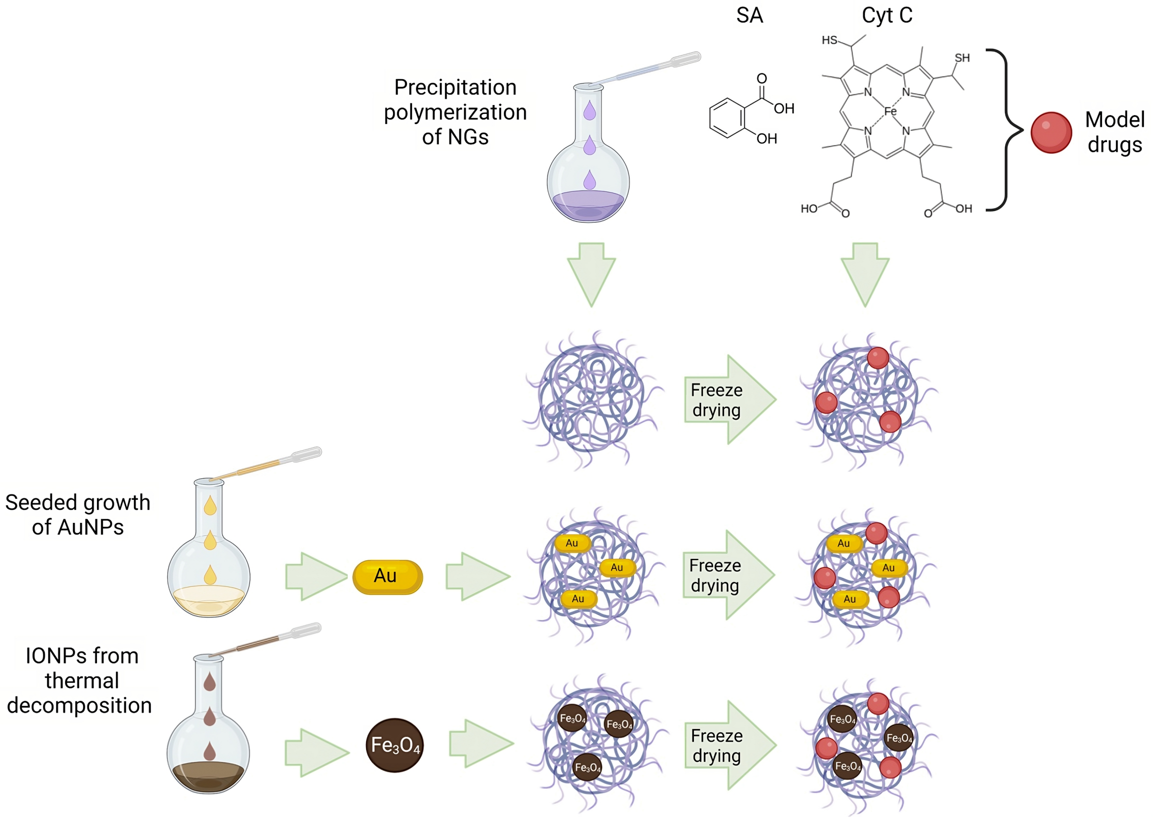

Figure 3.1: Schematic representation of the synthesis routes for the drug delivery systems, illustrating the bare NGs, the NGs incorporated with AuNPs, and the NGs incorporated with IONPs. Molecular structures for the SA and Cyt C model drugs are shown, while red dots are used to illustrate the loaded drugs. Figure created using BioRender [20].

3.2.1 Synthesis of Gold Nanoparticles

Gold nanoparticles with an etched nanorod morphology were chosen due to a high reported VPTT, drug loading, and release for NGs incorporated with these particles compared to other morphologies [90]. The AuERs used in this work were synthesized by Raghunathan et al. using a seeded growth technique, where the following synthesis route was used [39].

The AuERs were synthesized using a seeded growth. For the seed solution, 5 mL of 0.2 M of CTAB was mixed with 0.4 mM $HAuCl_4$, before 3.75 mM of $NaBH_4$ was added. The mixture was stirred for 2 min before aging at room temperature for 30 min. The growth solution was prepared by mixing 1.2 g of CTAB and 20 µL of OA in 15 mL of MQ water at 80 °C and was stirred at 1200 rounds per min (rpm) using a magnetic stirrer. The temperature was lowered to 35 °C before 750 µL of 4 mM $AgNO_3$ was added just after being prepared. The solution was stirred for 15 min before 15 mL of 1 mM $HAuCl_4 \cdot 3H_2O$ was added, and the solution was stirred for 15 min more. Then 135 µL of 128 mM AsA was added, and the solution was stirred at 1000 rpm. Lastly, 96 µL of seed solution was added to the growth solution under stirring at 1200 rpm. The particles were cleaned using centrifugation at 11 000 rpm for 5 min, using an Eppendorf Centrifuge 5810 Ultracentrifuge. The particle concentration was determined by measuring the weight of a vial containing 200 µL of particle solution before and after heating it at 55 °C for 24 hours to evaporate the water.

3.2.2 Synthesis of Iron Oxide Nanoparticles

IONPs were synthesized using thermal decomposition, where the set-up is presented in Figure 3.2. Two different synthesis routes were performed, forming nanospheres (NS) and NCs. The NCs were further divided into those separated using magnetic separation, denoted mNCs, and those separated through centrifugation, denoted cNCs.

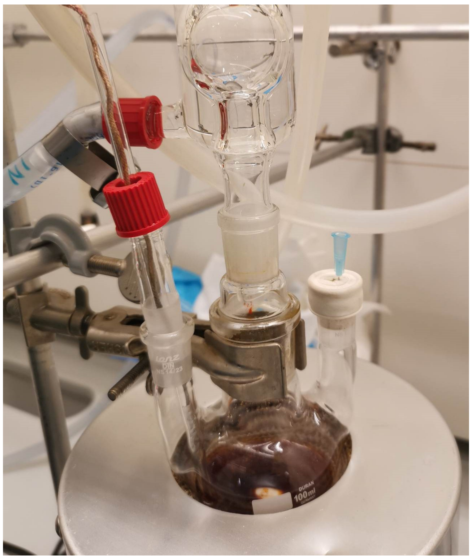

Figure 3.2: Photo of the thermal decomposition set-up for the IONP synthesis. The same set-up was used for NS and NC synthesis, consisting of a three-necked round-bottom flask, condenser, Ar gas, magnetic stirrer, and a temperature probe.

Nanospheres

The NS synthesis was inspired by work reported by Maity et al. [10]. 2 mmol $Fe(acac)_3$ was dissolved in 20 mL TREG in a three-necked round-bottom flask under magnetic stirring at 400 rpm. The flask was attached to a condenser at 4 °C, and the solution was flushed with Ar gas for 5 min. The solution was dehydrated at 120 °C for 1 hour, before the temperature was gradually increased at a rate of 20 °C per min until it reached 280 °C. The reaction was allowed to proceed at 280 °C for 2 hours. Once the reaction was complete, the solution was taken away from the heat and allowed to cool down to room temperature.

The particles were cleaned using magnetic decantation, by being precipitated using 20 mL of ethyl acetate, isolated using a disc magnet, and redispersed in ethanol. This process was repeated three times. The particles were then stored in 20 mL of MQ water at 4 °C. The concentration was measured as before.

Nanoclusters

The NC synthesis route was inspired by a second study reported by Maity et al. [11]. 2 mmol of Fe(acac)$_3$ was dissolved in a mixture of 16 mL of TREA and 4 mL of TREG in a three-necked round bottom flask, giving a 4:1 v/v TREA:TREG ratio. A condenser at 4 °C was attached to the flask, and the solution was flushed with Ar gas and stirred at 250 rpm for 10 min. Subsequently, the solution was dehydrated at 120 °C for 1 hour, and heated to 280 °C with a heating rate of 20 °C per minute. The temperature was kept at 280 °C for 1 hour.

After the solution was cooled down to room temperature, it was split into two equal parts. One part was magnetically separated, while the other part was centrifuged. The concentration was measured as before.

3.2.3 Synthesis of NIPAM-AAc Nanogels

The NGs were synthesized through co-precipitation polymerization of NIPAM and AAc [30], where the set-up is presented in Figure 3.3. Four samples were prepared: two bare NGs and two hybrid NGs incorporated with NPs. For the bare NGs, one sample had a NIPAM:AAc:BIS molar ratio of 85:10:5, and will be denoted NG10, while the other had 70:25:5, and will be denoted NG25. For the hybrid NGs, the molar ratio of NIPAM:AAc:BIS was 85:10:5, and 0.5 mg of NPs were added during the synthesis. The NGs containing AuERs will be denoted AuNG10, and were synthesized by Raghunathan [90]. The NGs containing IONPs will be denoted FeNG10. The cNC sample was used, based on a comparative study of the IONP samples, which will be presented in the results and discussion section.

NIPAM was recrystallized prior to the NG synthesis, by heating 5 g of NIPAM and 50 mL of n-hexane in a round-bottom flask at 110 °C for 2 hours, while connected to a condenser at 4 °C. Thereafter, the NIPAM was separated from the n-hexane using a Büchnel funnel containing a filter. The funnel was covered with a perforated parafilm to allow the remaining n-hexane to escape while the set-up was left overnight. The NIPAM was stored at -18 °C.

For the NG synthesis, 80 mg of the recrystallized NIPAM and the desired amount of

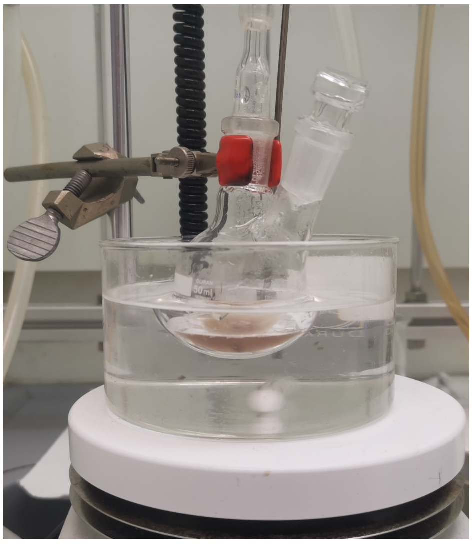

Figure 3.3: Photo of the set-up for the NG synthesis through co-precipitation polymerization of NIPAM and AAc. The set-up consisted of a two-necked round-bottom flask connected to nitrogen gas in a silicon oil bath. FeNG10 was synthesized in the photo, as seen from the color.

BIS were added to a two-necked round-bottom flask and melted at 70 °C. 6.4 mg of BIS was used for NG10, FeNG10, and AuNG10, and 6.8 mg of BIS was used for NG25. Then, 5 mL of 4.2 mmol of SDS, mixed with 0.5 mg of NPs for the hybrid NGs, was added to the solution. The reaction mixture was purged with nitrogen (N) gas for 30 seconds to create an inert atmosphere and left to dissolve for 1 hour at 300 rpm, using a magnetic stirrer. Under N atmosphere, 57 µL of 1.40 M of AAc was added for NG10, FeNG10, and AuNG10, and 175 µL was added for NG25. 400 µL of 103.6 mM of the initiator KPS was prepared and immediately added to the solution to avoid it from reacting before being added. This solution reacted for 2 hours before the flask was removed from the heat and allowed to cool for 10 min.

Any remaining reactants were removed through dialysis. A Sigma-Aldrich dialysis tubing cellulose membrane with a molecular weight cut-off (MWCO) limit of 14.5 kDa was placed in water for 15 min to wet the pores before being filled with the NG solution and secured with dialysis clips. The bags were placed in 1.5 L of MQ water with stirring at 100 rpm for 24 hours, replacing the water after approximately 5 and 18 hours to maintain a high concentration gradient.

After dialysis, the NGs were transferred to a centrifuge tube and freeze-dried. Liquid N was used to cool the sample, before a Virtis Benchtop Pro Freeze Dryer with a temperature of -60 °C and a pressure of 60 mTorr induced sublimation, removing the excess water from the gels. The system was left overnight until all of the water had evaporated, before the samples were stored at -18 °C.

3.3 Characterization

After synthesis, the AuNPs, IONPs, and NGs were characterized. Fourier Transformation Infrared spectroscopy was used to evaluate the chemical properties. Scanning (transmission) electron microscopy was used to evaluate the morphology and dry size. The zeta potential, hydrodynamic size, and polydispersity index were determined using a Zetasizer. The magnetic properties of the IONPs were characterized using a Vibrating Sample Magnetometer. The drug loading and manual release studies were performed using UV-Vis spectroscopy. Finally, the heat generated by the magnetic NPs and the drug release was studied using magneTherm.

3.3.1 Fourier Transform Infrared Spectroscopy

FTIR was used to identify functional groups in the NP and NG samples, using a Bruker Vertex 80v FTIR with an attenuated total reflectance (ATR) measurement cell. A dried sample was used. The background and measurements were performed in a vacuum of approximately 3 hPa from 4000 to 400 cm^-1, corresponding to the IR range of the EM spectrum. A number of 100 scans were performed per sample, and the average was calculated to reduce noise.

3.3.2 Scanning (Transmission) Electron Microsopy

S(T)EM Hitachi SU9000 was used to image the NPs and NGs to find the shape and the dry diameter of the particles. The instrument was operated in bright field (BF) mode, using an acceleration voltage of 20 or 30 kV and a current of 10 µA. The samples were prepared by dropping the solution onto a TEM grid. For the NGs, 10 µL of phosphotungstic acid (PTA) were subsequently dropped onto the deposited solution to stain the sample. The size of the particles was measured using ImageJ [109].

3.3.3 ZetaSizer

Malvern Zetasizer Nano-ZS was used to determine the ζ of the particles using Electrophoretic Light Scattering (ELS), and the d_{hyd} and PDI using DLS. As described in Section 2.4, DLS determines the d_{hyd} using the Stokes-Einstein equation, defined in Equation 2.14. As mentioned, the technique assumes spherical particles. The intensity-distribution of the particles was measured. For the NG measurements, 1 mg/mL of the freeze-dried NG sample was dispersed in MQ water, unless otherwise stated. For the NP measurements, the solution was diluted until it obtained a pale color. The pH of the MQ water was 6 according to a Mettler Toledo FiveEasy Plus pH meter FP20. If not specified, the measurements were performed at 25 °C. Disposable poly(methyl methacrylate) (PMMA) cuvettes were used as sample holders, and three measurements were performed for each sample.

The VCE for temperature, pH, and dual stimuli were found by measuring the d_{hyd} of the NGs at 25 and 45 °C, at pH 6 and 3, and at 25 °C with pH 6 and 45 °C with pH

3, respectively. The pH was reduced using 10 M of HCl to obtain pH 3. The VCEs were calculated using Equation 2.15. The VPTT was found by measuring the d_{hyd} of the NG particles between 25 and 55 °C, with 5 °C intervals. The swelling and collapse curves were then found using the swelling ratio, given by

$$\alpha = \left(\frac{d}{d_0}\right)^3 \tag{3.1}$$

where d_0 and d are the hydrodynamic diameters at 25 °C and at the measured temperature, respectively [21]. α was fitted to a sigmoidal curve using SigmaPlot [110], and the VPTT was found from the areas under the cooling and heating curves using the fitting parameters, using a MATLAB [111] script. [32]

3.3.4 Vibrating Sample Magnetometer

PMC MicroMag 3900 Series Vibrating Sample Magnetometer [112] was used to characterize the magnetic properties of the IONPs and FeNG10. NG10 was measured to establish any magnetic contributions from the NGs and the sample holder. The vibrational frequency was 83 Hz, the maximum applied field was 10 kOe, the step size was 100 Oe, and the measurement time at each step was 250 ms. Corrections of any para- or diamagnetic contributions were done at above 70% of the maximum applied field to avoid artifacts.

Around 10 mg of dried particles were weighed and placed in a gel capsule sample holder for each measurement, and the position of the sample was adjusted to the middle of the magnetic field. The precise weight of each sample is provided in Table 3.2. A Python script [64] was used to fit the measured data to the Langevin function, defined in Equation 2.16.

Table 3.2: The weights of the samples measured using a VSM.

Sample	**Weight [mg]**
NS 1	10.1
NS 2	10.2
NS 3	10.2
mNC 1	9.6
mNC 2	10.3
mNC 3	9.8
cNC 1	12.0
cNC 2	10.7
cNC 3	10.1
NG10	9.2
FeNG10	8.9

3.3.5 magneTherm Hyperthermia Studies

The nanoTherix magneTherm was used to study the heat generated by the magnetic NPs under an AMF. For these measurements, an IONP or NG solution was inserted into a tube containing a temperature probe, and placed within an insulator in the middle of the coils in the instrument. Unless otherwise stated, the concentration of the solution was 1 mg/mL. The temperature was recorded as a function of time while an AMF was applied to the sample. The instrument calculated the SAR based on the initial temperature slope at 5 to 200 seconds using Equation 2.22, using the IONP concentration and density (5.17 g/mL for magnetite) to calculate the mass. Each measurement lasted for 15 min, and the sample was cooled to room temperature at approximately 23 °C between measurements.

The instrument provided coils with 9 and 18 turns and capacitors with a capacitance of 6.2, 88, and 200 nF, giving six different combinations. For each combination, the instrument performed a frequency sweep, finding the resonance frequency. The Brezovich limit [76] and the ten times stronger literature limit [74, 77, 78] were introduced in Section 2.5.2. Assuming that $B = \mu_{0,B} H$ is valid for mediums with negligible magnetic contributions like MQ water [113], the corresponding maximum field for each limit could be calculated from the given frequencies. As a result of instrumental restrictions, the limit reported in the literature was adjusted down to a lower value, which will be denoted the Instrument limit. Consequently, the magnetic heating efficiency of all samples was characterized twice, once using the Brezovich limit of $4.85 \cdot 10^8$ A/(m·s) and once using the Instrument limit of $2.45 \cdot 10^9$ A/(m · s). I.e., the Instrument limit gives a $H \cdot f$ product approximately five times the Brezovich limit.

3.3.6 UV-Vis

Agilent Cary 3500 UV-Vis was used to find the absorbance as a function of the wavelength for the drugs, using the relationship between A and c given by Beer-Lambert's law, defined in Equation 2.26. This linear relationship was used to obtain calibration curves for the drugs. The absorbance at known drug concentrations was characterized, where the absorbance at the peak was used to determine the calibration curves for the drugs using linear regression.

The scans were performed from 200 to 400 nm for SA, based on the wavelength of maximum absorbance for the drug. Quartz cuvettes were used because plastic cuvettes did not transmit well at low wavelengths. For Cyt C, disposable plastic cuvettes were used, and the absorbance was measured between 350 and 700 nm. Unless otherwise stated, the baseline was measured using MQ water at room temperature.

3.4 Drug Loading

1.5 mg/mL of SA or 0.5 mg/mL of Cyt C was dissolved in water for the drug loading. The concentrations were determined from preliminary studies, which will be presented in the results section. Vigorous stirring and heat were needed to dissolve SA completely. The freeze-dried NGs were drug loaded using a breathing-in mechanism, where 2 mL of the drug solution was added to 1.7 mg of freeze-dried NG, and mixed by shaking at 300 rpm for 2 hours. The drug-loaded samples were centrifuged for 30 min to remove the supernatant. The absorbance of the supernatant was measured using UV-Vis. Equations 2.24 and 2.25 were used to calculate the LE and EE, where c_{sup} was found utilizing the calibration curves obtained using UV-vis.

3.5 Drug Release Studies

Two different techniques were used to study the drug release, one using the magneTherm, and the other by manual sampling. Figure 3.4 illustrate the differences between these two techniques.

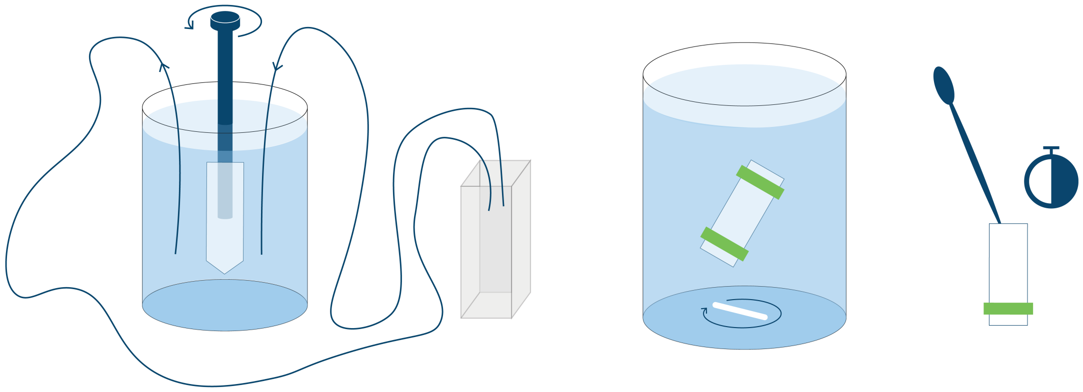

(a) magneTherm method

(b) Manual method

Figure 3.4: Illustrations of the differences between the two drug release methods used. Figure (a) shows the magneTherm method, where the release medium is continuously monitored using UV-vis. Figure (b) shows the manual method where the absorbance inside the membrane is measured every 30 min.

Using the magneTherm, the release was characterized through continuous monitoring of the absorbance in the release medium. These studies will be denoted the magneTherm release studies. For the manual sampling, the drug release was performed using a dialysis membrane in a water bath, conducted by manually sampling the absorbance inside the membrane every 30 min. These studies will be denoted the manual release studies. Unless otherwise stated, 1.7 mg NG loaded with a drug, as described in the section above, was dispersed into 2 mL of the desired release medium inside the membrane for all the release studies.

3.5.1 magneTherm Release Studies

A photo of the magneTherm release set-up is shown in Figure 3.5. The drug-loaded NGs were placed inside a dialysis tube with an MWCO of 6-8 kD, which was placed inside the instrument into 25 mL of the desired release medium. A water cooler held the desired temperature. The drug release was performed under sink conditions. Only SA was used as a model drug for these drug release studies, while Cyt C was excluded due to its high molecular weight, rendering it unsuitable for the set-up.

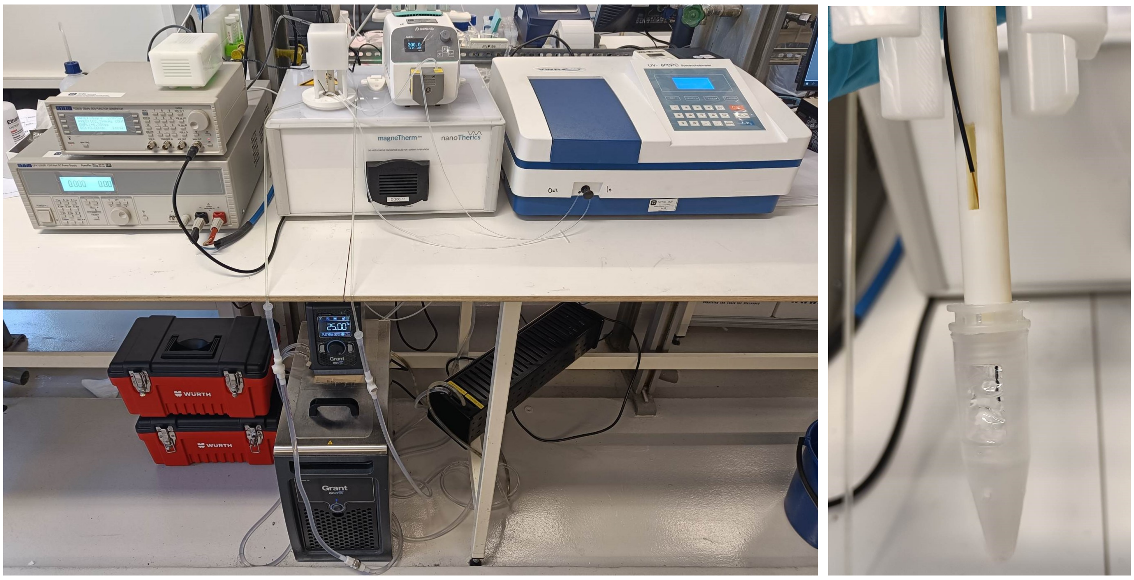

(a) magneTherm drug release set-up (b) Membrane

Figure 3.5: Figure (a) shows the magneTherm drug release set-up, consisting of a power generator (bottom left), a function generator (top left), a water cooler (floor), a UV-Vis (right), magneTherm (middle), and a release medium pump (top middle). Figure (b) shows the membrane sample holder with the temperature probe inside.

The magneTherm was connected to a VWR UV-1600PC UV/Visible Spectrophotometer, which performed a kinetic study of the release medium at the wavelength of the maximum absorbance of SA as a function of time. The interval between the UV-Vis measurements was set to 30 seconds. For the release at pH 3, the pH was adjusted as described before. The release percentage was found from the amount of drug detected in the release medium divided by the amount loaded into the NG.

The release studies are divided into static and pulsed studies. The static studies were performed for 3 hours, on all the NG samples, and without the use of an AMF. Four different release mediums were used: 25 °C and pH 6, 25 °C and pH 3, 45 °C and pH 6, or 45 °C and pH 3. The pulsed release studies were performed for 4 hours, only on FeNG10, and with the use of an AMF. The studies were performed at different temperatures, pH, field strengths, and concentrations.

3.5.2 Manual Release Studies

The manual drug release studies were performed by placing drug-loaded NGs in a dialysis membrane with MWCO of 14.5 kD into a water bath of 1 L of the release medium. The absorbance of the drug-loaded NGs was measured using UV-Vis every 30 min. The release was calculated based on the absorbance of the drug-loaded NGs before the experiment started and the absrobance of the unloaded NGs. These studies were performed using either Cyt C or SA as a model drug.

Again, the release studies are divided into static and pulsed ones, but both studies were performed on all samples. For the static studies, the release mediums and duration were the same as for the magneTherm release studies. The pulsed experiments were performed for 4 hours. For the first two hours, the pH was 6, while the temperature was 45 °C for 20 min an 25 °C for 10 min. For the last 2 hours, the pH was 3 when the temperature was 45 °C, and 6 when the temperature was 25 °C.

The materials and methods used in this work have now been introduced. The following section presents the results from the characterization of this hybrid targeted drug delivery system, and its performance is discussed.

Chapter 4

Results and Discussion

The findings of this project will be presented in several sections. Firstly, Section 4.1 will compare the NP properties. AuER was incorporated into AuNG10, while cNC was incorporated into FeNG10. The stimuli-responsiveness of these hybrid NGs and the bare NGs was compared in Section 4.2. In Section 4.3, drug loading using SA and Cyt C was compared. Lastly, Section 4.4 presents the drug release studies.

4.1 Nanoparticle Properties

In this section, the properties of the NPs will be examined and evaluated based on their potential within the targeted drug delivery system. The AuER sample was synthesized using a seeded growth method [90], while IONP samples were synthesized through two different thermal decomposition synthesis routes [10, 11]. This section will focus on two essential properties of the particles. Firstly, the particles had to be successfully incorporated into the NGs. To assess this, the colloidal stability of the particles was proven essential and was analyzed using the Zetasizer. Secondly, high heating efficiency was crucial. While the heating efficiency of AuER was not characterized, the absorbance peaks were identified using UV-Vis. For the IONPs, the SAR was characterized using the magneTherm. Equation 2.21 predicts this value to scale with the saturation magnetization, characterized by VSM, and the dry diameter of the particles, characterized by S(T)EM. Therefore, these parameters will be discussed in the following sections.

4.1.1 Chemical Analysis

As an initial study, FTIR was used to analyze the functional groups on the particle surfaces, the bonding between the particles and these functional groups, and to confirm the formation of magnetite NPs in the IONP samples. Figure 4.1 displays the FTIR spectra obtained for the NP samples. The samples were presented in Sections 3.2.1 and 3.2.2, where AuER refers to the sample with gold etched nanorods, NS denotes the sample with iron oxide nanospheres synthesized using TREG, and the NC samples are iron oxide nanoclusters synthesized using a 4:1 ratio of TREA:TREG. mNC was washed using magnetic separation, while cNC was cleaned using centrifugation.

AuER had two strong peaks around 2900 cm^{-1} and some smaller peaks around 1500, 950, and 700 cm^{-1}. The three IONP spectra were similar: a band between 3600 and 3000 cm^{-1}, small peaks around 2900 cm^{-1}, multiple peaks between 1600 and 1000 cm^{-1}, and strong peaks at 580 and 390 cm^{-1}.

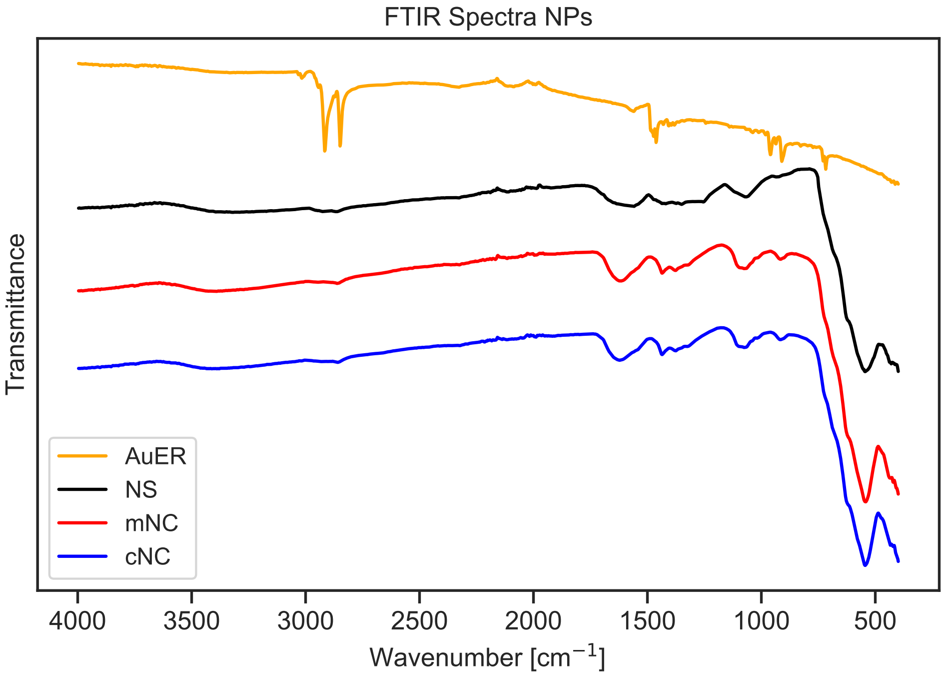

Figure 4.1: FTIR spectra of the NP samples. The transmittance was measured as a function of the wavenumber.

The FTIR spectrum of AuER confirmed the presence of CTAB on the AuNP surface and the binding of the CTAB head to the AuNPs. The spectrum exhibited a strong similarity to the FTIR spectrum obtained by de Barros et al. for AuNPs synthesized similarly [41]. In their study, de Barros et al. attributed the observed peaks to the presence of CTAB on the particle surfaces. This was confirmed by comparing the AuNP spectrum with the spectrum of pure CTAB. The molecular structure of CTAB is shown in Figure 2.6. The two strong peaks around 2900 cm^{-1} corresponded to the symmetric and asymmetric stretching, respectively, of the $-CH_2-$ groups of the hydrophobic CTAB tail. The peaks around 700 cm^{-1} were explained by the rocking motion of the -CH_2- groups in the CTAB tail. These vibrations were retained and not hindered when the CTAB was functionalized onto the AuNPs, indicating that the tails did not interact with the particle surface. The peaks around 1500 cm^{-1} were attributed to the asymmetric and symmetric C$-$H scissoring of the CH_3-N^+ group, while the peaks around 950 cm^{-1} were caused by the $C-N^+$ stretching of the hydrophilic CTAB head. These peaks exhibited slight shifts and lower intensities than in the spectrum of pure CTAB, indicating their binding to the particle surface. [41]

The NS, mNC, and cNC samples had FTIR spectra corresponding to magnetite, with sharp peaks at 580 and 390 cm^{-1}. Magnetite can be differentiated from other iron oxide phases using FTIR. The crystal structure of magnetite, Fe_3O_4, was introduced in Section 2.3, having an inverse spinal structure with Fe^{3+} and Fe^{2+} ions on the octahedral sites, and Fe^{3+} ions on the tetrahedral sites [22]. The FTIR spectrum of magnetite has characteristic sharp peaks at around 580 cm^{-1} due to the $Fe-O$ stretching vibration in the tetrahedral and octahedral sites [10, 53, 60], and in 390 cm^{-1} due to $Fe-O$ stretching in in octahedral sites [53, 60]. Separate iron oxide phases have different peaks, where maghemite has peaks at 630, 590, and 430 cm^{-1}, and goethite has peaks at 3100, 890, and 800 cm^{-1} [53, 59]. However, note that the peaks can be slightly shifted in the FTIR spectra, which can make magnetite and maghemite hard to differentiate using this technique.

The resemblance between the peaks of the NS spectrum and that obtained by Maity et al. indicated the successful incorporation of TREG onto the surfaces of the particles in the NS sample [10]. In addition to the characteristic peaks of magnetite, the NS spectrum exhibited peaks at around 2950-2850, 1600, 1450, 1350, 1250, and 1060 cm^{-1}. According to the work of Maity et al., on which the synthesis of the NS sample was based, these peaks corresponded to the $C-H$ stretching, $O-H$ stretching, $C-H$ bending, $C-O$ bending, and $O-H$ bending vibration, respectively, from the TREG absorbed to the particle surfaces [10]. Furthermore, the band between 3600 and 3000 cm^{-1} was explained by the $O-H$ stretching vibration of water molecules, and TREG absorbed to the particle surfaces.

The FTIR spectra of mNC and cNC had similar peaks as NS, despite the 4:1 ratio of TREA:TREG. TREA has characteristic peaks at 3254 and 3248 cm^{-1} when functionalized onto NPs due to N–H asymmetric and symmetric stretching vibrations [114], which were not found in the mNC and cNC spectra. This indicates that the TREA was not present on the surface of the clusters, but inside them. TREG is a chain-like stabilizing agent that sterically and electrostatically stabilized the particles. Adding TREA made the particles cluster together to reduce their surface energy, as they became unstable [11]. Therefore, the TREA could be inside the clusters, holding the particles together with its three arms, while TREG was outside. This would explain why the TREA groups were not visible in the FTIR spectra of mNC and cNC.

To conclude, the FTIR spectra confirmed the presence of CTAB on the surface of the AuERs and TREG on the IONPs. The TREA did not contribute to peaks in the FTIR spectra of the NC samples. The spectra indicated the formation of magnetite for all three IONP samples.

4.1.2 Size and Stability

The size and stability of colloidal particles are crucial factors for their performance in biomedical applications, as presented in Sections 2.1.2 and 2.1.4. Additionally, the optical properties of AuNPs, described in Section 2.2, and the magnetic properties of IONPs, introduced in Section 2.3, are strongly size-dependent. Consequently, it is essential to characterize these properties.

The morphology and dry size of the particles were analyzed using S(T)EM. Figure 4.2 shows one representative micrograph of each sample, while additional images are found in Appendix B.1. The AuER sample primarily consisted of particles with etched rod morphologies, while a smaller number of rods, squares, and some significantly smaller particles were also present. Among the IONP samples, the NS sample contained small and spherical particles, while the NC samples contained clusters of several particles. Based on the micrographs, there were no apparent differences between the size nor the shape of the particles in mNC and cNC.

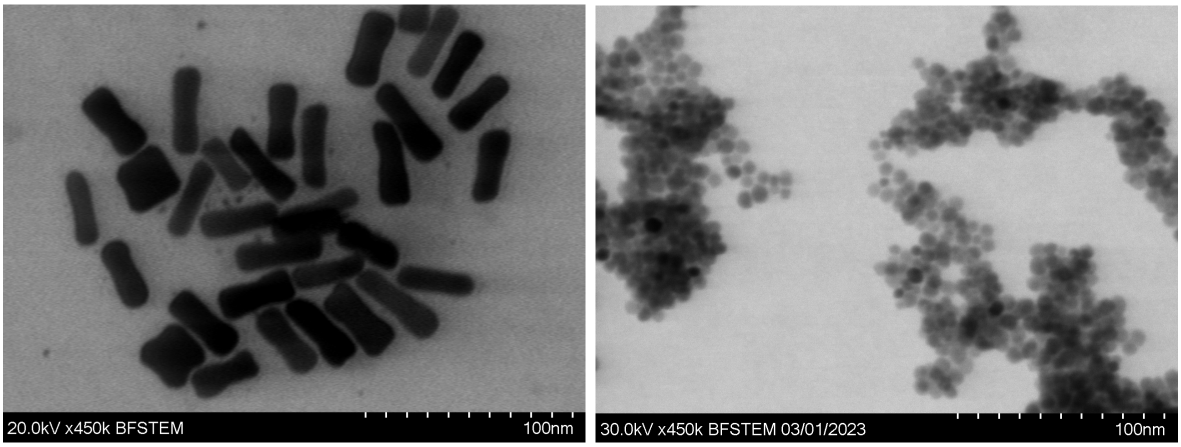

(a) AuER (b) NS

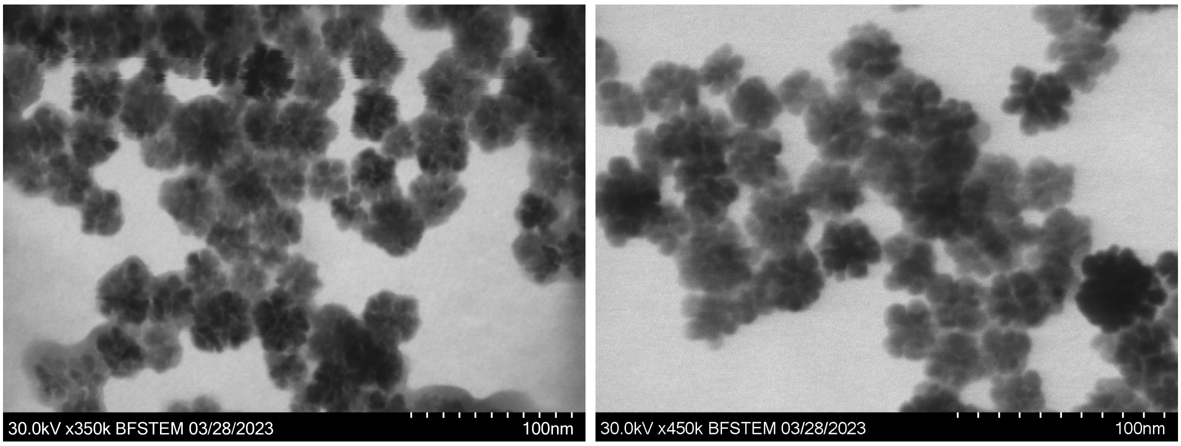

(c) mNC (d) cNC

Figure 4.2: S(T)EM micrographs of the NP samples.

The different morphologies observed in the AuER sample resulted from differences in the relative growth rates of the NP facets, as presented in Sections 2.1.3 and 2.5.1. CTAB binds to the $\{110\}$ facts, leading to an anisotropic growth [40, 41, 42]. The observed squares could have an etched rod morphology with a low aspect ratio or etched rods seen along the longitudinal axis, while the smaller particles observed could be seeds that had not grown as big as the others.

The spheres observed in the NS sample and the clusters observed in the NC samples were a result of the surface coating [10, 11]. The obtained particles were similar to what was reported by the two works of Maity et al. [10, 11]. The NS particles were stabilized by TREG, as verified by FTIR, resulting in small and spherical particles. The NC samples were synthesized using a 4:1 ratio of TREA:TREG, where the TREA reduced the stabilization effects of TREG [11]. Consequently, the particles clustered together to minimize their surface energy. The mNC and cNC samples were synthesized in the same batch, then divided into two and separated using different techniques. Consequently, the imaged particles from these samples had similar morphologies.

Table 4.1 compares the size and stability of the NPs. The dry length (L_{dry}), diameter (d_{dry}), and aspect ratio (AR) were found from 200 measured particles from S(T)EM images. The averages and standard deviations were calculated from these measurements, making the standard deviation an indication of the polydispersity of the particles. The size distributions of the counted particles are illustrated in Appendix B.1. The particles were measured manually using ImageJ [109], introducing the possibility of human error. AuER contained anisotropic particles, while the IONPs were considered close to isotropic. Therefore, L_{dry} and AR were found for AuER, while only d_{dry} was used to characterize the size of the IONPs. The diameter of the anisotropic particles in AuER was measured in the middle of the particles, while the NC diameters refer to the entire cluster, as marked in Appendix B.1. The sizes of the individual particles in the clusters were measured using 100 particles per sample and were 8 ± 2 nm for both mNC and cNC. The size distributions are found in Appendix B.1. Assuming a packing parameter of 0.74, i.e., close packing, the number of particles constituting each cluster could be approximated as 39. The d_{hyd} and PDI of the NPs were measured using DLS, and the ζ was measured using ELS. The instrument measured each parameter three times per sample and calculated the averages and standard deviations based on these measurements, making the standard deviations the deviations between the three measurements, not differences in the particle properties.

d_{hyd} was larger than d_{dry} for all samples except for AuER, but the difference was small for cNC. All samples had a positive ζ. mNC had a high PDI and low ζ, while the opposite was true for the three other samples. AuER and cNC had the lowest PDI and highest ζ. The NC samples had a significantly larger d_{dry} than NS, while mNC and cNC had identical d_{dry}. However, d_{hyd} was significantly larger for the mNC than for cNC. The particles in the clusters in mNC and cNC had identical d_{dry}, with overlapping standard deviations with the d_{dry} of NS.

Table 4.1: The dry length, diameter, and aspect ratio were measured from 200 particles using S(T)EM images, and the standard deviations indicate the polydispersity of the particles. The dry diameter of particles in the clusters was 8 ± 2 nm for both mNC and cNC, measured from 100 particles. Histograms representing the size distributions for the particles measured using S(T)EM are shown in Appendix B.1. The hydrodynamic diameter and polydispersity index were measured using DLS, while the zeta potential was measured using ELS, based on three measurements.

Sample	L_{dry} [nm]	d_{dry} [nm]	**AR**	d_{hyd} [nm]	**PDI**	ζ [mV]
AuER	39 ± 7	14 ± 4	3.0 ± 0.8	10 ± 0	0.2 ± 0.0	30 ± 1
NS	-	7 ± 1	-	217 ± 3	0.3 ± 0.0	27 ± 1
mNC	-	30 ± 6	-	409 ± 70	0.6 ± 0.2	15 ± 0
cNC	-	30 ± 6	-	55 ± 1	0.2 ± 0.0	30 ± 1

All the NP samples had a positive ζ, i.e., the particle surfaces had a positive surface charge. The positive charge of AuER was due to the Br^- ion of the CTAB functionalizing the particles dissociating in solution, making CTAB acquire a positive charge located at the N atom [41], as seen in Figure 2.6. For the NS sample, the positive charge was due to the TREG molecules on the particle surface. As explained in Section 2.5.2, TREG breaks down into an $R{-}O^-$ part that binds to the IONP surface, and a H^+ part that associates with the surface, making it positively charged [10]. For the NC samples, it was argued in Section 4.1.1 why TREG might be present on the surface of the clusters while TREA could be located within the clusters. As a result, TREG would dictate the surface charge, making the NCs positively charged. Alternatively, if the TREA were on the surface, the charge would depend on the pH of the solution. The particles were dispersed in MQ water which had a pH of 6. At this value, the TREA would carry a positive charge, contributing to the overall positive charge of the clusters. If a combination of TREG and TREA were present on the surface, this would still result in a positive surface charge.

The magnitude of the ζ indicates the electrostatic stability of colloidal particles, as explained in Section 2.1.4. For the particles to be considered electrostatically stable, ζ should be higher than 30 mV [57]. AuER and cNC had a ζ at this value, while NS was slightly below, and mNC was far below. Both NS and mNC were magnetically separated, and had lower ζ than AuER and cNC, which were centrifuged. By centrifugation, sedimented particles were collected. By magnetic separation, the particles that were the most attracted to the magnet were collected, which could be the most magnetic ones, the least colloidally stable ones, or a combination of the two. The particles were challenging to collect with magnetic separation, indicating that the magnet was too weak to collect the more stable or less magnetic particles. The method of separation was the only difference between mNC and cNC,demonstrating that the magnetic separation collected particles with reduced electrostatic stability, as seen from the lower ζ of mNC. Comparing NS and cNC, the latter was more electrostatically stable, which could be due to the difference in separation. However, since the synthesis routes were different, one cannot conclude this was the only reason. Comparing NS and mNC, which both were magnetically separated, NS was more electrostatically stable. This could be explained by the reduced stabilizing effect of TREA compared to TREG, and the reduced amount of TREG in the mNC sample. Maity et al. reported a ζ of +40 mV for the particles made similarly to NS [10], which is higher than what was obtained in this work. However, the pH is an essential factor for the measured ζ, and Maity et al. did not report the pH of the measurement. Nor did they report the ζ for the particles made similarly to mNC [11]. Even though only AuER and cNC had a value of ζ that indicated electrostatic stabilization, the NS and mNC could still be colloidally stable through the steric stabilization effect of TREG [25].

The d_{hyd} estimated for AuER using DLS was misleading due to the anisotropic morphology of the particles in the sample. DLS estimates the d_{hyd} using the Stokes-Einstein equation, defined in Equation 2.14, from the translational diffusion of the particles. Since rods have a rotation in solution [95], and the Stokes-Einstein equation gives d_{hyd} corresponding to a sphere with the same translational diffusion as was measured, rods are not accurately measured using DLS. The d_{hyd} does not correspond to the length nor diameter of anisotropic particles but is often correlated with the length of measured rods [29]. Two particle populations were observed from the DLS size distribution spectra in Appendix D.1, one around 2 nm and the other around 45 nm. These could correspond to the length and width of the rods, where the inaccuracy is a result of the assumptions for the DLS technique not being fulfilled. Since both d_{hyd} and the PDI were measured using DLS, these properties will not be considered further for AuER since they were misleading.

The increased d_{hyd} compared to d_{dry} was most likely a result of the surface coating and hydrated layer for cNC, but colloidal instability for NS and mNC. The d_{hyd} of coated IONPs in solution generally exceeds d_{dry} due to the inclusion of any surface coating and the hydrated layer surrounding the particles [47]. Firstly, very few particles were measured using S(T)EM compared to using DLS, which could cause differences in the results. Additionally, intensity-weighted DLS measurements were conducted, causing larger particles to overshadow smaller ones [21]. These factors explain the difference between d_{hyd} and d_{dry} for cNC, but for NS and mNC the differences were significantly larger. Maity et al. reported d_{hyd} of 13 nm for NS and 187 nm for mNC [10, 11]. The large d_{hyd} of NS and mNC could result from colloidal instability of these particles. In cases where aggregated particles moved together, DLS could count them as a individual particle, whereas d_{dry} was determined from individual particles in S(T)EM images. NS and mNC exhibited a lower ζ than cNC, which could explain the higher d_{hyd}. However, NS showed a much higher d_{hyd} value than implied by its ζ.

The polydispersities of the particles were similar to what is typically reported in the literature for IONPs synthesized using thermal decomposition [65], and lower than IONPs synthesized using co-precipitation [56, 74]. A low PDI is desirable for applications that require uniform particle properties. A PDI below 0.05 is generally considered highly monodisperse, below 0.3 is acceptable, and above 0.7 is unsuitable for analysis by DLS [85]. All the IONP samples had a PDI below 0.7, while only cNC was below 0.3 and even 0.05, indicating a very good monodispersity. Maity et al. reported a PDI of 0.127 for mNC using DLS, but did not report a value for NS [10, 11].

The d_{dry} of NS was significantly smaller than that of the clusters in the NC samples, explained by the clusters consisting of several particles. However, NS was around the same size as the particles in the clusters, having overlapping standard deviations. The NC samples had half the reaction time of NS, making the window for particle growth shorter. However, TREA has an increased boiling point compared to TREG, which has been found to give larger particle diameters [51]. The sum of these two factors resulted in similarly sized particles. However, it should be noted that measuring the individual particles within the clusters was challenging, making the particles on the surface, which possibly had an extended time to grow, counted more often than those in the middle of the clusters. Consequently, the sizes of the particles in the clusters should be interpreted cautiously, serving as an approximation rather than an exact value. When comparing the d_{dry} of the IONP samples to that of Maity et al., both the 7 nm of NS and the 30 nm of NC were small compared to the 11 and 44 nm obtained by Maity et al. for the two samples, respectively [10, 11].

According to the particle size distributions in Appendix B.1, all the particles that were counted in NS and in the clusters in the NC samples had a d_{dry} below 20 nm, implying SPM properties based on the size [67]. The M_S of SPM NPs is assumed to increase with increasing dry diameter [65], and the SAR parameter scales with the third power of the radius [58], highlighting the importance of size for magnetically heating particles.

Due to its anisotropy, the size of AuER was difficult to compare directly to the IONP samples. L_{dry} of AuER was larger than d_{dry} of all the IONP samples, while d_{dry} of AuER was higher than the d_{dry} of NS and the NC particles, while lower than the d_{dry} of the NC clusters. The obtained length, diameter, and AR of AuER were similar to what was measured for the same particles in a previous study [30]. The particles in AuER were smaller than 100 nm, so the quasi-static approximation was valid, and LSPR properties could be expected [26]. The LSPR properties of the AuER sample will now be considered.

4.1.3 Optical Properties of Gold Nanoparticles

As presented in Section 2.2, AuNPs can exhibit optical properties which result in strong absorbance at specific wavelengths. Therefore, the absorbance spectrum of AuER was obtained using UV-Vis to identify any LSPR peaks. The resulting spectrum is illustrated in Figure 4.3. Three peaks are seen, at 518, 596, and 748 nm, with the latter one being the strongest.

The LSPR properties of AuER arise from the small size of the particles, as measured using S(T)EM, giving a large number of coherently oscillating surface electrons [26].

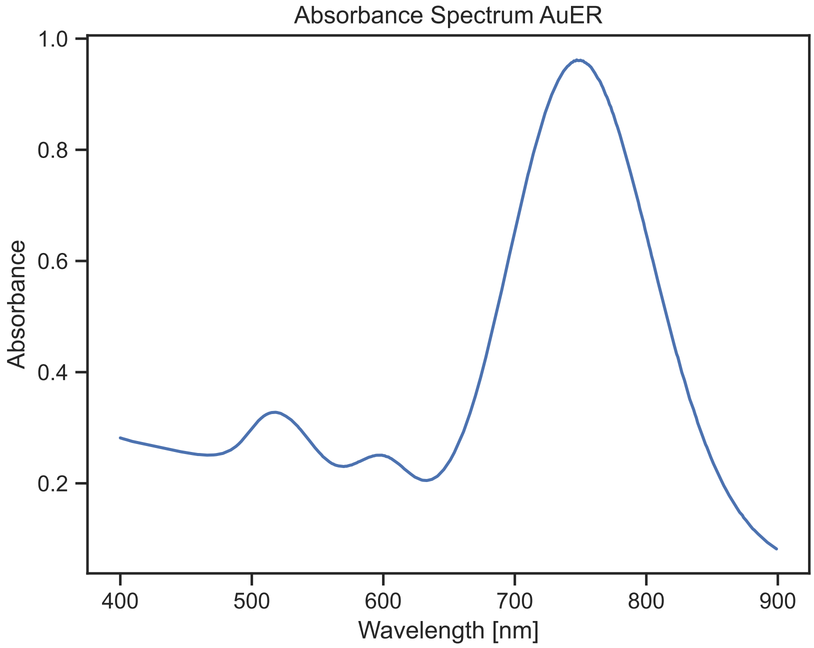

Figure 4.3: Absorbance spectrum of AuER, characterized using UV-vis. The peaks were located at 518, 596, and 748 nm.

The wavelength of absorbance scales inversely with the size due to a larger charge separation for bigger particles, requiring less energy [12]. Consequently, the three LSPR peaks corresponded to three axes of AuER, with the strongest peak at 748 nm corresponding to the longitudinal axis, i.e., the length of the particles. The peak at 518 nm was the second strongest and corresponded to the transverse axis, i.e., the diameter. The peak at 596 nm was the weakest and could correspond to some axis between the length and diameter resulting from the etched rod morphology. Note that the peaks depend on the chemical environment and could shift if the medium was changed from water to blood [26].

The strongest peak of AuER was in the NIR region and has the potential to be used for in vivo heating applications due to the low absorption of biological tissue at these wavelengths [43, 45]. Additionally, the strong absorbance indicates potential for imaging applications [12]. Having established the potential of AuER for optical heating, the magnetic properties of IONP in the context of magnetic heating will be considered.

4.1.4 Magnetic Properties of Iron Oxide Nanoparticles

The magnetic properties of magnetite NPs were introduced in Section 2.3, and their importance for magnetic heating applications was underlined in Section 2.5.2. Equation 2.21 demonstrates how the heating efficiency of magnetic NPs scales with the square of the M_S. Hence, this parameter was characterized using VSM, together with the remnant magnetization (M_R) and coercivity (H_C). The number N of blocked μ is also interesting. As seen from Equation 2.11, normalizing M_S by M_R will remove the intersample variation of μ, allowing for comparison of M_R between different samples. Therefore, this M_R/M_S ratio will be used to compare the number of blocked μ between the IONPs.

Table 4.2 shows the magnetic properties of the IONP samples as measured using VSM. Three measurements were performed for each sample, and the averages and standard deviations were calculated from these measurements. Figure 4.4 displays one of the magnetization curves for each sample in response to a magnetic field applied in a cycle, starting and ending at 10 kOe. The inserted figure shows the hysteresis of the magnetization around the origin where no field was applied. Normalized magnetization curves are found in Appendix C.1 for comparison of the curve shapes. mNC had the highest and NS had the lowest M_S, M_R, and H_C among the samples. The M_R/M_S ratio was 0.014 ± 0.003 %, 2.2 ± 0.44 %, and 1.7 ± 0.25 % for NS, mNC, and cNC, respectively.

All the samples were SPM, but the NC samples had a small hysteresis which could result from some particles being thermally blocked at room temperature. The magnetization curves resembled the SPM curve illustrated in Figure 2.5, and the size of all the counted particles were below 20 nm, as seen from the histograms in Appendix B.1. These factors would indicate SPM particles in all three IONP samples [67]. The hysteresis was negligible for NS, but both NC samples exhibited a small hysteresis, indicating that these samples were not perfectly SPM. Liu et al. have described magnetite NPs with a d_{dry} of 19 nm and a M_R/M_S of 3 % as exhibiting FM behavior [58]. On the other hand, Maity et al. described both NS and mNC as SPM, but did not provide M_R or H_C values for either of the samples [10, 11]. This finite hysteresis of the NC samples might result from magnetic interactions between the particles in the clusters. Dipolar interactions between magnetic NPs in samples with high concentrations have been shown to increase the blocking temperature due to increasing magnetic anisotropy, leading to increased H_C and M_R/M_S [66, 68]. Inside the clusters, the effective concentration of particles was high, most likely resulting in strong magnetic interactions between the particles, leading to a higher number of blocked μ compared to the NS sample, despite the similar particle sizes.

Table 4.2: Saturation magnetization, remnant magnetization, and coercivity of the IONPs. The parameters were measured using VSM, and were calculated based on three measurements per sample.

Sample	M_S **[emu/g]**	M_R **[memu/g]**	H_C **[mOe]**
NS	48.9 ± 0.7	7 ± 2	149 ± 32
mNC	70.9 ± 1.2	1584 ± 341	6608 ± 1579
cNC	68.9 ± 0.7	1194 ± 177	4913 ± 158

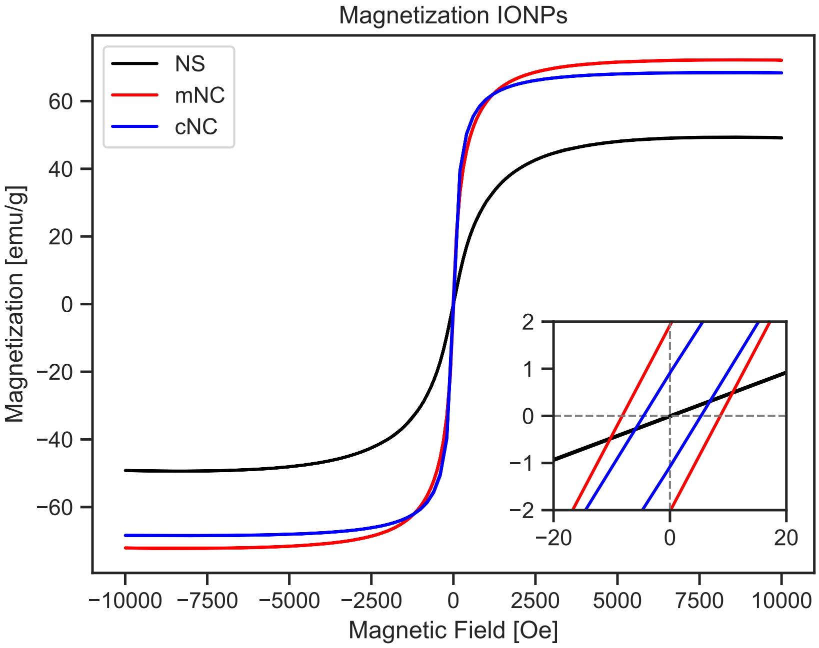

Figure 4.4: Magnetization as a response to an applied magnetic field. The inserted figure shows a closer look at the origin to illustrate the hysteresis. Normalized magnetization curves are shown in Appendix C.1 to illustrate the curve shapes.

All the IONPs had a M_S below the 92 emu/g of bulk magnetite [10], presumably resulting from spin canting, oxidation, and non-magnetic coating. Magnetite NPs have a reduced M_S with respect to bulk magnetite, normally attributed to the lower ordering of the surface magnetic moments [56], estimated to give a 0.6 nm thick non-magnetic shell around the particle surfaces [55]. This spin canting results in size-dependent M_S of NPs due to their high surface-to-volume ratio [55, 66]. Furthermore, the magnetization of coated particles is generally further reduced due to the coating changing the surface states of the IONPs [57], shielding of the magnetic core [58], and adding non-magnetic weight, which reduces the M_S which is normalized by mass. A last possible explanation for the reduced M_S compared to bulk magnetite was the possibility of oxidation of the particle surfaces, forming maghemite, which has a lower M_S than magnetite, or the formation of other less magnetic metastable iron oxide phases [57], which is explained by Ostwald's rule of stages [22]. A combination of these effects was most likely the reason for the reduced M_S of the NPs compared to that of the bulk.

The IONPs in this work had reduced M_S compared to what was obtained by Maity et al. The M_S of NS was significantly reduced compared with the 65 emu/g reported by Maity et al [10]. This could be a result of the difference in sizes, where 7 nm was obtained in this work compared to 11 nm reported by Maity et al. The M_S of NS was in the same range as what is reported for similarly sized magnetite NPs prepared using thermal decomposition in the literature [58], while differences can occur due to for example surface coating. mNC had a M_S close to the 75 emu/g reported by Maity et al. [11]. No size of individual particles was reported by Maity et al., only cluster size, making a comparison of the particles challenging. However, the reported cluster size was bigger than the one found in this work. The M_S of cNC was lower than mNC, which could be explained by magnetic separation favoring the most strongly magnetic particles compared to centrifugation. mNC was separated similarly as Maity et al. did, explaining why this sample was closest to the value they reported.

The NC samples had high M_S compared to what has been reported in the literature for individual particles [48, 58], and compared to NS. It has been established that the particles had similar d_{dry}, so this difference should not result from size. A description of mechanisms explaining the effect of clustering on M_S could not be found in the literature. However, the following explanations are proposed based on the previously explained mechanisms behind the reduced M_S of NPs compared to bulk magnetite. Firstly, the samples had a different surface coating. While the amounts and molecular weights of the coatings were similar, making the added non-magnetic weight the same, the particles inside the clusters could have had a lower concentration of coating molecules on the surface, limiting the reduction of M_S. Alternatively, it is possible that magnetic interactions could have an effect on spin canting, reducing the non-magnetic dead layer. A last explanation is that the oxidation of the particles inside the clusters could have been reduced compared to that of individual particles, as the surface would have been shielded.

The magnetization curves obtained using VSM were fitted to the Langevin function [62], found in Equation 2.16, in order to approximate the magnetic moment and magnetic diameter of the NPs. The results from the fit are tabulated in Table 4.3, and Figures showing the experimental data together with the fitted curves are found in Appendix C.2. Each of the three VSM measurements was fitted to the Langevin function, and the averages and standard deviations in the table are based on these three fittings. The M_S obtained from the Langevin fitting was slightly overestimated compared to the VSM results for all three samples. This was most likely an error in the fitting, and will not be further discussed due to the small magnitude of the error. μ and d_{mag} were larger for cNC than mNC. d_{mag} was the same as the d_{dry} measured in S(T)EM for NS, but higher for the NC samples when compared to the individual particles and not the clusters.

The estimated μ and d_{mag} resulted from the shapes of the magnetization curves. From the Langevin function in Equation 2.16, a steeper curve, i.e., increased χ, results from higher μ. The shape of the curves of the IONP samples can be compared using the normalized magnetization curves in Appendix C.1. cNC had the steepest curve, closely followed by mNC. As explained in Section 2.5.2, d_{mag} was calculated from μ by assuming spherical magnetite particles, which was verified by S(T)EM and FTIR. Consequently, the differences in d_{mag} result directly from the differences in μ, and are

Table 4.3: Parameters obtained by fitting the magnetization curves from Figure 4.4 to the Langevin function, defined in Equation 2.16. The values were estimated based on three measurements per sample.

Sample	$\boldsymbol{M_S}$ **[emu/g]**	$\boldsymbol{\mu}$ **[Am^2]**	$\boldsymbol{d_{mag}}$ **[nm]**
NS	51.6 ± 0.5	$9 \cdot 10^{-20} \pm 8 \cdot 10^{-21}$	7 ± 0
mNC	71.1 ± 2.1	$3 \cdot 10^{-19} \pm 2 \cdot 10^{-20}$	10 ± 0
cNC	69.4 ± 0.3	$4 \cdot 10^{-19} \pm 2 \cdot 10^{-20}$	11 ± 0

due to different curve shapes.

Comparing the estimated d_{mag} to the measured d_{dry}, the approximation was a perfect fit for NS, despite d_{dry} including the assumed non-magnetic layer on the surface of the NPs [55, 62]. However, d_{mag} was overestimated for the NC samples, particularly cNC when comparing the values to the sizes of the particles constituting the clusters. Firstly, as mentioned, the exact size measurements of the individual particles constituting the clusters must be used critically and not as exact sizes. Secondly, assumptions for this Langevin approximation are spherical and non-interacting particles [62]. The assumed magnetic interactions between the particles in the clusters would result in higher χ [66], and consequently, an overestimation of μ and d_{mag} by the Langevin fit.

In conclusion, mNC had the highest M_S, closely followed by cNC. The NC samples had increased H_C and M_R values in addition to high χ, which could be explained by interactions between the particles in the clusters blocking some magnetic moments. The following section will discuss how this affected the heating properties of the particles.

4.1.5 Heating Efficiencies of Iron Oxide Nanoparticles

This section will focus the heat generation of the IONPs when exposed to an AMF. As introduced in Section 2.5.2, the heating efficiency can be characterized using the SAR parameter obtained from hyperthermia measurements performed in the magneTherm. Before the studies on the IONPs were conducted, some preliminary experiments were performed using the same setup to optimize the studies.

Preliminary Studies

Firstly, water temperature under the influence of an AMF was measured to normalize the heating of the magnetic NPs. Figure 4.5 shows the water temperature as a function of time for the Brezovich and the Instrument limit. The temperature was increased by 0.29 °C for the Brezovich limit and 1.62 °C for the Instrument limit. These temperature increases were subtracted from the SAR value calculations for all subsequent measurements. Despite this normalization, the non-magnetic heating might have induced minor errors in the hyperthermia measurements performed in the magneTherm due to variations between measurements. The cause of the water heating was unknown but might have been caused by the coil heating up when the magnetic field was activated. Although the system was isolated, it was not perfectly adiabatic, and the heat generated by the coil could have affected the sample temperature.

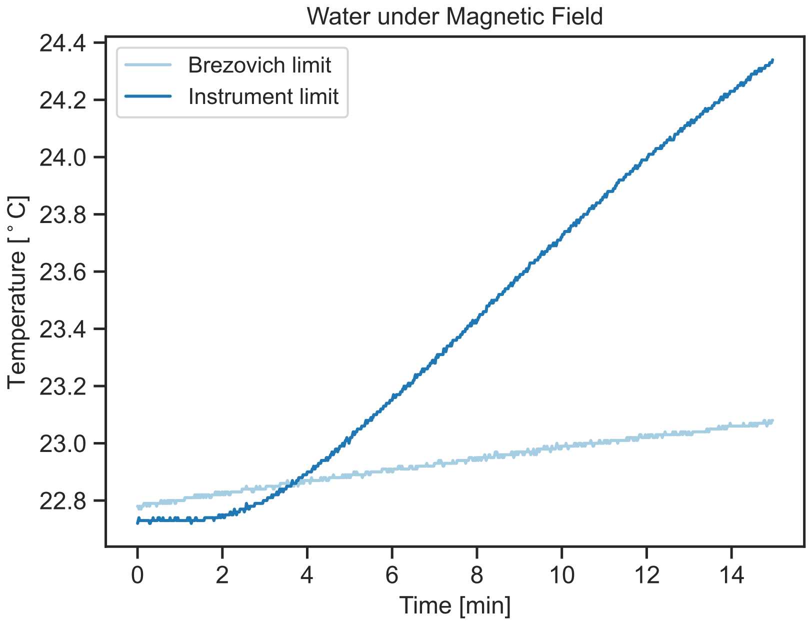

Figure 4.5: Heating of water using an AMF with 162 kHz and 38 Oe (Brezovich limit) and 190 Oe (Instrument limit). The temperature increase was 0.29 °C for the Brezovich limit and 1.62 °C for the Instrument limit.

Secondly, specific field strength and frequency combinations were excluded due to poor heat generation. The magneTherm provided six AMF frequencies, which combined with corresponding field strengths fulfilling the criteria set by the Brezovich and Instrument limits outlined in Sections 2.5.2 and 3.3.5, resulted in 12 different field strengths and frequency combinations. Initial experiments revealed that the heating efficiency was almost negligible for the three highest frequencies, corresponding to the three lowest magnetic field strengths, for both limits. This observation aligned with the established dependency of SAR on f and H^2 [69], as reported with consensus in the literature and represented by Equations 2.20, 2.21, and 2.23. As a result, only the three lowest f corresponding to the three highest H for each limit were utilized for the hyperthermia studies presented in the following section.

Effect of Field Strength and Frequency

To investigate the effect of field strength and frequency on the heating of the IONP samples, the sample concentration was kept at 1 mg/mL for all measurements. AMFs with the frequencies selected in the preliminary experiments were applied to the IONPs, combined with the corresponding field strengths decided by the Brezovich and Instrument limits. The SAR values were calculated using Equation 2.22, based on the measured temperature slopes between 5 and 200 seconds, subtracting the temperature slope of water for the corresponding $H \cdot f$ limit. However, the water temperature increase was not subtracted from the temperature figures. Table 4.4 shows the calculated SAR values, while Figure 4.6 shows the temperature of the samples as a function of time. The solid lines indicate AMFs with a frequency of 102 kHz, the dotted lines 154 kHz, and the dashed lines 162 kHz.

Table 4.4: Calculated SAR for the IONPs using different combinations of frequencies and field strengths, using Equation 2.22.

$\boldsymbol{H \cdot f}$ **limit**	$\boldsymbol{f}$ **[kHz]**	$\boldsymbol{H}$**[Oe]**	**NS [W/g]**	**mNC [W/g]**	**cNC [W/g]**
Brezovich	162	38	0	23	43
	154	40	0	82	175
	102	60	0	32	181
Instrument	162	190	22	164	484
	154	200	9	192	427
	102	300	24	213	406

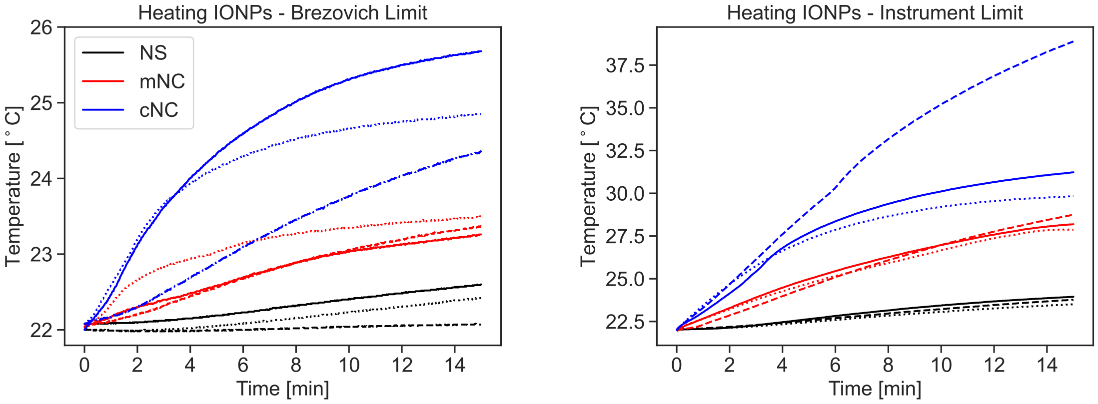

(a) Brezovich limit (b) Instrument limit

Figure 4.6: Heating of IONPs, using the Brezovich and Instrument limits. The solid lines had a frequency of 102 kHz, the dotted lines 154 kHz, and the dashed lines 162 kHz. Table 4.4 shows the corresponding field strengths for each limit. The figures should be seen with respect to Figure 4.5, showing the heating of water at 162 kHz and 38 Oe (Brezovich limit), and 190 Oe (Instrument limit).

The Instrument limit gave a higher SAR than the Brezovich limit for all the measurements. NS had no heating efficiency at the Brezovich limit and very low values at the Instrument limit. Both mNC and cNC had high SAR values, but the latter had significantly higher ones. cNC had the highest temperature increases with an increase of 3.7 °C for the Brezovich limit and 16.9 °C for the Instrument limit. No field strength and frequency combination consistently gave the highest SAR for all samples.

As presented earlier, the Brezovich limit was based on patient discomfort upon exposure to an AMF around the torso for an hour [76], but many studies argue that this limit can be exceeded by up to ten times when applying the field to a smaller body part or for a shorter time [69, 74, 77, 78]. In this work, the Instrument limit exceeded the Brezovich limit by five times. Consequently, the results obtained using the Brezovich limit could be obtained with the AMF applied to around the torso for an hour, while the results obtained using the Instrument limit are limited to shorter exposure times than one hour or smaller body parts than the torso.

The heat generated by the particles would most likely not be dangerous to cells. All temperature increases above 9 °C would give irreversible damage to healthy cells, assuming a starting temperature at 37 °C [80, 81]. The temperature increased more than 15 °C by cNC at 162 kHz and 190 Oe, while all the other measurements had an increase of 9 °C or lower. Since a non-adiabatic set-up was used for the experiments, heat dissipation mechanisms lowered the temperature increase when the local temperature rose above the ambient temperature [79]. This can be seen from the non-linear curves, which was why SAR was calculated from only the initial slopes. However, the heating in human tissue would be lower since the heat dissipation would be stronger than in this set-up [2, 79]. Additionally, for the hybrid drug delivery system, a lower concentration of magnetic NPs than 1 mg/mL would be used, as only a small amount would be incorporated into the NGs.

All the IONP samples exhibited magnetic heating properties when using the Instrument limit, and the NC samples were heating when using the Brezovich limit as well. The higher SAR values obtained using the Instrument limit compared to the Brezovich limit were predicted by the H^2 and f dependency of SAR from Equations 2.20 and 2.21 [58]. However, the increase was not as high as indicated by the equations. This could be because the heat dissipation increased when the temperature difference between the sample and the environment increased due to the non-adiabatic set-up.

As explained in Section 2.3, SPM NPs exposed to an AMF mainly generate heat through Brownian and Néel relaxation, dissipating thermal energy through shear stress and rearrangement of the magnetic moment, respectively [58, 69, 72]. τ_B, τ_N, and τ were approximated for the samples using Equations 2.17, 2.18, and 2.19, respectively, to estimate the dominating relaxation mechanism for each sample [69]. The approximated values are found in Appendix E.2 together with the parameters used for the approximations. Néel relaxation presumably dominated for all three samples, as expected for particles at these sizes [69]. τ_B would be underestimated in this system compared to in blood due to its dependency on viscosity. Still, since Brownian relaxation was not the dominating mechanism, and heating experiments performed in mediums simulating blood show the SAR to be similar as in water [58], this should be a negligible effect. τ_N would be underestimated for the NC samples, particularly mNC, due to the presumed magnetic interactions increasing K. This would lead to a higher τ for the NC samples, particularly mNC, and a higher contribution of Brownian relaxation to the heat generation.

FM NPs exposed to an AMF can generate heat proportional to the area of the hysteresis loop [72]. This mechanism increases with increasing M_R and H_C and is generally dominating for particles above 100 nm but still significant for particles around 15 nm, despite the relaxation mechanisms normally dominating for particles at this size [69]. It has been proposed that an increased SAR can occur just above the transition from SPM since both Néel and hysteresis loss contribute to heat generation, but this will vary widely from system to system and is not a generalized rule [69]. The contribution of the hysteresis loss to the heating efficiency was approximated for the samples using M_R and H_C, and is given in Appendix E.2. This approximation indicates negligible hysteresis loss for NS, but a significant contribution for the NC samples since they were not perfectly SPM.

NS had lower SAR than the NC samples, which according to Equations 2.20 and 2.21 could be a result of the r, M_S, χ, and τ of the particles [58]. r was similar for the samples, according to S(T)EM, while M_S and χ were significantly higher for the NC samples, according to the VSM data. The dependence of SAR on τ is more complex, where SAR is optimized when $\omega \cdot \tau = 1$, where $\omega = 2\pi f$ [69]. Since the approximated τ was uncertain for the NC samples due to the unknown contribution from the interactions on K, the $\omega \cdot \tau$ values for these samples were not known. A last difference between NS and the NC samples was the contribution of heat generated from the hysteresis loss of the NC samples [69, 72]. Consequently, the higher SAR of the NC samples could result from the increased M_S and χ, hysteresis loss, and possibly an improved combination of f and τ.

Comparing mNC and cNC, the cNC had significantly higher SAR, despite the samples having similar r, and mNC having higher M_S and higher approximated hysteresis loss based on M_R and H_C. On the other hand, cNC had higher χ, according to VSM results. Additionally, mNC had lower colloidal stability than cNC, which has been found to reduce SAR significantly [58], and it was observed that the mNC particles separated during the time of the measurement. A final contribution to the higher SAR of cNC could be the increased τ of mNC due to the higher magnetic anisotropy of this sample, indicated by the higher hysteresis. This would render cNC closer to fulfilling $\omega \cdot \tau = 1$ for the f studied in this work. To conclude, the higher SAR of cNC could result from the higher χ, higher colloidal stability, and probably a more optimal τ and f combination.

The $\omega \cdot \tau$ criterion could explain why the SAR did not increase with increasing H and decreasing f within each $H \cdot f$ limit, as predicted by Equations 2.20 and 2.21. The lack of common trends for the three samples when comparing the different H and f, could result from individual improved combinations for the different samples. This could be due to different τ between the samples, as the optimal frequency depends on the τ [69].

As presented in Section 2.5.2, comparing SAR values between different studies is challenging since the value depends strongly on the field strength and frequency used. To illustrate this, Maity et al. obtained a SAR of 885 W/g using the 1 mg/mL of the sample corresponding to NS, using an AMF with 20 MHz, but not stating the field strength [10]. Using 1 mg/mL of the sample corresponding to the mNC sample, they obtained a SAR of 500 W/g, using an AMF with 240 kHz and 1118.4 Oe [11], giving a $H \cdot f$ of 44 times the Brezovich limit. Consequently, the ILP parameter defined in Equation 2.23 will be used to compare the heating efficiencies obtained in this work with values found in the literature.

ILP values from the literature were calculated and presented in Appendix E.1, while values from this work are tabulated in Table 4.5. ILP values obtained using the Brezovich limit were higher than when using the Instrument limit for mNC and cNC. The ILP of NS using the Brezovich limit was zero due to the zero SAR obtained. The studies in the literature generally use much higher magnetic field strengths than what is used in this work [11, 65, 74, 75, 77].

Table 4.5: Calculated ILP for the magnetic nanoparticles for different combinations of frequencies and field strengths, using Equation 2.23 and the values in Table 4.4.

$\boldsymbol{H \cdot f}$ **limit**	$\boldsymbol{f}$ **[kHz]**	$\boldsymbol{H}$ **[Oe]**	**NS** $[\mathbf{nHm^2kg^{-1}}]$	**mNC** $[\mathbf{nHm^2kg^{-1}}]$	**cNC** $[\mathbf{nHm^2kg^{-1}}]$
Brezovich	162	38	0.0	16.1	29.9
	154	40	0.0	53.8	114.8
	102	60	0.0	14.0	78.8
Instrument	162	190	0.6	4.4	13.1
	154	200	0.2	4.9	11.0
	102	300	0.4	3.6	6.9

The higher ILP obtained using the Brezovich limit compared to the Instrument limit for the NC samples was a result of SAR increasing with less than H^2, presumably because of stronger heat dissipation at increased temperatures.

Maity et al. obtained an ILP of 0.3 nHm^2/kg for the mNC sample [11], which was significantly lower than what was obtained for the same sample in this study, but around the values of NS using the Instrument limit. Narayanaswamy et al. obtained 0.24 nHm^2/kg for polyethylene glycol-coated IONPs [74], similarly to NS. Piñeiro-Redondo et al. obtained 4.3 nHm^2/kg with polyacrylic acid-coated IONPs [75], around what was obtained for mNC using the Instrument limit. Values up to 24.3 nHm^2/kg have been reported for bacterial magnetosomes by Hergt et al. [77], which was higher than what was obtained for cNC using the Instrument limit. Furthermore, Kallumadil et al. tested 16 different commercially available coated IONP samples, and found them to have ILPs between 0.16 and 3.12 nHm^2/kg [73], while Unni et al. report an ILP of 6.1 nHm^2/kg, and refer to several values of between 0.17 and 5.9 nHm^2/kg reported in the literature [65]. Aslibeiki et al. reported ILPs of 0.45, 0.11, and 0.02 nHm^2/kg [68]. These reported or calculated values were below the highest ILPs obtained for both mNC and cNC. One can therefore conclude with a very successful heating of both of these samples, especially cNC.

Based on the experiments in this section, cNC had superior heating properties compared to the other samples across all the f and H combinations. Therefore, cNC was selected for further hyperthermia characterization. The optimal field and frequency combination of cNC was 102 kHz and 60 Oe for the Brezovich limit and 162 kHz and 190 Oe for the Instrument limit, based on the SAR values in Table 4.4. The AMF frequency of 162 kHz was chosen for the further studies due to its highest overall SAR value and its steady temperature increase for both corresponding field values.

Effect of Concentration

This section will explore how the concentration of cNC affected its heating properties, using an AMF with a frequency of 162 kHz. Concentrations lower than the previously studied 1 mg/mL were selected as cNC was incorporated into the NGs at low concentrations. As the concentration decreased, smaller temperature variations resulted in large differences in SAR. Therefore, studies with concentrations below 0.2 mg/mL were not conducted, as the experiments were considered unreliable.

Figure 4.7 shows the temperature of cNC for different concentrations, using both the Brezovich and the Instrument limit, indicated by solid and dashed lines, respectively. Table 4.6 shows the SAR values which were calculated from the initial slopes in Figure 4.7. The Instrument limit gave higher SAR than the Brezovich limit for all concentrations. There was no trend for the SAR as a function of concentration within either of the limits.

SAR was normalized by the IONP mass, which could indicate independence of particle concentration according to Equations 2.20, 2.21, and 2.22. However, various studies have shown SAR to either increase or decrease as a function of concentration. Deatsch et al. reviewed the effect of concentration on SAR in 11 different studies [69], and concluded that SAR generally decreased with increasing concentration for particles dominated by Néel relaxation. However, SAR could increase with increasing concentration for certain systems through increased hysteresis loss. Both effects were a consequence of thermally blocked particles due to magnetic interactions between the particles. The concentrations in the studies were generally far above what was used in this work, with the exception of the work by Piñeiro-Redondo et al., using concentrations of 0.6-20 mg/mL [75]. They found the SAR to increase with increasing concentration for coated particles, but decrease for uncoated particles. Since the concentrations that were used in this thesis were low, the interactions between the particles in the clusters were most likely significantly stronger than the interactions between the particles in separate clusters. This explains why SAR was independent of the concentration. The exception was the measurement at 0.2 mg/mL using the Brezovich limit, where the heat generated by the particles was too low to give a measurable temperature increase.

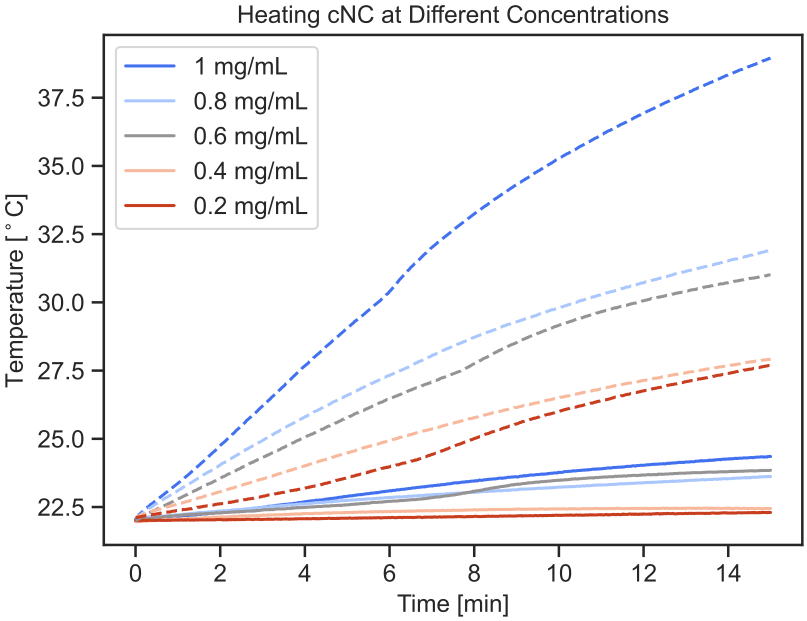

Figure 4.7: Temperature increase using different concentrations of cNC and an AMF at 162 kHz. The solid lines show measurements performed with field strengths following the Brezovich limit (38 Oe), while the dashed lines show measurements performed using field following the Instrument limit (190 Oe).

Table 4.6: SAR values for cNC at 162 kHz as a function of concentration. The field strength was 38 Oe for the Brezovich limit and 190 Oe for the Instrument limit.

c [mg/mL]	**Brezovich SAR [W/g]**	**Instrument SAR [W/g]**
1.0	43	484
0.8	53	411
0.6	57	444
0.4	47	391
0.2	0	416

The properties of the inorganic NPs used in this study in the relevance of optical and magnetic heating potential have now been discussed. AuER was incorporated into AuNG10, while cNC was selected to be incorporated into FeNG10 due to its superior colloidal and heating properties. Important characteristics of the resulting NGs are responsiveness to stimuli and preserved optical and magnetic properties of the incorporated AuNPs and IONPs, respectively. The effect of the inorganic NPs and NIPAM and AAc molar ratios on these properties will be presented in the following section.

4.2 Nanogel Properties

The synthesis of the NGs was performed as described in Section 3.2.3. As the reaction proceeded, the color turned from transparent to cloudy for all the samples, indicating a collapse of the NGs at the temperatures well above the LCST of NIPAM [30]. NG25 had a stronger cloudy color than NG10, while AuNG10 and FeNG10 had blue and brown shades, respectively, indicating the incorporation of NPs into the NG. However, it was discovered that some of the cNC particles were sticking to the magnetic stirrer during the FeNG10 synthesis, demonstrating that the incorporation was not perfect for this sample.

NGs were first attempted to be synthesized using an SDS and a KPS which were later discovered to be contaminated. For the experiments using a contaminated SDS, the monomers would not polymerize, which could be seen by the solution not turning white but remaining pale, and melting upon freeze-drying instead of forming a powder. For the experiments using a contaminated KPS, the particles seemed to polymerize based on the color of the solution, but the $\mathrm{VCE}_{\mathrm{temp}}$ was restricted to around 50 %. These observations underlined the importance of a surfactant and an initiator for the synthesis. The results from these unsuccessful experiments will not be included in the following sections.

4.2.1 Chemical Analysis and Morphology

As an initial analysis, FTIR and S(T)EM were used to characterize the chemical properties and the morphology of the samples, respectively. The results are not included in this section but in the appendix since they did not provide any relevant information.

The FTIR spectra for NG10, AuNG10, and FeNG10 are shown in Appendix A. All the NGs had similar spectra with peaks corresponding to C-N bending at 1100-1200 cm^{-1}, $-\mathrm{CH}_2$ stretching vibration at 1300-1400 cm^{-1}, C=O stretching at 1600-1700 cm^{-1}, $-\mathrm{COOH}$ stretching at 1700-1800 cm^{-1}, and N−H stretching at 3200-3300 cm^{-1} [82]. The similarity of the spectra was most likely due to the low amount of NPs incorporated into the hybrid NGs providing insufficient absorbance to influence the spectra.

The NGs were stained using PTA before being imaged using S(T)EM. The obtained micrographs are found in Appendix B.2. The NGs were not visible in the images, but the NPs could be seen in the images of the hybrid NGs, surrounded by a shadow, similar to what was observed in the literature [94]. The NGs were not visible because they mostly consisted of water and had low contrast in S(T)EM even after being stained. Anything that could be seen during imaging was immediately burned away by the electron beam, and was not visible for lower acceleration voltages.

The FTIR and S(T)EM characterization did not provide any new information about the NGs, and will therefore not be further discussed. The stimuli-responsiveness of the NGs will now be presented, starting with the temperature responsiveness.

4.2.2 Temperature Responsiveness

To evaluate the temperature responsiveness of the NGs, the hydrodynamic diameter, polydispersity index, and zeta potential were characterized at 25 and 45 °C. The results are displayed in Figure 4.8. The averages and standard deviations were calculated based on three measurements performed by the instrument, as before. The temperature values were chosen to characterize the full collapse as the different NGs could have different collapse temperatures within this region, and to compare with existing literature [30, 90, 94]. The d_{hyd} at the two temperatures were used to calculate the volumetric collapse efficiencies of the NGs upon an increase in temperature, i.e., the $\mathrm{VCE_{temp}}$, using Equation 2.15. The averages and standard deviations were based on the calculated $\mathrm{VCE_{temp}}$ from the three d_{hyd} measurements.

All the NGs had a negative ζ at both temperatures. d_{hyd} and PDI decreased with increasing temperature, while ζ increased (i.e, became more negative). FeNG10 had the highest PDI at both temperatures, while NG25 had the highest d_{hyd}. There were no apparent correlations between PDI or ζ with d_{hyd}. $\mathrm{VCE_{temp}}$ was above 90 % for all the samples, where NG10 and FeNG10 had a higher $\mathrm{VCE_{temp}}$ than NG25 and AuNG10.

The change in all the measured parameters upon the temperature increase and the $\mathrm{VCE_{temp}}$ above 90 % indicated strong temperature responsiveness for all the samples. This responsiveness can be explained by the temperature-dependent solubility of NIPAM. At 25 °C, the NIPAM-based NGs were hydrophilic and swollen because of hydrogen bonds between the amide groups of NIPAM and the water surrounding the NGs [21]. When the temperature increased to 45 °C, there was an entropy-favored release of the bound water molecules, as predicted by Gibbs free energy, and the NGs collapsed [8]. This response was also visible, as the NGs went from being transparent to cloudy when the temperature increased.

NG25 had an increased d_{hyd} at both temperatures and a decreased $\mathrm{VCE_{temp}}$, compared to NG10. The increased d_{hyd} was a result of the increased mole% of AAc relative to the initiator and stabilizer. This results in more monomers being incorporated into each NG, leading to larger NGs, in agreement with what has been observed in the literature [21, 30]. The decrease in $\mathrm{VCE_{temp}}$ of NG25 could be explained by the higher mole% of AAc compared to NIPAM. The temperature-dependent collapse has been attributed to the temperature-dependent solubility of NIPAM. Since the measurements were performed at a pH above its $\mathrm{pK_A}$, AAc would be hydrophilic as a result of electrostatic interactions at both the measured temperatures, not contributing to the collapse [8]. Consequently, a lower mole% of the monomers will contribute to the collapse in NG25, resulting in a reduced VCE$_{\text{temp}}$. A similar observation has been reported in the literature, although with slightly lower VCE$_{\text{temp}}$ than in this work [30].

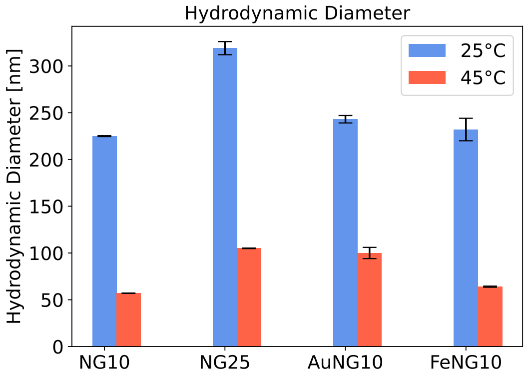

(a) Hydrodynamic diameter

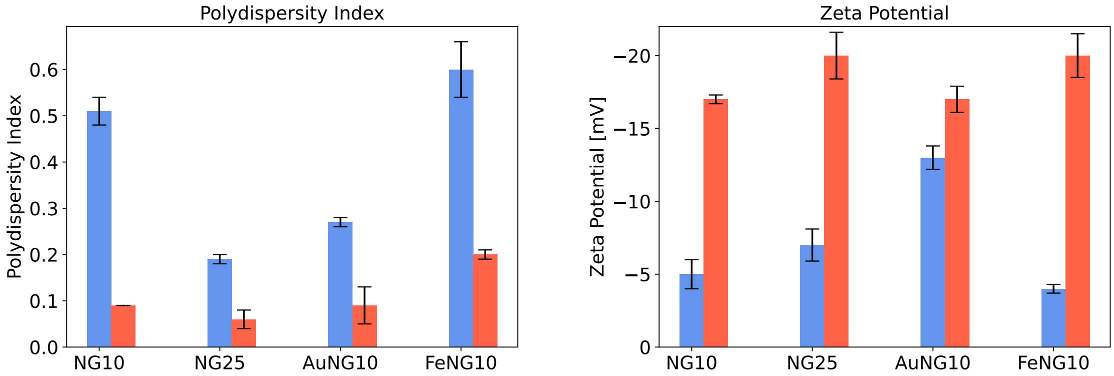

(b) Polydispersity index

(c) Zeta potential

Figure 4.8: The d_{hyd}, PDI, and ζ of the NGs at 25 and 45 °C, measured using the Zetasizer at pH 6. The bars show the averages and the error bars show the standard deviations based on three measurements per sample.

Table 4.7: VCE$_{\text{temp}}$ calculated using Equation 2.15 with d_{hyd} at 25 and 45 °C for all the NGs. The values were calculated based on three measurements per sample.

Sample	**VCE$_{\textbf{temp}}$** [%]
NG10	98.3 ± 0.5
NG25	92.5 ± 0.3
AuNG10	93.0 ± 1.3
FeNG10	97.9 ± 0.3

The slight increase in d_{hyd} for the hybrid NGs compared to NG10 has also been reported in the literature [94], and could be attributed to the incorporated NPs increasing the total volume of the NGs. However, this change may be considered insignificant in this work. The reduction of $\mathrm{VCE_{temp}}$ compared to NG10 was negligible for FeNG10, seen by the overlapping standard deviations, but high for AuNG10. A small decrease in $\mathrm{VCE_{temp}}$ of hybrid NGs could be explained by the NP volume being constant when the NGs collapsed, analogous to AAc remaining hydrophilic upon the temperature-driven collapse of NIPAM. The large difference between the $\mathrm{VCE_{temp}}$ of AuNG10 and FeNG10 could be explained by the reduced incorporation of NPs into FeNG10, or by differences in the properties of AuER and cNC, like morphology. In a previous study, the shape of AuNPs incorporated into NGs resulted in widely different $\mathrm{VCE_{temp}}$, where the etched rod morphology gave the lowest value, 84 %, while spheres gave significantly higher values [90]. However, the size, chemical composition, and surface functionalization of AuER and cNC were also different and could have contributed to the difference in properties of the resulting hybrid NGs.

An explanation for the decrease in PDI upon the increase in temperature could not be found in the literature. However, a possible explanation could be that variations between the NGs resulted in varying degrees of swelling at low temperatures. These differences would be reduced at higher temperatures, when the NGs collapsed and expelled the water. The PDIs at 25 °C were generally above the upper limit of 0.2 preferred for biomedical applications [85], with the exception of NG25. The reduced mole% of stabilizer and initiator in this sample would theoretically imply a lower monodispersity, oppositely of what was observed [83]. However, there was only a small difference between the PDI of NG25 and AuNG10, implying that this difference could alternatively be a result of batch-to-batch variations.

The ζ was below ± 30 mV for all samples, but due to the additional steric stabilization provided by SDS, they can still be assumed colloidally stable [85]. Additionally, ζ can only partly be used to characterize NGs since they have no well-defined slipping plane, and some of the charges can be buried [94]. The negative ζ of all the NGs can be attributed to the deprotonated carboxylic groups of AAc [30]. The increase in ζ upon the collapse could be explained by the conserved number of charges upon the decrease in size resulting in an increased electrophoretic mobility [8], and the negatively charged AAc coming more to the surface when the NIPAM underwent the coil-to-globule transition [30]. The increased ζ of NG25 compared to NG10 at both temperatures could be explained by the higher mole% of AAc in NG25, introducing more negatively charged carboxylic groups [30].

The VPTT describes the temperature at which most of the NGs undergo collapse. This parameter is based on the temperature-dependent swelling ratio, α, defined in Equation 3.1 [32]. By fitting α as a function of temperature to a sigmoidal curve, the VPTT was found at the inflection point [32]. Graphs illustrating α between 25 and 55 °C for the NG samples are shown in Appendix D.2. The VPTT was found for both heating and cooling, and the average was calculated from these. These values are tabulated in Table 4.8, where the averages and standard deviations were found from the three measurements performed per sample using the Zetasizer. The heating VPTT was lower than the cooling VPTT for NG10, but the opposite for NG25, AuNG10, and FeNG10. The VPTT was higher for NG10 than NG25, but higher for the hybrid NGs than NG10.

Table 4.8: The columns show the VPTT for the heating and cooling of the NGs, and the average of the two values. The VPTTs were found based on three measurements per sample, where the samples were heated up from 25 to 55 °C, and cooled back down. The intervals were of 5 °C. The measurements were performed at pH 6.

Sample	**Heating VPTT** [°C]	**Cooling VPTT** [°C]	**VPTT** [°C]
NG10	38.8 ± 1.6	39.1 ± 2.4	38.9 ± 1.7
NG25	37.2 ± 0.0	35.9 ± 0.1	36.5 ± 0.1
AuNG10	40.1 ± 0.4	40.3 ± 0.0	40.2 ± 0.2
FeNG10	40.1 ± 0.2	39.8 ± 0.6	40.0 ± 0.4

Differences in heating and cooling VPTT resulted from differences in the shape of the heating and cooling curves in Appendix D.2. However, from the figure in Appendix D.2, AuNG10 and FeNG10 had higher hysteresis. Both these observations could be explained by slow reorganization and the equilibrium state not being reached before the measurement [94], or by energy being required to break the hydrogen bonds between NIPAM and the surrounding water. Additionally, the hysteresis in the hybrid NGs could arise from different densities of NPs in the NGs introducing inhomogeneities to the system [94]. However, these differences between the heating and cooling curves were minor and unlikely to affect any following measurements.

All the NGs had finite polydispersities, leading to a collapse over a finite temperature range due to variations in chain lengths [30]. However, no further correlations were observed between the PDI of the NGs and the width of the collapse range.

All the VPTTs were above 32 °C, the LCST of NIPAM, as expected when copolymerizing NIPAM with AAc [8, 82]. In the literature, NGs similar to NG10 have been reported to have a VPTT around 37 °C [82, 94]. Since the hydrophilic nature of AAc promotes swelling, the VPTT reported in the literature has increased with increasing mole% AAc [21, 30]. However, this study observed the opposite when comparing NG10 to NG25. On the other hand, the increase in VPTT upon the incorporation of inorganic NPs was in agreement with what has been reported in the literature, attributed to an increase in hydrophilicity provided to the NGs [94]. As examples, a VPTT of 38.9 °C has been reported for Fe@Au NGs [94], while a VPTT around 39.5 °C was found for the AuNG10 sample in a previous study [90].

The VPTT of NGs for in vivo applications should fall within physiologically relevant and safe limits, i.e., between 37 and 45 °C [4]. This renders the VPTT of NG25 too low, as the NGs would collapse once injected into the body and before reaching the target site. The VPTT of NG10 could be considered suitable, but it is important to note the high standard deviation of this sample. Consequently, many of the NGs in NG10 would likely collapse at 37 °C. Therefore, AuNG10 and FeNG10 could be considered the samples with the most suitable VPTTs for the targeted drug delivery application. However, note that VPTT depends on the type of solvent, and the value could differ in vivo compared to in this measurement [8, 21].

4.2.3 pH Responsiveness

In the previous section, the temperature responsiveness of the NGs was evaluated, considering their collapse efficiencies upon an increase in temperature. This section will discuss the pH responsiveness using a similar approach, as responsiveness to low pH can be used to deliver cargo in a cancer environment or endosomal compartments, as explained in Section 2.4.1. The d_{hyd}, PDI, and ζ were measured at pH 6 and at pH 3. The results are displayed in Figure 4.9. The pH range was chosen to characterize the full collapse, similar as for the temperature. The blue bars are the same as in Figure 4.8. The volumetric collapse upon pH stimulus, i.e., $\mathrm{VCE_{pH}}$, was calculated using the measured d_{hyd}, and tabulated in Table 4.9. The averages and standard deviations were calculated as before.

The d_{hyd} and PDI decreased upon lowering the pH for all the samples. ζ was negative at both pH values, and decreased when the pH was lowered for NG10, NG25, and AuNG10, but remained unchanged for FeNG10. The $\mathrm{VCE_{pH}}$ was lower than $\mathrm{VCE_{temp}}$ for all samples, and varied widely between the samples, being largest for AuNG10 and lowest for FeNG10.

The change in d_{hyd} upon decreasing pH indicated pH responsiveness for all the samples. This can be explained by the pH dependency of AAc, having a pK_a of 4.3 [30]. Above this pH, the carboxylic groups of AAc are deprotonated, causing electrostatic repulsion between the groups, causing the monomer to spread out and become hydrophilic, making the NGs swell [8]. However, when the pH was decreased to 3, the carboxylic groups became protonated, and the hydrophilicity decreased, making the NGs collapse [21]. This response could also be observed in the change of color from transparent to turbid, as was also seen for the change in temperature. The lower $\mathrm{VCE_{pH}}$ compared to $\mathrm{VCE_{temp}}$ indicated a lower response to pH compared to temperature. This can be explained by the higher mole% of the temperature-responsive NIPAM than the pH-responsive AAc for all the NGs [30, 94].

Contrary to what has been reported in the literature, NG10 had a higher $\mathrm{VCE_{pH}}$ than NG25, despite the higher mole% of the pH-responsive AAc in NG25 [30]. However, the values obtained for the bare NGs in this work far exceed those reported in the literature, where a $\mathrm{VCE_{pH}}$ of 18 % has been found for a sample similar to NG10, and a $\mathrm{VCE_{pH}}$ of 23 % for NG25 [30]. The reasons for the negative $\mathrm{VCE_{pH}}$ trend when increasing mole% AAc, and the higher $\mathrm{VCE_{pH}}$ values compared with literature, are unknown.

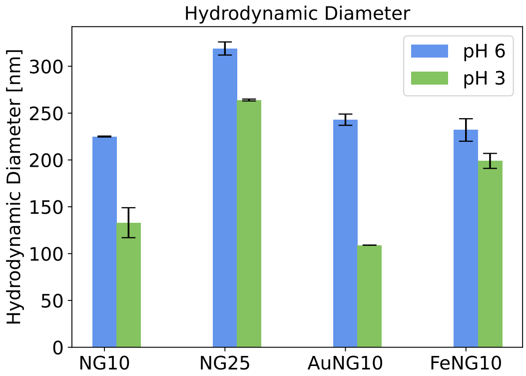

(a) Hydrodynamic diameter

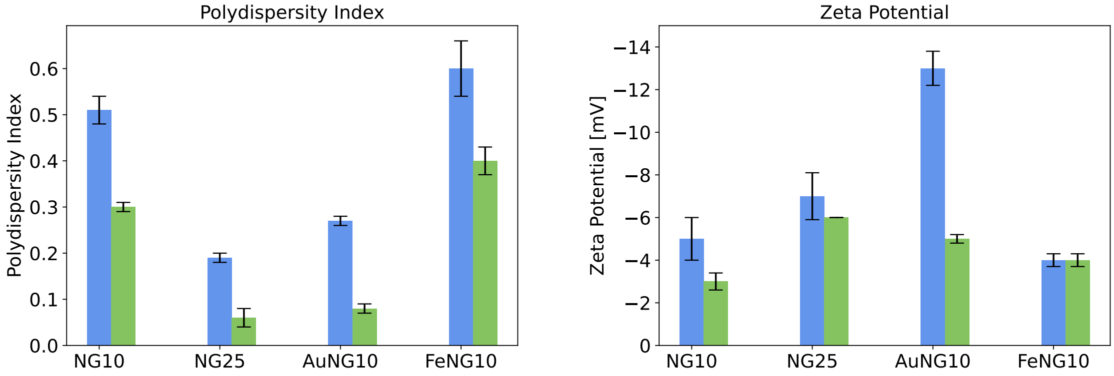

(b) Polydispersity index (c) Zeta potential

Figure 4.9: The d_{hyd}, PDI, and ζ of the NGs at pH 6 and pH 3, measured using the Zetasizer at 25 °C. The bars show the averages and the error bars show the standard deviations based on three measurements per sample.

Table 4.9: $\mathrm{VCE_{pH}}$ calculated using Equation 2.15 with d_{hyd} at pH 6 and pH 3. The values were calculated based on three measurements per sample.

Sample	$\mathbf{VCE_{pH}}$ [%]
NG10	80.8 ± 8.0
NG25	43.0 ± 3.4
AuNG10	90.8 ± 0.7
FeNG10	38.7 ± 7.5

The decrease in $\mathrm{VCE_{pH}}$ of FeNG10 compared to NG10 aligns with the reduced pH responsiveness reported by Yao et al. for dually responsive NGs incorporated with in situ synthesized IONPs, compared to NGs without IONPs [91]. Yao et al explained this observation by the bonds between the NPs and NGs preventing swelling and thus reducing the collapse, which does not seem applicable for this work since FeNG10 did not have a smaller d_{hyd} than NG10 in the swollen state. An alternative explanation could be the non-collapsing volume of the NPs reducing the VCE_{pH}, as suggested for the reduced VCE_{temp}. However, this effect would not sufficiently explain the entire difference observed in the VCE_{pH}. Furthermore, the VCE_{pH} of AuNG10 was larger than that of NG10. This increase could have been a result of interactions between the CTAB-coating in AuER and AAc. Lim et al. refer to numerous studies on pH-dependent interactions between CTAB and AAc [115], which could have influenced the VCE_{pH}. However, further investigation is necessary before a conclusion can be made to understand the interactions within this specific system where CTAB was bound to the AuNPs.

The PDI decreased both upon an increase in temperature and a decrease in pH. This could imply that reduced variations in swelling was a contributing factor, as earlier proposed. However, the lack of correlations between the extent of the collapse and the change in PDI between the different samples could weaken this hypothesis.

With the exception of FeNG10, the ζ was reduced when the NGs collapsed in response to the decrease in pH. This was the opposite of what was observed for the collapse due to an increase in temperature, where ζ increased. When the pH was reduced, AAc deprotonated and became neutral, leading to a decrease in the charges per NG and resultingly in a reduced ζ. However, as seen from the negative ζ, the AAc was not fully deprotonated at pH 3. Consequently, the decrease in d_{hyd} would lead to an increasing ζ, as earlier explained, opposing the reduction of ζ due to protonation. The change in ζ was small for NG25, which had the second lowest VCE_{pH}, and ζ did not change for FeNG10, which had the lowest VCE_{pH}. This can be explained by a reduced AAc protonation in these NGs. The difference in ζ was very large for AuNG10, which was hypothesized to have an increased protonation of AAc due to the interactions with CTAB, based on the work reported by Lim et al. [115]. These observations align with the pH-induced collapse mechanism being the AAc protonation.

The responsiveness of the NGs to changes in temperature and pH has now been established through experimental observations. It is also interesting to explore how the NGs respond to both pH and temperature simultaneously, as this dual responsiveness is particularly relevant for targeted drug delivery applications.

4.2.4 Dual Responsiveness

Responsiveness to both an increase in temperature and a decrease in pH could enable the NGs to respond to both externally controlled heat generation and cancer environments. Therefore, the response to this dual stimuli was characterized. Firstly, the pH was lowered by dispersing the freeze-dried NGs into MQ water with pH 3, then the temperature was increased using the Zetasizer. d_{hyd}, PDI, and ζ were measured under these conditions, and compared to the values without any stimuli. The results are shown in Figure 4.10, where the blue bars are the same as before. VCE_{dual} is found in Table 4.10, calculated using d_{hyd}.

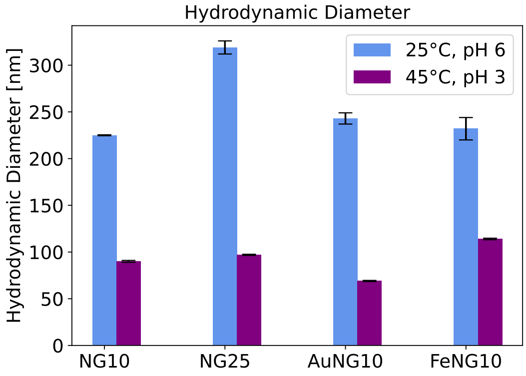

(a) Hydrodynamic diameter

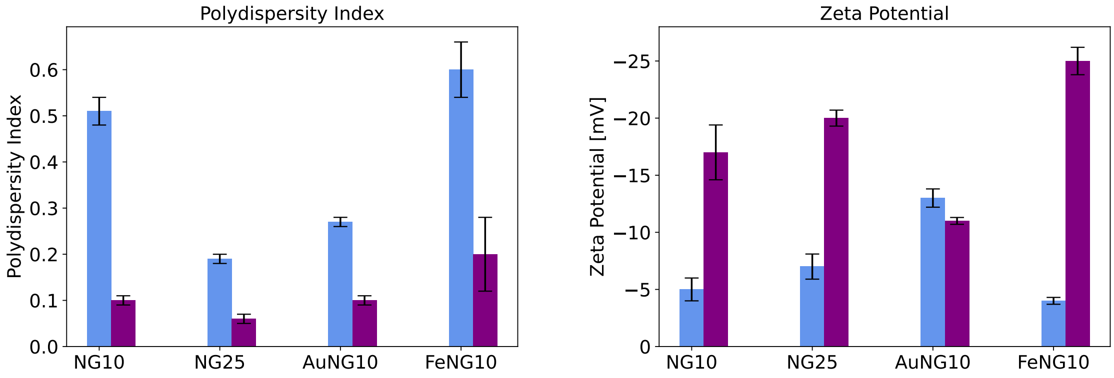

(b) Polydispersity index

(c) Zeta potential

Figure 4.10: The d_{hyd}, PDI, and ζ of the NGs at 25 °C with pH 6 and 45 °C with pH 3, measured using the Zetasizer. The pH stimulus was introduced first, and then the temperature stimulus. The bars show the averages and the error bars show the standard deviations based on three measurements per sample.

Table 4.10: Dual VCE obtained by lowering the pH from 6 to 3 and then increasing the temperature from 25 to 45 °C.

Sample	$\mathbf{VCE_{dual}}$ [%]
NG10	94.4 ± 0.5
NG25	97.2 ± 0.2
AuNG10	98.1 ± 0.2
FeNG10	88.6 ± 0.7

The d_{hyd} and PDI decreased for all samples upon the dual stimuli, while ζ increased for all samples apart from AuNG10. The decrease in PDI was similar to before, and a possible explanation for this has already been proposed. VCE_{dual} was larger than VCE_{pH} for all samples, but smaller than VCE_{temp} for all samples except NG25. VCE_{dual} was largest for AuNG10, and smallest for FeNG10.

As discussed in the previous sections, the mechanisms for collapse induced by pH and temperature were different. Therefore, the order of the applied stimuli was important. In this work, the pH was changed first to simulate the NGs entering an environment with low pH. Thereafter, the temperature was increased to mimic external stimuli through either optical or magnetic heating. This sequential order of stimuli would be more realistic for the targeted drug delivery application than the opposite order would be. If the temperature were increased first, the temperature-induced collapse would lead to more AAc being present on the NG surfaces when the pH was subsequently decreased [30], which would impact the measured properties. When analyzing the results presented in Figure 4.10, it could be useful to consider them in relation to the green bars in Figure 4.9. The resulting difference between the green and purple bars would represent the influence of the increase in temperature at pH 3, which differed from the effect of the temperature increase at pH 6, which was illustrated in Figure 4.8.

The change in all parameters upon the dual stimuli along with the high VCE_{dual} indicated a dual responsiveness of all the NGs. The responsiveness was initially due to the protonation of AAc upon lowering the pH, most likely followed by the coil-to-globule transition of the NIPAM. The measured parameters under the dual stimuli were more similar to those obtained by the temperature increase alone than to those obtained by the decrease in pH alone. This can be explained by NIPAM being the monomer present with the highest mole% in the NGs.

The VCE_{dual} exceeded 90 % for all samples apart from FeNG10. The low VCE_{dual} of FeNG10 could be a result of its poor pH-responsiveness, with a VCE_{pH} of only 38.7 %, being lowest among all the samples. In contrast, AuNG10 exhibited the highest VCE_{dual} of the samples, and additionally had a high response to both temperature and pH when the stimuli were applied individually. However, NG25 had a lower response to both pH and temperature compared to NG10, but had a higher VCE_{dual}. This indicates that the individual VCE values did not perfectly reflect the dual response of the NGs.

NG10 and FeNG10 exhibited higher VCE_{temp} than VCE_{dual}. Since both the temperature and the pH-induced a collapse when they were changed individually, this suggests that the effect of the increased temperature could differ at pH 3 compared to at pH 6. One possible effect was that the deprotonation of AAc could be enhanced with increasing temperature, counteracting the collapse caused by NIPAM and resulting in a reduced dual collapse [30]. Moreover, there has even been reported to be an increase in d_{hyd} upon dual stimuli compared to without stimuli [94]. These findings highlight the need for further investigation of the properties of the NGs under dual stimuli to better understand their behavior at this physiologically relevant combination of stimuli.

The ζ for all the samples was initially changed as shown in Figure 4.9c where the pH was reduced, simultaneously decreasing by protonation of AAc and increasing because of the reduction of size. Subsequently, the ζ could be expected to increase when the temperature was increased due to the AAc that remained deprotonated moving to the surface and the number of charges being constant while the size decreased, as shown in Figure 4.8. However, this last assumption might no longer hold, as the protonation of AAc could change when the temperature changed [30]. This variation in protonation could explain why the ζ values ended up as high or higher than those obtained solely from an increase in temperature for three out of the four samples, even though the AAc had been protonated before the temperature increase.

The ζ increased for all samples except AuNG10 upon dual stimuli, and obtained the same value as for only temperature stimulus for both NG10 and NG25. FeNG10 obtained an even higher value for dual stimuli than temperature stimulus. All these observations could be explained by the change in ζ for the different samples upon the decrease in pH, seen in Figure 4.9c. The ζ of AuNG10 decreased significantly, preventing the temperature stimulus from increasing back up to its initial level. For NG10 and NG25, the decrease was small and seemingly irrelevant for the subsequent increase in ζ upon temperature stimulus. And for FeNG10, there was no change in ζ for only temperature stimulus, giving a higher final upon the subsequent temperature increase.

The responsiveness of the NGs to temperature, pH, and both temperature and pH has been established, by demonstrating a change in d_{hyd}. This effect could potentially be used to release a loaded drug from the NGs. The following sections will look into the optical properties of AuNG10 and the magnetic and heating properties of FeNG10. The aim is to study how the properties of the inorganic NPs incorporated into the NGs were preserved, and explore how these properties could be used to externally induce the collapse of these hybrid NGs.

4.2.5 Optical Properties

UV-vis was used to verify the preservation of the optical properties of AuER upon incorporation into AuNG10. The absorbance of NG10 was measured as a reference to normalize the absorbance of AuNG10. The absorbance spectra are presented in Figure 4.11. The spectrum for AuER is the same as was illustrated in Figure 4.3, but the absorbance is adjusted to become comparable with that of AuNG10, which had much lower absorbance values. The highest peak of AuER at 748 nm was still found in AuNG10, but with a small bathochromic shift to 757 nm. The second-highest peak of AuER at 518 nm was also still visible, while the peak from 597 nm was barely visible. The absorbance of NG10 was low, but increased at decreasing wavelengths and had a small peak at around 618 nm.

The LSPR properties depend on the chemical environment around the NPs [26], and

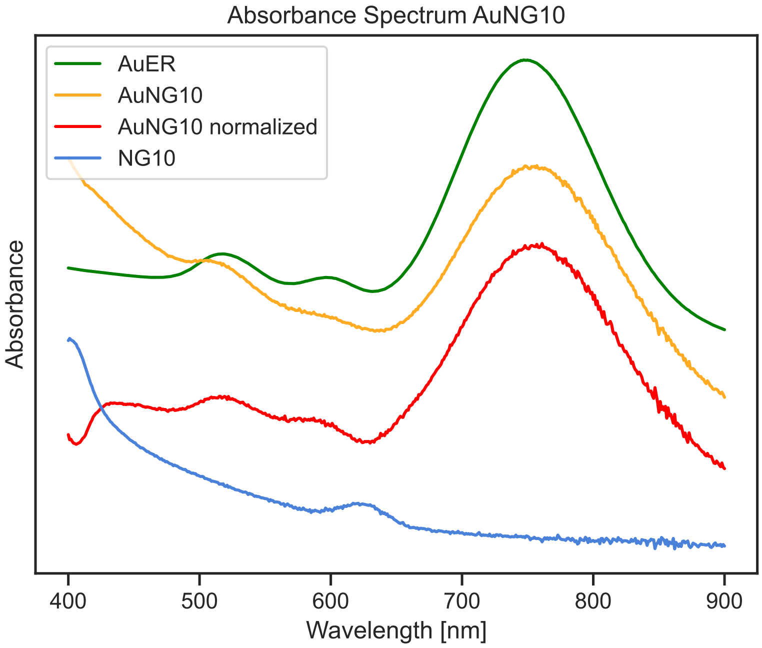

Figure 4.11: Absorbance spectra for AuER, NG10, AuNG10, and AuNG10 normalized with NG10, characterized using UV-vis.

the bathochromic shift of the highest peak has previously been reported for coated AuNPs, explained by an increase in the hydrophilic environment around the NPs [95]. The smaller peaks were less visible when normalizing with NG10, resulting from the increased absorbance of NG10 at lower wavelengths. The increased absorbance of NG10 at lower wavelengths was due to light scattering from the bare NGs [43].

The preserved highest peak of AuER upon incorporation into the NGs indicates that AuNG10 could be possible to track and image for biomedical applications [21]. Additionally, since the peak was within the NIR region of the EM spectrum, AuNG10 showed promise for generating heat in response to irradiation through the photothermal effect when injected into the body [4]. The next section will present the magnetic properties of FeNG10, in context with magnetic heating of the cNC particles incorporated into the sample.

4.2.6 Magnetic Properties

Freeze-dried FeNG10 was characterized using VSM with the same field as was used for the IONPs to understand the magnetic properties of the cNCs when incorporated into the NG matrix. NG10 was also attempted to be characterized in order to detect any magnetic contributions due to the bare NGs or the sample holder, but the magnetic properties were too weak to be measured in the set-up. Only one measurement was performed for FeNG10, compared to three measurements performed for each of the

IONP samples. This gives a larger uncertainty for the FeNG10 measurement.

For comparison, the magnetization curve for FeNG10 and cNC are both shown together in Figure 4.12. The magnetization curves for the two samples had similar shapes. FeNG10 had a M_S of 91 memu/g, a M_R of 10 memu/g, and a H_C of 21 Oe, giving a M_R/M_S ratio was 11 %, while the values for cNC were provided in Table 4.2.

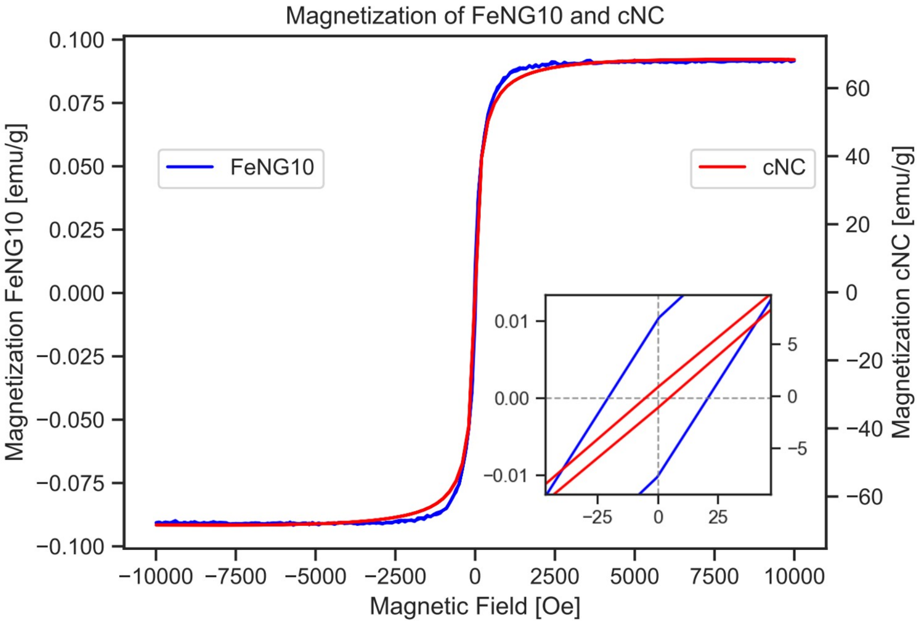

Figure 4.12: Magnetization of FeNG10 in response to a magnetic field, compared with the magnetization of cNC. The y-axis on the left shows magnetization values for FeNG10, while the y-axis on the right shows magnetization values for cNC. FeNG10 had a M_S of 91 memu/g, a M_R of 10 memu/g, a H_C of 21 Oe, and a M_R/M_S ratio of 11 %. The values for cNC were presented in Table 4.2. The inserted figure shows a closer look at the hysteresis, around zero field.

The observed similarity of the curves has also been reported upon incorporating IONPs into NGs in the literature, indicating the SPM properties were preserved [91]. FeNG10 had a slightly steeper curve and a significantly higher hysteresis than cNC. To illustrate this, the FeNG10 had a M_R/M_S ratio more than six times higher and a H_C more than four times higher than cNC. These high values could be an error due to the low magnetization values, giving inaccurate measurements for low field strengths. The magnetization values were close to the lower limits provided by the instrument due to the resolution, according to instrument specifications [112]. This could also explain the increased noise of the FeNG10 curve compared to the smoother cNC curve. Another explanation for the large hysteresis could be that there were a much larger number of thermally blocked particles in FeNG10 than for cNC, but this is unlikely due to the lower concentration of particles.

The wt% of cNC in FeNG10 was around 0.45, assuming all the particles were incorporated during the synthesis. However, assuming the M_S of the cNC particles would be conserved upon the incorporation, the wt% of the cNC in the NGs would be 0.13, according to the M_S of cNC compared to that of FeNG10. This entails that either less than one-third of the cNC particles were incorporated into FeNG10, or the cNC particles had reduced M_S when incorporated into the NGs, or a combination of the two effects. During the FeNG10 synthesis, it was observed that not all the particles were incorporated. This was most likely due to the high magnetization of the particles, and could be improved using a mechanical stirrer instead of a magnetic one. Additionally, it has been shown that surface coating can lower the M_S of IONPs by shielding the magnetic particles from the applied field [58]. This effect could be even more significant when the particles were incorporated into the NGs. To conclude, the reduced M_S of FeNG10 compared to cNC was most likely a combination of poor incorporation and high shielding of the NG. Since FeNG10 exhibited SPM-like magnetic properties, the heating efficiency of the sample was studied.

4.2.7 Heating Efficiency

The NGs were all found to be temperature-responsive, exhibiting high collapse efficiencies upon reaching 45 °C. The VPTT of FeNG10 was 40 °C. In order to reach this temperature, the heating efficiencies of the NGs must be sufficient. Therefore, the heating properties of 1 mg/mL FeNG10 were studied using the magneTherm.

Figure 4.13 shows the temperature recorded in FeNG10 when subjected to an AMF with a frequency of 162 kHz, and a field corresponding to the Brezovich and the Instrument limit. The temperature increase was 0.65 °C for the former limit and 2.82 °C for the latter. Using the weight of the whole NG sample as the mass, the SAR was 27 W/g for the Brezovich limit, and 85 W/g for the Instrument limit. Using only the weight of the cNC incorporated into the NG, assuming perfect incorporation (wt% of 0.45) and that the particles were perfectly distributed in the NG, the SAR would be 5918 W/g for the Brezovich limit and 18986 W/g for the Instrument limit. Considering the non-perfect incorporation, the values would be even higher. The SAR and temperature increase were higher for the Instrument limit than the Brezovich limit, as was observed for the IONPs.

The SAR values calculated based on the cNC content should be used with care due to the small masses, since small temperature changes gave very high SAR values. Additionally, there was uncertainty regarding the mass of cNC particles in the sample due to the non-perfect incorporation. Therefore, these values were associated with large uncertainty, and should not be compared directly with other values. Based on the concentration studies in Section 4.1.5, the SAR of FeNG10 would be expected to be the same as for the pure cNC sample, or lower due to possible shielding effects. However, there could also be effects of the incorporation into the NGs, which could affect the heat generation, for example by changing the relaxation times. Either way, the extremely high SAR values calculated here could be considered an error, and the temperature increases would be more interesting to discuss.

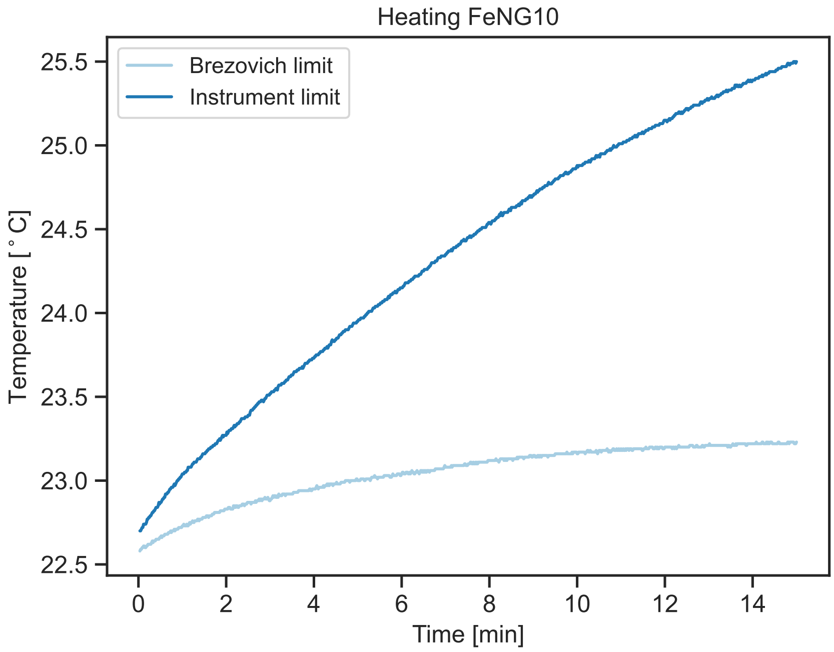

Figure 4.13: Temperature increase of FeNG10 upon exposure to an AMF at 162 kHz and 38 Oe (Brezovich limit) and 190 Oe (Instrument limit). The figure should be seen with respect to the heating of water under the same field strengths, shown in Figure 4.5.

The temperature increase was reduced for FeNG10 compared to cNC as a result of the lower concentration of heating IONPs. However, considering the low concentration of cNC in FeNG10, the heating was very high. Assuming an initial temperature of 37 °C, the final temperature would be around 39.8 °C using the instrument limit. This was close to the VPTT of FeNG10 and would result in a partial collapse of the NGs. Furthermore, the temperature was still increasing after the initial 15 min and could have reached higher temperatures if the measurement had continued. Additionally, the rotational motion of the cNC particles could potentially accelerate the NG collapse through mechanical disruption, as has been reported in the literature [98]. The temperature increase was far below the 45 °C limit for not damaging healthy cells [80].

The properties of the NGs have now been characterized and discussed with respect to their performance as a targeted drug delivery system. The next section will be a study of their performance in loading a hydrophilic and a hydrophobic drug, which was released in the final section of this work.

4.3 Drug Loading

The NIPAM-AAc NGs contain hydrophilic and hydrophobic branches, which allow for loading with the hydrophilic and hydrophobic model drugs Cyt C and SA, respectively. This comparison was performed to investigate the loading mechanisms of the NGs, which will be discussed in the following chapters. Initial studies were performed to optimize the drug loading process. These include obtaining calibration curves, performing kinetic studies of the drug loading, and optimizing the drug loading process for each of the two model drugs.

4.3.1 Preliminary Studies for Drug Loading

The drug absorbance and concentration calibration curves were obtained to evaluate the drug loading, as described in detail in Section 3.3. The absorbance spectra for SA and Cyt C at different concentrations are found in Figures 4.14a and 4.15a, obtained using UV-Vis. The absorbance peaks at 296 nm for SA and 409 nm for Cyt C were marked by vertical gray lines, and the absorbance values at these peaks were plotted against their corresponding concentrations in Figures 4.14b and 4.15b. The calibration curves were obtained using the linear relationship between A and c from Beer-Lambert's law, defined in Equation 2.26, to perform a linear regression. The resulting lines had slopes of 25.69 for SA and 8.04 for Cyt C, where the R^2-values for this linear fit were 0.99 for both drugs.

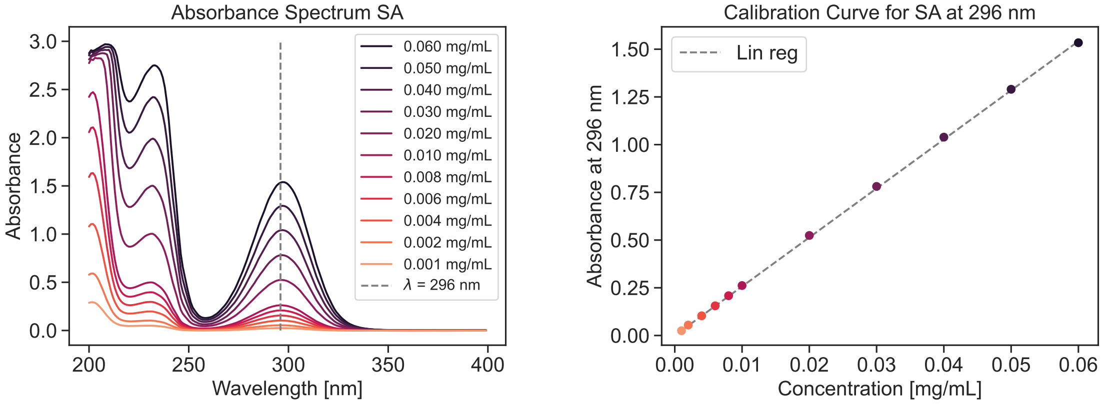

(a) Absorbance SA

(b) Calibration curve SA

Figure 4.14: Figure (a) shows absorbance measurements for different concentrations of SA, and (b) shows the calibration curve obtained for the measurements at 296 nm. The line had a slope of 25.69 with an R^2 of 0.99.

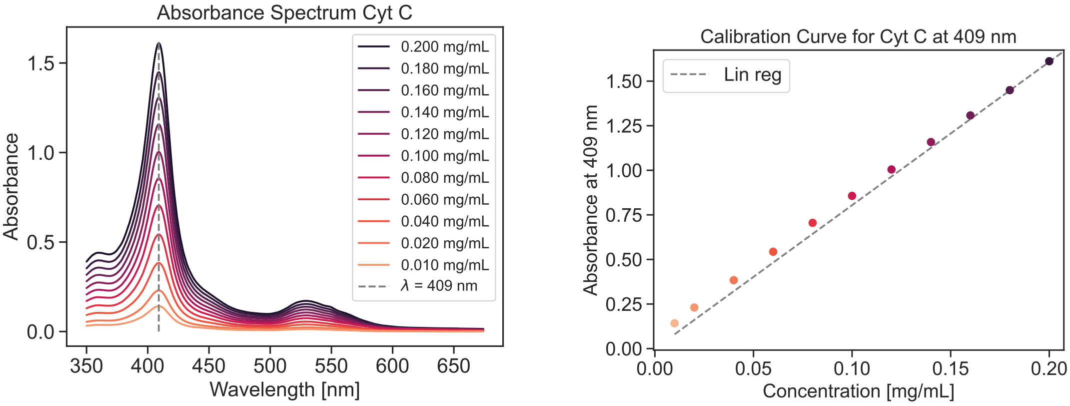

(a) Absorbance Cyt C (b) Calibration curve Cyt C

Figure 4.15: Figure (a) shows absorbance measurements for different concentrations of Cyt C, and (b) shows the calibration curve obtained for the measurements at 409 nm. The line had a slope of 8.04 with an R^2 of 0.99.

The R^2-values were high for both drugs, indicating good fits for the linear regressions. As a result, the obtained calibration curves could be used to characterize the drug loading. The linear relationship between A and c generally holds for A below 1, but was observed up to an A of 1.6 for both SA and Cyt C. Above this value, the absorbance increased less than the concentration, and this data was not included in the calibration curves.

Kinetic studies of the absorbance during the drug loading were performed in order to verify that the absorbance of the loaded drug was the same as for the unloaded drug. 0.85 mg/mL of freeze-dried NG10 was dispersed into either 0.04 mg/mL of SA or 0.1 mg/mL of Cyt C, and the solution was stirred for 3 hours at 400 rpm in the UV-Vis, while the absorbance was measured every 30 seconds. The drug concentrations were chosen to be within the range of the calibration curves, due to the linearity between A and c in this region. The results from this study are shown in Appendix F.1. For SA, there was no shift in wavelength over time, but a small increase in absorbance, which was presumably due to the poor solubility of SA in water, taking time to dissolve completely. For Cyt C, there was no significant change in the absorbance peak. To conclude, the absorbance of the free drugs was approximately the same as the loaded drugs, confirming that the drug loading and release could be characterized by measuring the absorbance of the NGs loaded with the drug.

Section 3.4 describes the drug-loading process. The process was optimized by shaking the freeze-dried NG with a drug concentration of 0.5, 0.75, 1, or 1.5 mg/mL at 300 rpm for 2, 4, 6, 8, 24, or 48 hours. Higher concentrations were also attempted, but discarded due to the poor solubility of SA in water [14]. Furthermore, separation was attempted by dialysis and by centrifugation. For centrifugation separation, the absorbance of the supernatant was measured. For dialysis, the absorbance of the drug-loaded NGs was measured, and normalized by the absorbance of the unloaded NGs at the same concentration. The optimal combination was found to be using 1.5 mg/mL for SA, as the drug was poorly loaded at lower concentrations. 0.5 mg/mL Cyt C was used since the drug was more easily loaded, and to make it comparable with existing literature [30, 94]. The optimal loading time was 2 hours, and separating the loaded drug from the unloaded drug was optimized by centrifugation for 30 min. Therefore, these combinations were used for the drug loading experiments.

4.3.2 Drug Loading with Hydrophobic and Hydrophilic Drug

The drug loading was performed as described, and characterized by measuring the absorbance of the supernatant at 296 or 409 nm, the wavelength of maximum absorbance for the model drugs, after the centrifugation. The LE and EE were calculated from this value, using Equations 2.24 and 2.25, respectively.

All samples were loaded five times with Cyt C and nine times with SA, with the exception of FeNG10, which was loaded 21 times with SA. The complete collection of these drug loading results is shown in Appendix F.2, together with which release experiment the sample was subsequently used in. For the hybrid NGs, a possible inhomogeneous distribution of NPs in the NGs could lead to differences in the drug loading properties from measurement to measurement. For NG10 and NG25, on the other hand, the LE and EE should theoretically be similar for all measurements. However, this was not the case, which could be a result of insufficient centrifugation or inaccurate removal of the supernatant. Due to the differences in measurement populations between the samples and the fact that the variance in LE and EE was assumed to be an error, the average and standard deviations were not calculated, and the highest obtained LE and EE for each sample will be discussed instead.

Table 4.11 shows the drug loading results obtained for the different NGs with the two drugs. The EE was higher using SA than Cyt C for all samples. The LE was higher using SA for AuNG10 and FeNG10, but higher using Cyt C for NG10 and NG25. AuNG10 had the highest LE and EE using SA, while NG25 had the highest LE and NG10 had the highest EE using Cyt C.

The trend for increased EE using SA and increased LE using Cyt C is a result of the differences in drug concentration used for the loading, as seen from Equations 2.24 and 2.25. This makes comparing the LE and EE of SA and Cyt C challenging since SA will generally give decreased LE and increased EE compared to Cyt C due to the increased drug concentration used. The variances between trends for LE and EE when comparing samples loaded with the same drug were a result of small differences in the measured weight of the NGs.

When loading with Cyt C, NG25 had a higher LE and similar EE compared to NG10. Using Cyt C and corresponding NGs, Sharma et al. obtained lower loading for NG10 and similar loading for NG25 compared to this work [30]. Furthermore, a higher loading of NG25 compared to NG10 was reported, as partly found in this work. Two

Table 4.11: Drug loading results from the different NGs using different drugs. The drug concentration when loading was 1.5 mg/mL for SA and 0.5 mg/mL for Cyt C. LE and EE were calculated using Equations 2.24 and 2.25. The highest LE and EE per sample are tabulated, while all data are shown in Appendix F.2.

Sample	**Drug**	**LE [%]**	**EE [mg/mg]**
NG10	SA	27.5	0.41
NG25	SA	50.6	0.84
AuNG10	SA	65.2	0.98
FeNG10	SA	60.3	0.95
NG10	Cyt C	64.4	0.38
NG25	Cyt C	67.2	0.37
AuNG10	Cyt C	37.7	0.20
FeNG10	Cyt C	56.8	0.28

explanations were proposed. Firstly, NG25 incorporated a higher amount of monomers into each NG, confirmed by the increased d_{hyd}. NGs are assumed to mainly load drugs through physical encapsulations into the pores of the matrix when using a breathing-in method [21, 94]. Consequently, the larger volume of NG25 provided more pores and space for drug loading [30]. Note that the NG mass used to load each sample was approximately the same, meaning the fewer but larger NGs in NG25 had a higher loading capacity due to the decreased surface-to-volume ratio. Secondly, the loading efficiency of NGs using a breathing-in method can depend on interactions between the NGs and the drug [96]. Drugs with opposite charges of the NGs would be more easily loaded [8], resulting in an enhanced loading of the weakly positive Cyt C at pH 6 [94] due to the negative charge of the carboxylic groups of AAc at this pH, leading to the formation of a polymer-protein complex [94, 95]. Consequently, the higher amount of AAc in NG25 could further increase the loading of Cyt C [30].

The higher loading of SA in NG25 compared to NG10 could be due to the larger volume of the NGs in NG25, providing more pores for encapsulation. Additionally, SA is a small drug, having a molecular weight of 138 Da compared to the 12 kDa of Cyt C, which could lead to a higher encapsulation. Additionally, hydrophobic polymer networks easier encapsulate hydrophobic drugs [8], and NIPAM has both hydrophilic and hydrophobic domains. For cellulose NGs, SA has been shown to interact with the hydrophobic branches of the NGs, but also to have van der Waals interactions with the hydrophilic branches [13], which could be proposed loading mechanisms for the NGs in this work as well. The negative charge of SA at pH 6 [14] would imply electrostatic repulsion with AAc, which could have led to a decrease in loading for NG25 due to more AAc monomers, but this was not observed.

The reduced loading of Cyt C for the hybrid NGs was in agreement with what has been reported in the literature, explained by the NPs occupying space and reducing available binding sites [94]. The much lower loading of AuNG10 compared to FeNG10 could be due to the higher incorporation of the AuER than cNC particles, supported by the observed poor incorporation of cNC during the FeNG10 synthesis. Furthermore, the shape or functionalization of the particles could contribute to a difference in blocking of the binding sites from Cyt C.

The increased loading of SA for the hybrid NGs, compared to the loading of SA for the bare NGs and Cyt C for the hybrid NGs, could indicate positive interactions between the drug and the inorganic NPs in the samples. The negative charge of SA would experience electrostatic attraction from the positively charged AuER and cNC particles. The increased loading into AuNG10 compared to FeNG10 could be due to the higher incorporation of AuER particles, giving a stronger electrostatic attraction, or additional hydrophobic interactions between SA and the CTAB tail. Furthermore, the small size of SA compared to Cyt C could lead to the SA not being blocked by the inorganic particles.

As a final note, it has been found that drug-loaded NGs had a similar size and shape as unloaded NGs, meaning the characterized NG properties should still apply for the loaded drugs [103]. The final section of this work will discuss the drug release from these NGs.

4.4 Drug Release Studies

The drug release studies are divided into those performed using the nanoTherics magneTherm to continuously monitor the absorbance in the release medium, and those performed by manually measuring the absorbance of the sample inside a cellulose membrane every 30 min. The differences between the two measurement techniques were illustrated in Figures 3.4a and 3.4b. The corresponding results will now be presented.

4.4.1 magneTherm Release Studies

The drug release using the magneTherm was performed as described in Section 3.5.1, using SA as the model drug. The combination of real-time monitoring of the absorbance of the release medium and the application of an AMF allowed for studying the effect of magnetic heating on the drug delivery system. The set-up consisted of the magneTherm instrument, power generator, function generator, water cooler, UV-vis spectrophotometer, and release medium pump. The membrane containing the sample was placed inside the release medium, located inside the center of the coil generating the AMF. A pump continuously circulated the release medium between the surroundings of the membrane and the UV-Vis spectrophotometer. Preliminary experiments were performed to optimize the protocol for the release experiments.

Preliminary Studies for the magneTherm Release Studies

A second calibration curve was obtained for SA with the UV-vis used for the magneTherm release studies and is found in Appendix F.3. The slope was 24.28, and the

R^2-value was 0.99, indicating a good fit. Note that the slope was slightly lower than the calibration curve obtained for the drug loading.

A kinetic study of the absorbance of SA at 45 °C and pH 3 was performed to ensure that the same calibration curve could be used for these conditions. The results are found in Appendix F.4 and show no apparent shift in the wavelength of the peak over time. However, the peak was shifted from 296 to 299 nm for the whole study, which might induce a small error in the results, making the calculated release lower than it was. There was also a slight increase in the absorbance over time, which can be explained by SA taking time to dissolve completely, as before.

Experiments using unloaded SA were performed to study the delay of the measured release in the setup. Figure 4.16a shows the release of 2 mL 0.5 mg/mL of SA placed into the water bath, outside the dialysis membrane to simulate the delay from the drug being released from the membrane until detected in the UV-vis. 100 % release was detected after approximately 3 min. Figure 4.16b shows the release of 2 mL of 0.5 mg/mL of SA from inside the membrane to simulate the delay from the drug being released from the NGs until it was detected. 100 % release was detected after around 3 hours at pH 6, but only 60 % of the drug was detected at pH 3 after the same time. Studies with Cyt C were also conducted, but no release was detected.

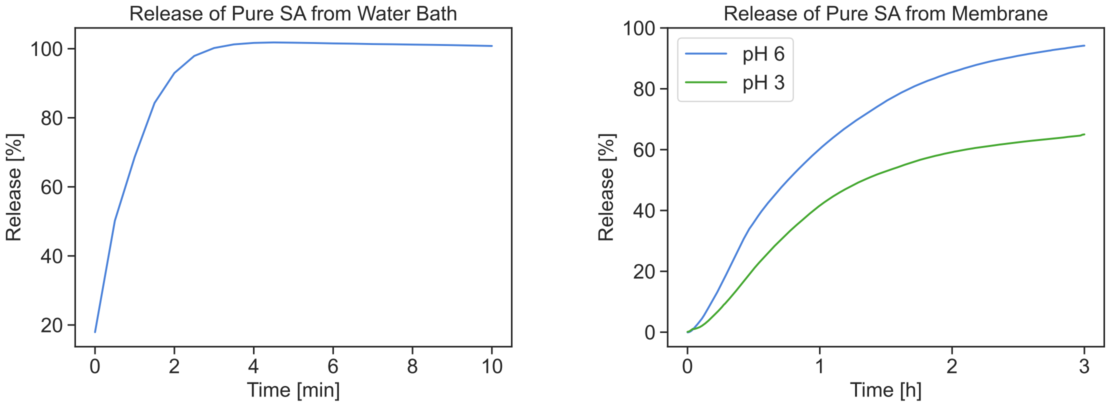

(a) SA in water bath

(b) SA in dialysis membrane

Figure 4.16: Release of pure SA in the magneTherm in a medium with pH 6. Figure (a) shows the release profile of SA from the release medium and to the detector. Figure (b) shows the release profile of SA from inside the dialysis membrane to the detector, both for pH 6 and pH 3. Both studies were performed at 25 °C.

The 3 min delay from the water bath to the detector in Figure 4.16a was deemed to be negligible compared to the length of the experiments. The release seemingly starting at 20 % was a consequence of the UV-vis characterizing the average absorbance over 30 seconds at the time, meaning the average absorbance during the first 30 seconds was around 20 %.

The three-hour delay from the membrane to the detector at pH 6 in Figure 4.16b will induce a significant delay in the release studies, and indicates that the drug was stuck inside or onto the membrane despite the higher MWCO of the membrane than the molecular weight of SA. Furthermore, the delay was even bigger at pH 3. The reason for this large difference due to pH is not known, but the minor shift of the absorbance peak of SA at pH 3 and the additional proton acquired by SA at this pH [14] could give small contributions, but not explain the entire difference. As the preliminary studies have been presented, the following section will contain the results from the drug release experiments performed using the NGs loaded with SA.

Release from Nanogels Loaded with Salicylic Acid

Pulsed release studies were performed for FeNG10 under the application of an AMF with a frequency of 162 kHz, as optimized in Section 4.1.5, and field strengths corresponding to the Brezovich and Instrument limit. The experiments were performed for 4 hours, using mediums at 25 and 37 °C in combination with pH 6 and 3. The AMF was applied in pulses of 20 min with 10 min between. Additionally, static release experiments were performed for 3 hours for all the NG samples, using mediums at 25 and 45 °C, combined with pH 6 and 3. For the dual stimuli, the pH was lowered first, then the temperature was increased, similarly to the $\mathrm{VCE}_{\mathrm{dual}}$ measurements. For FeNG10, two additional static release studies were performed at 37 °C with pH 6 and 3 to compare with the pulsed release studies at these conditions.

The pulsed release results are shown in Figure 4.17, while the static release results are shown in Figure 4.18. Additional pulsed release studies using a double concentration of FeNG10 were performed, but these are found in Appendix F.5 due to the lack of additional information obtained from the studies. Static release experiments were performed using all the NG samples, but only the results from NG10 and FeNG10 are provided in Figure 4.18, due to the lack of additional information obtained from the studies of NG25 and AuNG10. The release from NG25 and AuNG10 is shown in Appendix F.5. NG10 was selected to keep in this section to discuss the effect of the different mediums on the release, while FeNG10 was kept in this section to compare the pulsed release experiments performed on this sample to the ones with static release medium. Appendix F.2 shows the drug loading for the samples used in the release, in addition to the R^2 obtained for fitting the release profile to zero-order release.

The small peak at 37 °C at pH 6 using the Brezovich limit was presumably an error, possibly caused by a temporary air bubble scattering light inside the UV-vis cuvette, and will not be discussed. Comparing the release curves to the loading, there was a strong negative correlation between the final release and the LE of the sample that was used. Among the pulsed experiments, AMFs following the Instrument limit did not result in a higher release than AMFs following the Brezovich limit. Comparing the release from FeNG10 in the static and pulsed experiments in the same mediums after

3 hours, there was only an increase using the AMF at 37 °C using the Brezovich limit at pH 3 and 6. For the static release experiments, there were no significant differences between the release of the two samples, or common trends for the release depending on the release medium used. The release profiles were generally more linear at pH 6 than 3, regardless of the temperature or applied AMF, as seen from the R^2-values for the zero-order release fit. Comparing the results from NG10 and FeNG10 in Figure 4.18 to that of NG25 and AuNG10, NG10 and FeNG10 exhibited higher overall release compared to NG25 and AuNG10, particularly AuNG10. Comparing the pulsed release in Figure 4.17 to the results for the double concentration, there was no difference in release resulting from the increase in concentration. As mentioned above, the results from the loading, the fit to zero-order kinetics, the NG25 and AuNG10 static release results, and pulsed FeNG10 results using a double concentration, can be seen in Appendix F.

The delayed diffusion of SA out of the membrane, illustrated in Figure 4.16b, would influence the release profiles. The increased delay at pH 3 could explain the lower linearity of the release profiles measured at this pH. The impact of the membrane on the experiments was analyzed by centrifuging the samples after several experiments and characterizing the absorbance of the supernatant to find the concentration of the released drug. The studies revealed the release inside the membrane to be three to seven times higher than what was detected in the UV-vis. Due to small parts of the membrane being permeable, as shown in Figure 3.5b, and the fact that several release curves stagnated at low values, this observation could be due to the blocking of pores by NGs.

The strong negative correlation between LE and the achieved release could result from the membrane limiting drug diffusion. However, since other parameters changed between the experiments, one cannot definitively conclude this correlation since it is also plausible that the high loading could result from interactions between the NGs and the drug, which would lead to reduced release. Furthermore, the different temperatures and pH values used prevent direct comparison of the release profiles. The opposite trend, higher LE resulting in a faster release, has been reported in the literature, explained by the increased concentration gradient assuming diffusion as a release mechanism [95]. This cannot be expected if the release mechanism i squeezing-out.

The absence of increased release at 25 °C when applying an AMF indicated that the rotational motion of the cNC particles had no effect. At this starting temperature, the heat generated by the cNC particles in FeNG10 would not be sufficient to induce a collapse, according to the results in Section 4.2.7. Hua et al. reported a two-fold increase in the release upon applying an AMF despite negligible heat generation, explained by the movement of the magnetic particles causing mechanical disruption in the polymer matrix [98]. The absence of this effect in this work could be due to a dominating Néel relaxation of cNC, while the magnetic particles of Hua et al. were much larger, indicating that Brownian relaxation could be dominating.

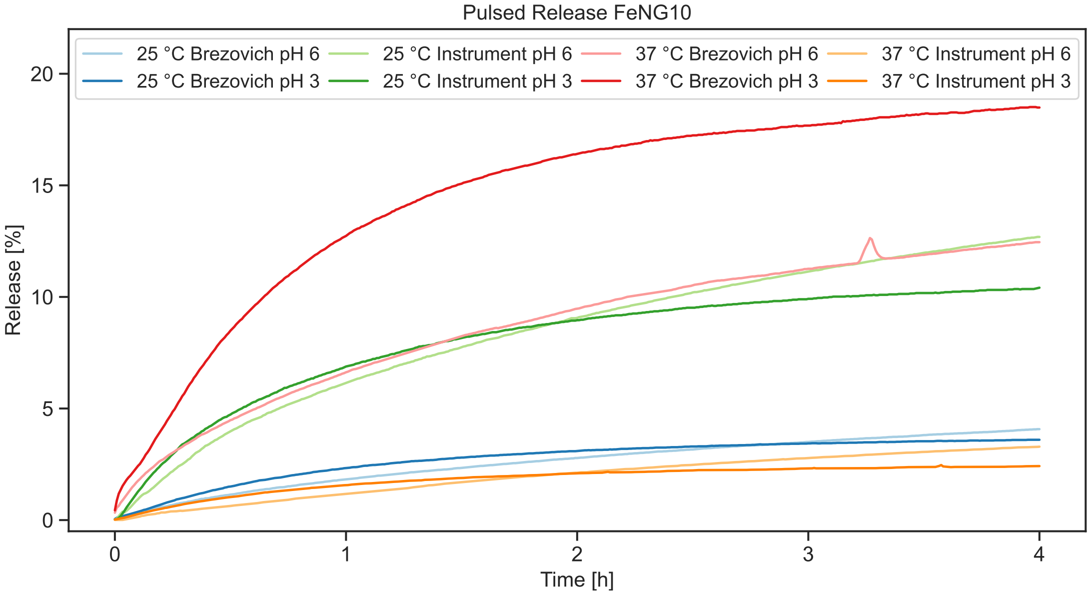

Figure 4.17: Pulsed release of SA from FeNG10, studied in the magneTherm set-up. An AMF with a frequency of 162 kHz and a field of 38 Oe (Brezovich limit) or 190 Oe (Instrument limit) was applied for 20 min, with 10 min breaks between the exposures.

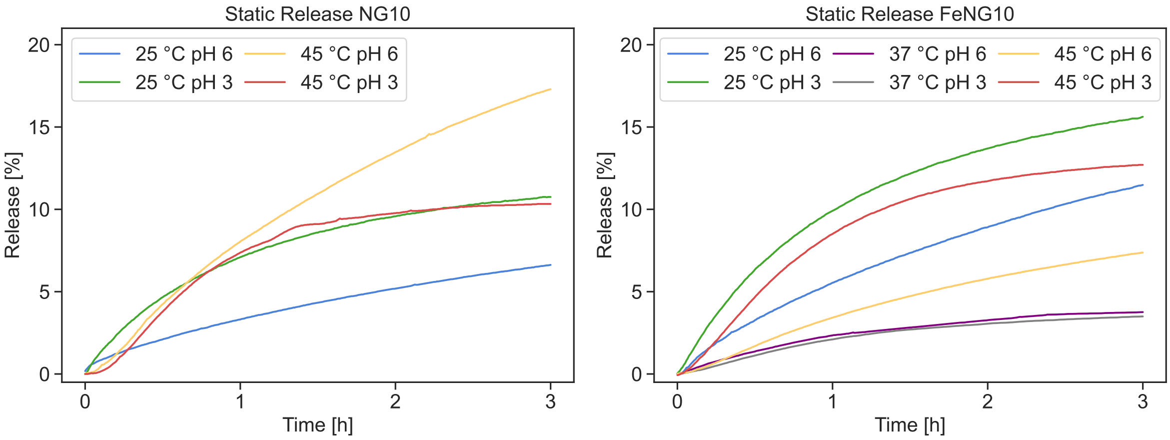

(a) NG10 (b) FeNG10

Figure 4.18: Static release of SA from NG10 and FeNG10, studied in the magneTherm set-up. Corresponding release profiles for NG25 and AuNG10 are shown in Appendix F.5. No AMF was applied for these studies.

For the studies at 37 °C, the heat generation by the cNC particles could affect the collapse of the NGs due to the starting temperature being close to the VPTT of FeNG10. The release was significantly increased using the Brezovich limit for both pH values, but this increase was not observed for the Instrument limit. This indicated that the increase was not due to the heat generated by the particles but other factors like differences in drug loading, or that the results were outliers. A double concentration of FeNG10 did not increase the release, as shown in Appendix F.5, indicating that a much higher concentration of cNC particles would be needed to generate sufficient heat for the application. In conclusion, the AMF pulses did not significantly affect the drug release results of FeNG10, independently of the temperature of the medium.

Considering the release from NG10, there was a small release without stimuli, which could result from diffusion, poorly bound drugs, or remaining supernatant left behind during cleaning. From Section 4.3.2, the assumed loading mechanism was physical encapsulation into the pores of the NG, which could lead to the small SA molecule diffusing out [94]. However, the observed release was almost linear, having an R^2 of 0.98 for the linear fit in Appendix F.1, and not following Fick's law, defined in Equation 2.27. This could indicate that the release was due to poorly bound drugs or remaining supernatant [104].

The increased release from NG10 upon application of stimuli could be due to a squeezing-out mechanism. NG10 experienced a high collapse upon temperature, pH, and dual stimuli, which have been reported to cause an efficient expulsion of encapsulated Cyt C from the polymer matrix through a squeezing-out mechanism [30, 94]. However, the release in response to each stimulus did not perfectly correlate with the magnitude of the corresponding VCE values. In particular, the release upon dual stimuli was similar to that of pH stimulus, while VCE_{dual} was closer to VCE_{temp}. This could indicate that the release of SA was not only governed by the squeezing-out mechanism but also by diffusion, which was also indicated by the release in the absence of stimuli. For small molecules like SA, the release could be faster at T<VPTT due to larger pores than at T>VPTT where the pores shrink, when diffusion is a release mechanism [8]. If both diffusion and squeezing-out were release mechanisms happening simultaneously, the effect of the collapse would consequently result in opposite effects for the two mechanisms, decreasing the release by diffusion and increasing the release by squeezing-out. The measured release at dual stimuli being closer to one of the pH stimulus than temperature could also be explained by the SA being detected more slowly at pH 3 than pH 6, in combination with the change in the hydrophilic-hydrophobic balance of NIPAM at elevated temperatures which could slow down the release of SA through increased hydrophobic interactions.

The observed trends for NG10 in the different release mediums were not common for all the samples. This could be due to differences in drug-carrier interactions and the membrane limiting the diffusion having a more significant effect on samples with higher LE. NG25 had a lower overall release than NG10, which could be due to the larger matrix volume for this sample, as seen from Figure 4.8a, giving a delay in the release since it would take the drug a long time to escape [30]. The release from NG25 was higher for the two individual stimuli than the dual stimuli, despite the higher VCE_{dual} than VCE_{temp} and VCE_{pH}. The release from AuNG10 was very low, which could result from any electrostatic or hydrophobic interactions between SA and

CTAB, as discussed in Section 4.3.2. Chemical bonds between the carrier and the drug would give a lower release than physical encapsulation [21]. Electrostatic and hydrophobic interactions are less strong than chemical bonds but could contribute to a slightly lower release. However, the electrostatic interactions would decrease when the pH was reduced below the pK_a of SA, implying a higher release at low pH, which was not observed. This could imply the interactions were hydrophobic. The release from AuNG10 did not seem to correlate to the VCE of the corresponding stimuli, and the release with no stimuli was higher than upon dual stimuli. FeNG10 generally had a high static release, except at 37 °C, where the samples used for these experiments had a particularly high LE, which might have caused a decrease in the release. With the exception of at 37 °C, the release using pH stimulus was high, despite FeNG10 having a very low $\mathrm{VCE}_{\mathrm{pH}}$. This could result from any electrostatic interactions of SA with TREG and TREA, making SA release when protonated.

In conclusion, the release was not increased through the applications of an AMF. The experiments indicated the release mechanism to be a combination of diffusion and squeezing-out due to the general increase of the release upon application of stimuli, combined with the lack of correlation between the release and the VCE due to the stimuli. Furthermore, there might be interactions between SA with FeNG10, as indicated by pH-dependent release, and with AuNG10, indicated by the very low release. Ideally, the release without stimuli should be zero to prevent leakage before reaching the target site, but this was not the case for neither of the samples. However, there were uncertainties related to the release profiles due to possible higher release limitations for samples with higher LE and the lower detection of the SA at low pH. Manual release experiments were performed in a separate set-up to provide more insight into the release mechanisms and to compare the release of SA with that of Cyt C.

4.4.2 Manual Release Studies

The manual drug release studies were performed as described in Section 3.5.2. The set-up included a membrane filled with 2 mL of an NG loaded with either SA or Cyt C, which was closed with dialysis clips and placed in a water bath with 1 L to ensure sink conditions. A magnetic stirrer provided a homogeneous release medium. The release was measured by characterizing the absorbance of the drug-loaded NGs before the release and every 30 min during the release. The absorbance of the drug-loaded NGs was normalized by the absorbance of the unloaded NGs in the specific medium since the absorbance of the NGs increased when they were in a collapsed state. Before the drug release experiments, preliminary experiments were executed to test and optimize the set-up.

Preliminary Studies for the Manual Release Studies

The kinetic drug loading studies presented in Section 4.3 concluded that the absorbance peaks of the loaded drugs were identical to the unloaded drugs. Consequently, the absorbance of the drug-loaded NGs inside the membrane could be used to characterize the drug release.

The kinetic study of SA at pH 3 and 45 °C for 3 hours presented in Section 4.4.1 was repeated for Cyt C with a 0.25 mg/mL concentration. The result is found in Appendix F.4, showing that the absorbance peak did not shift significantly, meaning that the obtained calibration curve could be used to characterize the drug release in the medium with pH 3 and 45 °C.

As a final preliminary study, the release of pure SA and Cyt C from inside the dialysis membrane was characterized to study the delay of the detected release. The results are shown in Figure 4.19, compared to the result obtained for SA in the magneTherm from Figure 4.16b. The release profiles were similar, with the release of SA using the manual method being slightly higher than the release of SA in the magneTherm, and the release of Cyt C slightly lower.

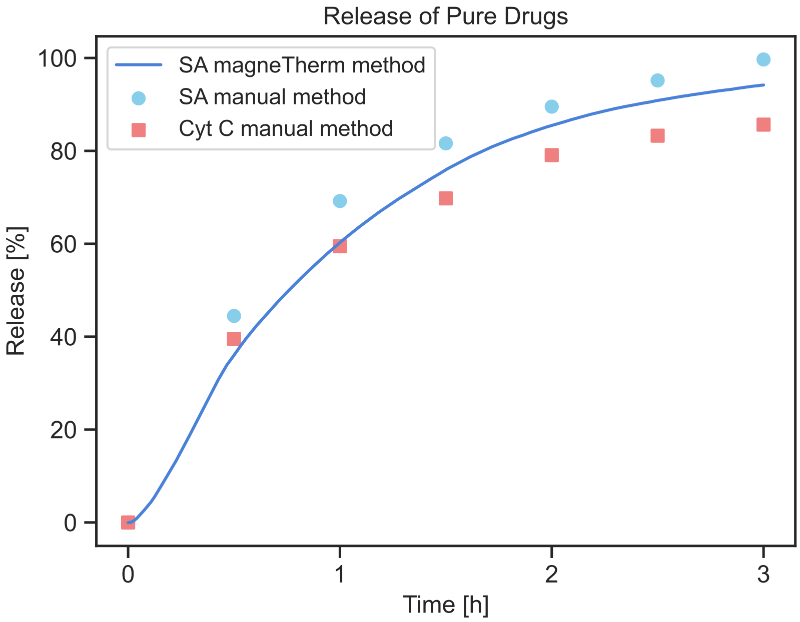

Figure 4.19: Comparison of the release of pure drugs from inside the membranes in the two drug release set-ups. The release from SA is shown using the magneTherm and manual set-up, and pure Cyt C is shown using the manual method. The studies were performed at pH 6 and 25 °C.

The three release profiles followed first-order release kinetics, explained by the drug diffusing out of the membrane due to a concentration gradient. The delay is still around 3 hours for SA using the manual method, as it was for the magneTherm, and slightly higher for Cyt C. Again, this delay must be considered when interpreting the release results. The release of Cyt C was lower than that of SA, which could result from the higher molecular weight. As the preliminary studies for the manual method have been presented, the drug release results will now be discussed.

Release from Nanogels Loaded with Salicylic Acid or Cytochrome C

Pulsed release experiments simulating a temperature change due to externally applied stimuli were conducted for all the NGs. For the first two hours, the pH was 6, while the temperature was pulsed between 45 °C for 20 min and 25 °C for 10 min. The pH was pulsed simultaneously for the remaining two hours with the temperature, being 3 for 20 min and 6 for 10 min. The results from the pulsed release experiments are found in Figure 4.20. As for the magneTherm release studies, four different static release studies were used for all the NGs at combinations of 25 and 45 °C with pH 6 and 3. The static experiments were performed for 3 hours using both SA and Cyt C. Figure 4.21 shows the results from the manual static release studies of NG10 and FeNG10 to compare with those from the magneTherm studies. Again, the NG25 and AuNG10 results provided no new information and are found in Appendix F.6, similarly as before.

The release was higher than what was obtained in the magneTherm. When comparing the release to the LE in Table F.1, there was no correlation. SA was consistently released faster than Cyt C in all measurements. The release of SA was the slowest for AuNG10. There was no common trend for which stimuli gave higher or lower release among the different samples in the static release experiments for either drug.

A few measurements showed a decrease in the release from one time-stamp to the next, namely the release of Cyt C from NG10 at 25 °C pH 6 and FeNG10 at 25 °C pH 3 between one and one and a half hours. In theory, a negative release should not be possible since the drug concentration gradient would only allow diffusion out of the membrane and not into it. The error could result from the measured absorbance in the membrane including the NGs, which could have variations in their transparency, thus introducing errors in the measurements.

The release was significantly higher in these experiments than the magneTherm experiments, despite the similar release of pure drugs illustrated in Figure 4.19. In Section 4.4.1, it was hypothesized that the NGs could cause a blockage for the drugs in the magneTherm set-up due to the small permeable areas of the release membrane. In comparison, the entire membrane in the manual set-up was permeable. The NGs blocking the SA in the magneTherm set-up could explain why the free SA had similar release kinetics in both set-ups, while the release from NGs was widely different.

Comparing the results from the pulsed release to that of the static release, only the release of Cyt C from AuNG10, in Appendix F.6, and FeNG10 was increased after 3 hours. It has been hypothesized that when the NGs collapse upon constant exposure to stimuli, the polymer network will form a skin on the surface of the NG, which can prevent a significant amount of the drug from escaping, and that a pulsed release would drastically increase the release [101]. Similar pulsed release studies using Cyt C

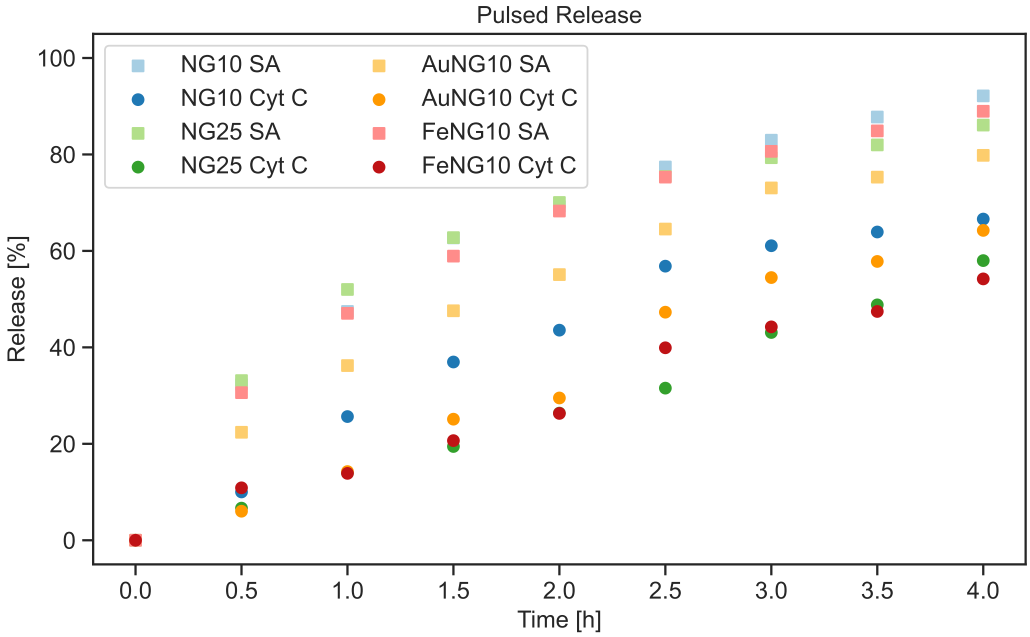

Figure 4.20: Pulsed release of SA and Cyt C from all the NGs, studied using the manual release set-up. 20 min of stimuli was applied, followed by 10 min without stimuli. For the first two hours, the stimulus was only temperature. For the last two hours, the stimuli were both temperature and pH.

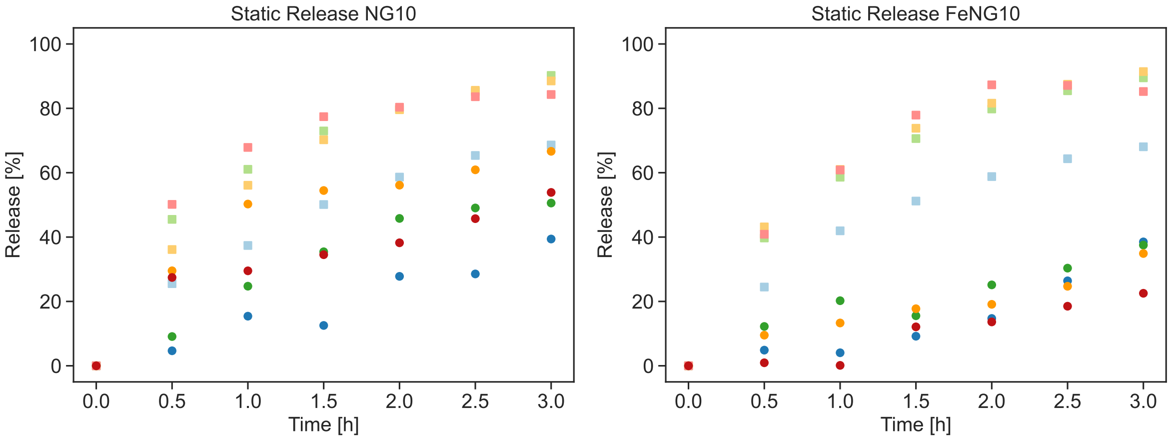

(a) NG10

(b) FeNG10

(c) Legend for static release

Figure 4.21: Static release of SA and Cyt C from NG10 and FeNG10, using the manual release set-up. Corresponding release profiles for NG25 and AuNG10 are shown in Appendix F.6.

from AuNG10 have shown 50 % of the drug to be released within the first hour, with a release kinetic close to zero-order [90]. In this work, the release was relatively close to zero-order for several samples, but for Cyt C the release was slower than reported in the literature, taking 3 to 4 hours to reach 50 %. The release of SA was faster, but closer to first-order.

SA was released faster than Cyt C for all the measurements, which could be a result of faster release from the NGs, the membrane, or both. The lower molecular weight of SA could allow it to escape both the pores of the NGs and the membrane faster, where the faster diffusion out of the membrane was established in Figure 4.19. However, the difference between the obtained release for SA and Cyt C was higher than the difference for the release of the pure drugs through the membrane, indicating that SA also was released faster from the NGs. Additionally, differences in the loading mechanism of the drugs could affect the relative release. Cyt C forms a protein-polymer complex with the NGs upon loading [94], which can be assumed stronger than the interactions between SA and the NGs, leading to slower release.

There was a burst release of SA for several measurements, characteristic of weakly bound drugs [21]. This observation supports the hypothesis that Cyt C was bound stronger to the NGs than SA. As for the magneTherm results, there was no consistency between the volumetric collapse and the release, in contrast to what has been observed in the literature for similar NGs loaded with Cyt C [30, 94, 95], indicating that the squeezing-out mechanism was not dominating for the release of SA. Furthermore, the differences between the stimuli for the individual samples were minimal. The slow release of SA from AuNG10 was still observed, where possible mechanisms for this have been discussed.

Cyt C loaded via breathing-in methods has been found to travel inside the pores of NGs and require stimuli and time to release [94], but in this work, there was a high leakage out of the NGs without stimuli. This could indicate that the drug was poorly bound. In the literature, dual stimuli have been found to give significantly higher release compared to pH or temperature individually, both for bare NGs [30] and for NGs incorporated with NPs [94]. The low effect of dual stimuli in this work could be due to the enhanced deprotonation of AAc at increasing temperatures [30]. Furthermore, the differences in the literature only became significant after more extended periods than the 3 hours measured in this work. In this work, the differences between the different stimuli were minor for the release of Cyt C, just as for the release of SA.

The release profiles obtained in these experiments were generally more linear than those obtained in the magneTherm, closer to zero-order. SA was released faster than Cyt C, most likely due to its smaller size and weaker interactions with the NGs, and generally had a less linear release profile. The release profile of Cyt C was particularly linear for the pulsed experiments, promising for targeted drug delivery applications. However, there was an overall high leakage of the drugs in the absence of stimuli, which would pose a problem for the targeted drug delivery application, as the intended specificity of the system will be drastically reduced. For most experiments, the release when no stimuli were applied was very similar to the release when stimuli were applied. No samples consistently showed a low leakage and a high stimuli-induced release.

Chapter 5

Conclusion

The motivation behind this work was to achieve a predictable and externally controlled release to address the challenges of systemic cancer treatment, using a hybrid NG-based targeted drug delivery system. Important aspects that were addressed were developing IONPs with sufficient heating efficiency, NGs with a high collapse at relevant temperatures, the preservation of the magnetic and optical properties of inorganic NP upon the incorporation into the NGs, a sufficient drug loading capacity, and a controllable release in response to applied stimuli.

The main objective of this work was to obtain an externally controllable zero-order release using stimuli. However, no increase in the release was observed when an AMF was applied to the IONP NGs, neither from the rotation nor heat generation of the IONPs. Although there was a partial increase in the release upon application of stimuli in the form of increased temperature, decreased pH, or both, the difference was low compared to the drug leakage in the absence of stimuli. Conducting longer experiments could provide clearer insight into the effect of stimuli on the release. The results indicated that the release mechanism for both SA and Cyt C involved a combination of diffusion and squeezing-out, with some samples exhibiting kinetics near zero-order, but with a low release rate. The release of SA was faster due to its smaller size and presumed weaker interactions with the NGs. The experimental findings were limited by the significant delay caused by the dialysis membranes, particularly in the magneTherm. This problem could potentially be solved by a membrane with larger permeable parts.

Magnetite IONP clusters were obtained with a very high heating efficiency when subjected to clinically relevant AMFs. This high heating efficiency was attributed to a significant hysteresis loss in addition to relaxation mechanisms, high saturation magnetization, susceptibility, colloidal stability, and possibly the coupling between the relaxation time and the AMF frequency. The magnetic properties were possibly influenced by reduced spin canting and oxidation of the particles in the clusters, but further investigations are needed to confirm this hypothesis. Upon incorporation into NGs, the superparamagnetic properties of the IONCs were conserved. However, poor incorporation into the NGs reduced the magnetization and heating efficiency, which could explain why there was no increase in the release of these NGs under the applied AMF. The incorporation could have been improved by using a mechanical stirrer instead of a magnetic stirrer.

All the NGs collapsed in response to an increased temperature, decreased pH, and both, explained by the temperature and pH dependency of the NIPAM and AAc monomers, respectively. The VCE was higher for temperature than for pH due to the higher concentration of NIPAM than AAc. For some of the samples, the VCE was higher for temperature than for the dual stimuli, which could be because the pH was lowered first, which changed the properties of the NGs before the temperature was increased. The VPTTs of the bare NGs were too low, and could be further tuned by introducing more AAc, while the VPTTs of the hybrid NGs were highly relevant for the drug delivery application.

The NGs exhibited high loading capacities for both SA and Cyt C, but the loading experiments had poor reproducibility. Proposed loading mechanisms were physical encapsulations of the drugs into the pores of the NGs, based on the increased loading into the larger NGs, and interactions between the NGs and the drugs. The bare NGs had a high loading of Cyt C, which could be explained by the formation of a polymer-protein complex from electrostatic interactions between AAc and Cyt C. The hybrid NGs had high loading of SA, which could be due to electrostatic interactions between SA and the inorganic NPs, and hydrophobic interactions between SA and the CTAB tail. The hybrid NGs had a reduced Cyt C loading due to the inorganic NPs occupying binding sites.

Lastly, the high LSPR peak in the NIR region of the EM spectrum of AuERs was preserved upon incorporation into NGs. This indicated that these hybrid NGs could be used for photothermal heating, but this was not characterized.

In conclusion, both the IONPs and the NGs showed promise for targeted drug delivery applications individually due to excellent heating and stimuli-responsive properties. However, the hybrid system proved unsuccessful in the drug release studies, and did not obtain a predictable and externally controllable release. This study contributes insights into the importance of the interactions between the different components in the system for its drug release performance. Still, optimization of the system is needed before it can become predictable enough for the clinical stage. Suggestions for such improvements will be elaborated on in the future work section concluding this work.

Chapter 6

Future Work

As concluded, the individual components of the hybrid system had the potential for the application of targeted drug delivery. However, further research is needed to optimize the combined system and further investigate its properties in biologically relevant environments to ensure predictable release. Therefore, the following studies are suggested for any future work on the system.

Firstly, the absence of the influence of the AMF on the release was hypothesized to be a result of the low incorporation of the IONPs into the NGs, giving insufficient heating and mechanical disruption. Consequently, a higher incorporation is suggested for future experiments. Additionally, since the magnetic stirrer proved a challenge for the incorporation of the magnetic NPs, a mechanically stirred set-up should be employed for the NG synthesis.

Furthermore, additional drug release studies should be conducted to predict the release from this system better. For this purpose, longer drug release studies should be conducted to better understand the complete effect of the stimuli on the release compared to the release in the absence of the stimuli. Additionally, the effect of the AMF on the release should be investigated deeper, which could be done by attempting different pulses, continuous fields, or different frequencies, since the relaxation time of the IONPs could change when incorporated into the NGs. The release from the NGs should also be investigated in different biologically relevant environments, including at 37 °C and at pH 5. Furthermore, biologically relevant buffers with a low pH could be used as a release medium, instead of MQ water with a pH adjusted using HCl, as was used in this work. Lastly, the performance of the system in a medium simulating blood should be explored.

Further optimization of the drug loading process is needed due to the poor reproducibility of the drug loading, as seen from Appendix F.2. Additionally, loading the NGs with a mixture of SA and Cyt C could provide insights into the loading mechanisms of the drugs, and possibly increase the total loading. Furthermore, release studies in the magneTherm using a drug with similar properties as Cyt C but with a lower molecular weight could be conducted to examine the effect of the drug properties on the release. A drug with a higher molecular weight than SA should be studied to see if it would lower the diffusion of the drug out of the NGs.

The optical heating properties of the AuERs both before and after incorporation into the NGs should be examined. The photothermal effect could be an alternative to the AMF stimulus, and the release in response to pulses of irradiation should be studied.

Lastly, the different mechanisms within the system could be investigated further. Investigating the assumed interactions between the particles constituting the clusters would be interesting. Furthermore, the pH at which the NGs experience the collapse, analogous to the VPTT, could be characterized in order to predict the behavior of the NGs in tumor environments. Lastly, the drug interaction with the NGs and NPs should be further explored.

To conclude, if all the presented challenges are overcome, this hybrid targeted drug delivery system has the potential to revolutionize cancer therapy by drastically reducing side-effects in addition to improving therapeutic effects.

References

[1] World Health Organization. *Cancer*. Last accessed 25 February 2023. 2023.

[2] Yan Wang et al. 'Applications of magnetic nanoparticles in biomedicine'. *Journal of Physics* 36 (2003), pp. 167–181. DOI: `10.1088/0022-3727/36/13/201`.

[3] Sudipta Senapati et al. 'Controlled drug delivery vehicles for cancer treatment and their performance'. *Nature: Signal transduction and targeted therapy* 3.1 (2018), pp. 1–19. DOI: `10.1038/s41392-017-0004-3`.

[4] Archana Swami et al. *Nanoparticles for Targeted and Temporally Controlled Drug Delivery*. Ed. by Sonke Svenson and Robert K. Prud'homme. Boston, MA: Springer US, 2012, pp. 9–29. ISBN: 978-1-4614-2305-8.

[5] Frank X Gu et al. 'Targeted nanoparticles for cancer therapy'. *Nano today* 2.3 (2007), pp. 14–21. DOI: `10.1016/S1748-0132(07)70083-X`.

[6] Jing Su et al. 'Catechol Polymers for pH-Responsive, Targeted Drug Delivery to Cancer Cells'. *Journal of the American Chemical Society* 133 (2011), pp. 11850–11853. DOI: `10.1021/ja203077x`.

[7] Ran Mo. 'Recent progress in multidrug delivery to cancer cells by liposomes'. *Nanomedicine* 9.8 (2014), pp. 1117–1120. DOI: `10.2217/nnm.14.62`.

[8] Satish Nayak et al. 'Soft Nanotechnology with Soft Nanoparticles Angewandte Chemie'. *Reviews* 44 (2005), pp. 7686–7708. DOI: `10.1002/anie.200501321`.

[9] Zhaoyi Sun et al. 'Hydrogel-Based Controlled Drug Delivery for Cancer Treatment: A Review'. *Mol. Pharmaceutics* 17 (2020), p. 391. DOI: `10.1021/acs.molpharmaceut.9b01020`.

[10] Dipak Maity et al. 'Studies of magnetite nanoparticles synthesized by thermal decomposition of iron (III) acetylacetonate in tri(ethylene glycol)'. *Journal of Magnetism and Magnetic Materials* 321.19 (2009), pp. 3093–3098. ISSN: 03048853. DOI: `10.1016/j.jmmm.2009.05.020`.

[11] Dipak Maity et al. 'Novel synthesis of superparamagnetic magnetite nanoclusters for biomedical applications'. *Journal of Materials Chemistry* 21 (2011), pp. 14717–14724. DOI: `10.1039/c1jm11982f`.

[12] Stefan Maier. *Plasmonics: fundamentals and applications*. Vol. 1. Springer, 2007. ISBN: 9781441941138.

[13] Xiaobang Hou et al. 'Controlled Release of Agrochemicals Using pH and Redox Dual-Responsive Cellulose Nanogels'. *Journal of Agricultural and Food Chemistry* 67.24 (2019), pp. 6700–6707. DOI: `10.1021/acs.jafc.9b00536`.

[14] Daisuke Tada et al. ‘Drug release from hydrogel containing albumin as crosslinker’. *Journal of Bioscience and Bioengineering* 100.5 (2005), pp. 551–555. DOI: `10.1263/JBB.100.551`.

[15] Yan Wang et al. ‘Monitoring the hydrolyzation of aspirin during the dissolution testing for aspirin delayed-release tablets with a fiber-optic dissolution system’. *Journal of Pharmaceutical Analysis* 2.5 (2012), pp. 386–389. DOI: `10.1016/j.jpha.2012.06.002`.

[16] Gerald Litwack. *NO Binding to the Proapoptotic Cytochrome c–Cardiolipin Complex*. Vol. 96. Vitamins & Hormones. Academic Press, 2014, pp. 193–209. DOI: `10.1016/B978-0-12-800254-4.00008-8`.

[17] Carlos Bárcena. ‘Applications of magnetic nanoparticles in biomedicine’. *Nanoscale Magnetic Materials and Applications* (2009), pp. 591–626. DOI: `10.1007/978-0-387-85600-1`.

[18] Alaaldin M Alkilany et al. ‘Cellular uptake of nanoparticles: journey inside the cell’. *Chem. Soc. Rev* 46.14 (2016), pp. 4218–4244. ISSN: 0306-0012. DOI: `10.1039/c6cs00636a`.

[19] John William Mullin. *Crystallization*. Elsevier, 2001. ISBN: 9780080530116.

[20] *BioRender.com*. Last accessed 27 July 2023. 2023.

[21] Sulalit Bandyopadhyay. *Fabrication and Application of Nanomaterials*. McGraw-Hill Education, 2019. ISBN: 9781260132236.

[22] Stephen Blundell. *Magnetism in condensed matter*. American Association of Physics Teachers, 2003. ISBN: 9780198505921.

[23] Guozhong Cao. *Nanostructures & nanomaterials: synthesis, properties & applications*. Imperial college press, 2004. ISBN: 9781860944154.

[24] Victor K Lamer and Robert H Dinegar. ‘Theory, Production and Mechanism of Formation of Monodispersed Hydrosols’. *Journal of the American Chemical Society* 72.11 (1950), pp. 4847–4854.

[25] Georgios M Kontogeorgis and Soren Kiil. *Introduction to applied colloid and surface chemistry*. John Wiley & Sons, 2016. ISBN: 9781118881187.

[26] K Lance Kelly et al. ‘The Optical Properties of Metal Nanoparticles: The Influence of Size, Shape, and Dielectric Environment’. *The Journal of Physical Chemistry B* 107.3 (2003), pp. 668–677. DOI: `10.1021/jp026731y`.

[27] Philip Hofmann. *Solid state physics: an introduction*. John Wiley & Sons, 2022. ISBN: 9783527408610.

[28] John MD Coey. *Magnetism and magnetic materials*. Cambridge university press, 2010. ISBN: 9780521816144.

[29] Yaman Boluk and Christophe Danumah. ‘Analysis of cellulose nanocrystal rod lengths by dynamic light scattering and electron microscopy’. *Journal of Nanoparticle Research* 16.1 (2014). DOI: `10.1007/s11051-013-2174-4`.

[30] Anuvansh Sharma et al. ‘Modulating acrylic acid content of nanogels for drug delivery & biocompatibility studies’. *Journal of Colloid and Interface Science* 607 (2022), pp. 76–88. ISSN: 0021-9797. DOI: `10.1016/J.JCIS.2021.07.139`.

[31] Lacramioara Popa. *Hydrogels: Smart Materials for Biomedical Applications*. BoD–Books on Demand, 2019. ISBN: 9781789858754.

[32] Sulalit Bandyopadhyay et al. 'A robust method to calculate the volume phase transition temperature (VPTT) for hydrogels and hybrids'. *RSC Advances* 7.84 (2017), pp. 53192–53202. DOI: `10.1039/c7ra10258e`.

[33] B Devika Chithrani. 'Determining the Size and Shape Dependence of Gold Nanoparticle Uptake into Mammalian Cells'. *Nano Letters* 6.4 (2006), pp. 662–668. DOI: `10.1021/nl052396o`.

[34] Nadine Pernodet et al. 'Adverse Effects of Citrate/Gold Nanoparticles on Human Dermal Fibroblasts'. *Small* 2.6 (2006), pp. 766–773. DOI: `10.1002/smll.200500492`.

[35] Yu Pan et al. 'Size-Dependent Cytotoxicity of Gold Nanoparticles'. *Small* 3.11 (2007), pp. 1941–1949. DOI: `10.1002/smll.200700378`.

[36] Hung-Jen Yen. 'Cytotoxicity and Immunological Response of Gold and Silver Nanoparticles of Different Sizes'. *Small* 5.13 (2009), pp. 1553–1561. DOI: `10.1002/smll.200900126`.

[37] Catherine M Goodman et al. 'Toxicity of Gold Nanoparticles Functionalized with Cationic and Anionic Side Chains'. *Bioconjugate Chemistry* 15.4 (2004), pp. 897–900. DOI: `10.1021/bc049951i`.

[38] Euiyeon Lee et al. 'Molecular origin of AuNPs-induced cytotoxicity and mechanistic study'. *Scientific reports* 9.1 (2019), pp. 1–13. DOI: `10.1038/s41598-019-39579-3`.

[39] Karthik Raghunathan et al. 'Tuning and tracking the growth of gold nanoparticles synthesized using binary surfactant mixtures'. *Nanoscale Advances* 2.5 (2020), pp. 1980–1992. DOI: `10.1039/d0na00214c`.

[40] Waqqar Ahmed et al. 'Facile synthesis of gold nanoworms with a tunable length and aspect ratio through oriented attachment of nanoparticles'. *Nanoscale* 6.21 (2014), pp. 13222–13227. DOI: `10.1039/c4nr04122d`.

[41] Heloise Ribeiro de Barros et al. 'Surface interactions of gold nanorods and polysaccharides: From clusters to individual nanoparticles'. *Carbohydrate Polymers* 152 (2016), pp. 479–486. DOI: `10.1016/j.carbpol.2016.07.018`.

[42] Sulalit Bandyopadhyay et al. 'Shape tunable synthesis of anisotropic gold nanostructures through binary surfactant mixtures'. *Materials Today Chemistry* 3 (2017), pp. 1–9. DOI: `10.1016/j.mtchem.2016.11.005`.

[43] Takahito Kawano et al. 'PNIPAM gel-coated gold nanorods for targeted delivery responding to a near-infrared laser'. *Bioconjugate Chemistry* 20.2 (2009), pp. 209–212. DOI: `10.1021/bc800480k`.

[44] Ralph Weissleder. 'A clearer vision for in vivo imaging'. *Nature Biotechnology* 19.4 (2001), pp. 316–317. DOI: `10.1038/86684`.

[45] Lucian Fodor, Yehuda Ullmann and Monica Elman. *Aesthetic applications of intense pulsed light*. Springer, 2011. ISBN: 9783030228286.

[46] Esther Cazares-Cortes et al. 'Magnetic Nanoparticles Create Hot Spots in Polymer Matrix for Controlled Drug Release'. *nanomaterials* 8.10 (2018), p. 850. DOI: `10.3390/nano8100850`.

[47] Joanna Dulí Nska-Litewka et al. 'Superparamagnetic Iron Oxide Nanoparticles-Current and Prospective Medical Applications'. *Materials* 12.4 (2019), p. 617. DOI: `10.3390/ma12040617`.

[48] C. Ravikumar and Rajdip Bandyopadhyaya. 'Mechanistic study on magnetite nanoparticle formation by thermal decomposition and coprecipitation routes'. *Journal of Physical Chemistry C* 115.5 (2011), pp. 1380–1387. DOI: `10.1021/jp105304w`.

[49] A. Lassenberger et al. 'Monodisperse Iron Oxide Nanoparticles by Thermal Decomposition: Elucidating Particle Formation by Second-Resolved in Situ Small-Angle X-ray Scattering'. *Chemistry of Materials* 29.10 (2017), pp. 4511–4522. DOI: `10.1021/acs.chemmater.7b01207`.

[50] Geoffrey Cotin et al. 'A Confinement-Driven Nucleation Mechanism of Metal Oxide Nanoparticles Obtained via Thermal Decomposition in Organic Media'. *Small* 18.20 (2022). DOI: `10.1002/smll.202200414`.

[51] Jongnam Park et al. 'Ultra-large-scale syntheses of monodisperse nanocrystals'. *Nature Materials* 3.12 (2004), pp. 891–895. DOI: `10.1038/nmat1251`.

[52] Maria F. Casula et al. 'The concept of delayed nucleation in nanocrystal growth demonstrated for the case of iron oxide nanodisks'. *Journal of the American Chemical Society* 128.5 (2006), pp. 1675–1682. DOI: `10.1021/ja056139x`.

[53] Zhen Li, Qiao Sun and Mingyuan Gao. 'Preparation of water-soluble magnetite nanocrystals from hydrated ferric salts in 2-pyrrolidone: Mechanism leading to Fe3O4'. *Angewandte Chemie - International Edition* 44.1 (2004), pp. 123–126. DOI: `10.1002/anie.200460715`.

[54] Hyung Jun Park, Dong Jun Shin and Junhua Yu. 'Categorization of Quantum Dots, Clusters, Nanoclusters, and Nanodots'. *Journal of Chemical Education* 98.3 (2021), pp. 703–709. DOI: `10.1021/acs.jchemed.0c01403`.

[55] Changming Cheng et al. 'Tunable synthesis of carboxyl-functionalized magnetite nanocrystal clusters with uniform size'. *Journal of Materials Chemistry* 19.46 (2009), pp. 8782–8788. DOI: `10.1039/B910832G`.

[56] Victor L. Kirillov et al. 'Size control in the formation of magnetite nanoparticles in the presence of citrate ions'. *Materials Chemistry and Physics* 145.1-2 (2014), pp. 75–81. DOI: `10.1016/j.matchemphys.2014.01.036`.

[57] Andrea Atrei et al. 'Effect of Citrate on the Size and the Magnetic Properties of Primary Fe3O4 Nanoparticles and Their Aggregates'. *Applied Sciences (Switzerland)* 11.15 (2021). DOI: `10.3390/app11156974`.

[58] Xiao Li Liu et al. 'Optimization of surface coating on Fe3O4 nanoparticles for high performance magnetic hyperthermia agents'. *Journal of Materials Chemistry* 22.17 (2012), pp. 8235–8244. DOI: `10.1039/c2jm30472d`.

[59] Marcela Stoia, Roxana Istratie and Cornelia Păcurariu. 'Investigation of magnetite nanoparticles stability in air by thermal analysis and FTIR spectroscopy'. *Journal of Thermal Analysis and Calorimetry* 125.3 (2016), pp. 1185–1198. DOI: `10.1007/s10973-016-5393-y`.

[60] Aurel Ercuta and Marius Chirita. 'Highly crystalline porous magnetite and vacancy-ordered maghemite microcrystals of rhombohedral habit'. *Journal of*

Crystal Growth 380 (2013), pp. 182–186. DOI: `10.1016/j.jcrysgro.2013.06.003`.

[61] Maria Cristina Mascolo, Yongbing Pei and Terry A. Ring. ‘Room Temperature Co-Precipitation Synthesis of Magnetite Nanoparticles in a Large pH Window with Different Bases’. *Materials* 6.12 (2013), pp. 5549–5567. DOI: `10.3390/ma6125549`.

[62] D. X. Chen et al. ‘Size determination of superparamagnetic nanoparticles from magnetization curve’. *Journal of Applied Physics* 105.8 (2009). DOI: `10.1063/1.3117512`.

[63] Ibtessam Alotaibi et al. ‘Synthesis, characterization and heating efficiency of Gd-doped maghemite (γ-Fe2O3) nanoparticles for hyperthermia application’. *Physica B: Condensed Matter* 625 (2022). DOI: `10.1016/j.physb.2021.413510`.

[64] Andreas Bogen Kristiansen, Nathan Church and Seniz Ucar. ‘Investigation of magnetite particle characteristics in relation to crystallization pathways’. *Powder Technology* 415 (2023), p. 118145. DOI: `10.1016/J.POWTEC.2022.118145`.

[65] Mythreyi Unni et al. ‘Thermal Decomposition Synthesis of Iron Oxide Nanoparticles with Diminished Magnetic Dead Layer by Controlled Addition of Oxygen’. *ACS Nano* 11.2 (2017), pp. 2284–2303. DOI: `10.1021/acsnano.7b00609`.

[66] André M. Pereira et al. ‘Unravelling the effect of interparticle interactions and surface spin canting in γ-Fe2O3@SiO2 superparamagnetic nanoparticles’. *Journal of Applied Physics* 109.11 (2011). DOI: `10.1063/1.3583652`.

[67] Sheng Peng et al. ‘Synthesis and Stabilization of Monodisperse Fe Nanoparticles’. *Journal of the American Chemical Society* 128 (2006), p. 10677. DOI: `10.1021/ja063969h`.

[68] Bagher Aslibeiki et al. ‘The effect of interparticle interactions on spin glass and hyperthermia properties of Fe3O4 nanoparticles’. *Materials Research Express* 4.7 (2017). DOI: `10.1088/2053-1591/aa7eb1`.

[69] Alison Deatsch and Benjamin Evans. ‘Heating efficiency in magnetic nanoparticle hyperthermia’. *Journal of Magnetism and Magnetic Materials* 354 (2014), pp. 163–172. DOI: `10.1016/j.jmmm.2013.11.006`.

[70] Cindy Dennis et al. ‘Nearly complete regression of tumors via collective behavior of magnetic nanoparticles in hyperthermia’. *Nanotechnology* 20.39 (2009). DOI: `10.1088/0957-4484/20/39/395103`.

[71] Yuri I. Golovin et al. ‘Theranostic multimodal potential of magnetic nanoparticles actuated by non-heating low frequency magnetic field in the new-generation nanomedicine’. *Journal of Nanoparticle Research* 19.2 (2017). DOI: `10.1007/s11051-017-3746-5`.

[72] Fridon Shubitidze, Katsiaryna Kekalo and Robert Stigliano. ‘Magnetic nanoparticles with high specific absorption rate of electromagnetic energy at low field strength for hyperthermia therapy’. *Journal of Applied Physics* 117 (2015), p. 94302. DOI: `10.1063/1.4907915`.

[73] Mathew Kallumadil et al. 'Suitability of commercial colloids for magnetic hyperthermia'. *Journal of Magnetism and Magnetic Materials* 321.10 (2009), pp. 1509–1513. DOI: `10.1016/j.jmmm.2009.02.075`.

[74] Venkatesha Narayanaswamy et al. 'Role of magnetite nanoparticles size and concentration on hyperthermia under various field frequencies and strengths'. *Molecules* 26.4 (2021). ISSN: 14203049. DOI: `10.3390/molecules26040796`.

[75] Yolanda Piñeiro-Redondo et al. 'The influence of colloidal parameters on the specific power absorption of PAA-coated magnetite nanoparticles'. *Nanoscale Research Letters* 6 (2011), pp. 1–7. DOI: `10.1186/1556-276X-6-383`.

[76] Ivan A Brezovich, William J Atkinson and Michael B Lilly. 'Local Hyperthermia with Interstitial Techniques'. *Cancer Research* 44 (1984), pp. 4752–4756. ISSN: 6380712.

[77] Rudolf Hergt and Silvio Dutz. 'Magnetic particle hyperthermia-biophysical limitations of a visionary tumour therapy'. *Journal of Magnetism and Magnetic Materials* 311.1 (2007), pp. 187–192. DOI: `10.1016/j.jmmm.2006.10.1156`.

[78] Borja Herrero de la Parte et al. 'Proposal of New Safety Limits for In Vivo Experiments of Magnetic Hyperthermia Antitumor Therapy'. *Cancers* 14.13 (2022). DOI: `10.3390/cancers14133084`.

[79] R. R. Wildeboer, P. Southern and Q. A. Pankhurst. 'On the reliable measurement of specific absorption rates and intrinsic loss parameters in magnetic hyperthermia materials'. *Journal of Physics D: Applied Physics* 47.49 (2014). DOI: `10.1088/0022-3727/47/49/495003`.

[80] B. Leber et al. 'Impact of Temperature on Cell Death in a Cell-culture Model of Hepatocellular Carcinoma'. *Anticancer Research* 32 (2012), pp. 915–922. ISSN: 22399612.

[81] Chinthaka P. Gooneratne et al. 'Analysis of the Distribution of Magnetic Fluid inside Tumors by a Giant Magnetoresistance Probe'. *PLoS ONE* 8.11 (2013), p. 81227. DOI: `10.1371/journal.pone.0081227`.

[82] Yun Kyoung Kim et al. 'Dual Stimuli-Triggered Nanogels in Response to Temperature and pH Changes for Controlled Drug Release'. *Nanoscale Research Letters* 14 (2019). DOI: `10.1186/s11671-019-2909-y`.

[83] George Odian. *Principles of polymerization.* John Wiley & Sons, 2004. ISBN: 9780070475854.

[84] Daniel Morales et al. 'Single-Step Binary Electrostatic Directed Assembly of Active Nanogels for Smart Concentration-Dependent Encryption'. *Langmuir* 34.4 (2018), pp. 1557–1563. DOI: `10.1021/acs.langmuir.7b03519`.

[85] Marzieh Danaei et al. 'Impact of particle size and polydispersity index on the clinical applications of lipidic nanocarrier systems'. *Pharmaceutics* 10.2 (2018). DOI: `10.3390/pharmaceutics10020057`.

[86] Howard G Schild. 'Poly (N-isopropylacrylamide): experiment, theory and application'. *Progress in polymer science* 17.2 (1992), pp. 163–249. DOI: `10.1016/0079-6700(92)90023-R`.

[87] William H Blackburn and L Andrew Lyon. 'Size-controlled synthesis of monodisperse core/shell nanogels'. *Colloid Polymer Science* 286 (2008), pp. 563–569. DOI: `10.1007/s00396-007-1805-7`.

[88] Anil Kumar Bajpai and M Shrivastava. 'Swelling Kinetics of a Hydrogel of Poly(ethylene glycol) and Poly(acrylamide-co-styrene)'. *J Appl Polym Sci* 85.7 (2002), pp. 1419–1428. DOI: `10.1002/app.10675`.

[89] Travis W. Jarrells et al. 'Quantification of Monomer Units in Insoluble Polymeric Active Pharmaceutical Ingredients Using Solid-State NMR Spectroscopy I: Patiromer'. *AAPS PharmSciTech* 21.3 (2020). DOI: `10.1208/s12249-020-01654-8`.

[90] Karthik Raghunathan. 'Integrated Experimental and Computational Studies on Plasmonic Nanoparticles'. PhD thesis. Norwegian University of Science and Technology, 2023. ISBN: 9788232670048.

[91] Haiyang Yao et al. 'Synthesis and self-assembly of multiple-responsive magnetic nanogels'. *Polymers for Advanced Technologies* 30.2 (2019), pp. 312–319. DOI: `10.1002/pat.4467`.

[92] Shamsul Hayat et al. *Salicylic Acid*. 2013. ISBN: 9781402051838.

[93] Satit Puttipipatkhachorn et al. 'Drug physical state and drug-polymer interaction on drug release from chitosan matrix films'. *Journal of Controlled Release* 75.1-2 (2001), pp. 143–153. DOI: `10.1016/S0168-3659(01)00389-3`.

[94] Sulalit Bandyopadhyay et al. 'Incorporation of Fe@Au nanoparticles into multiresponsive pNIPAM-AAc colloidal gels modulates drug uptake and release'. *Colloid polymer science* 294 (2016), pp. 1929–1942. DOI: `10.1007/s00396-016-3944-1`.

[95] Sulalit Bandyopadhyay, Anuvansh Sharma and Wilhelm Robert Glomm. 'The influence of differently shaped gold nanoparticles functionalized with nipam-based hydrogels on the release of cytochrome c'. *Gels* 3.4 (2017). DOI: `10.3390/gels3040042`.

[96] Rajesh Raju et al. 'Synthesis, Characterization and Drug Loading of Multiresponsive p[NIPAm-co-PEGMA] (core)/p[NIPAm-co-AAc] (Shell) Nanogels with Monodisperse Size Distributions'. *Polymers* 10.3 (2018), p. 309. DOI: `10.3390/polym10030309`.

[97] Weitai Wu et al. 'Core-shell hybrid nanogels for integration of optical temperature-sensing, targeted tumor cell imaging, and combined chemo-photothermal treatment'. *Biomaterials* 31.29 (2010), pp. 7555–7566. DOI: `10.1016/j.biomaterials.2010.06.030`.

[98] Xin Hua et al. 'Externally Controlled Triggered-Release of Drug from PLGA Micro and Nanoparticles'. *Plos One* 9.12 (2014). DOI: `10.1371/journal.pone.0114271`.

[99] Xinyu Hu et al. 'Magnetic field-driven drug release from modified iron oxide-integrated polysaccharide hydrogel'. *International Journal of Biological Macromolecules* 108 (2018), pp. 558–567. DOI: `10.1016/J.IJBIOMAC.2017.12.018`.

[100] Baeckkyoung Sung, Min Ho Kim and Leon Abelmann. 'Magnetic microgels and nanogels: Physical mechanisms and biomedical applications'. *Bioengineering and Translational Medicine* 6.1 (2021). DOI: `10.1002/btm2.10190`.

[101] Jian Tao Zhang et al. 'Poly(N-isopropylacrylamide) nanoparticle-incorporated PNIPAAm hydrogels with fast shrinking kinetics'. *Macromolecular Rapid Communications* 26.16 (2005), pp. 1346–1350. DOI: `10.1002/marc.200500298`.

[102] Mohammad Barzegar-Jalali et al. 'Kinetic Analysis of Drug Release From Nanoparticles'. *J Pharm Pharmaceut Sci* 11.1 (2008), pp. 167–177. DOI: `10.18433/J3D59T`.

[103] Roya Salehi, Sepideh Rasouli and Hamed Hamishehkar. 'Smart thermo/pH responsive magnetic nanogels for the simultaneous delivery of doxorubicin and methotrexate'. *International Journal of Pharmaceutics* 487.1-2 (2015), pp. 274–284. DOI: `10.1016/j.ijpharm.2015.04.051`.

[104] Mei Li Laracuente, Marina H. Yu and Kevin J. McHugh. 'Zero-order drug delivery: State of the art and future prospects'. *Journal of Controlled Release* 327 (2020), pp. 834–856. DOI: `10.1016/j.jconrel.2020.09.020`.

[105] Paarakh Padmaa et al. 'Release Kinetics - Concepts and Applications'. *International Journal of Pharmacy Research & Technology* 8 (2018), pp. 12–20. DOI: `10.31838/ijprt/08.01.02`.

[106] Nikolaos A. Peppas. 'Physiologically Responsive Hydrogels'. *Journal of Bioactive and Compatible Polymers* 6.3 (1991), pp. 241–246. DOI: `https://doi.org/10.1177/088391159100600303`.

[107] Takeru Higuchi. 'Mechanism of sustained-action medication. Theoretical analysis of rate of release of solid drugs dispersed in solid matrices'. *Journal of Pharmaceutical Sciences* 52.12 (1963), pp. 1145–1149. DOI: `10.1002/jps.2600521210`.

[108] Gautam Singhvi and Mahaveer Singh. 'In vitro Drug Release Characterization Models'. *International Journal of Pharmaceutical Studies and Research* 2.1 (2011), pp. 77–84. ISSN: 2229-4619.

[109] C. T. et al. Rueden. *ImageJ2: ImageJ for the next generation of scientific image data*. Last accessed 4 March 2023. 2023.

[110] San Jose California USA Systat Software Inc. *SigmaPlot Version 14.0*. 2023.

[111] The MathWorks Inc. *MATLAB*. 2023.

[112] Lake Shore Cryotronics. *PMC MicroMag 3900 Series VSM Specifications*. Last accessed 13 June 2023. 2023.

[113] International Commission on Non-Ionizing Radiation Protection et al. 'Guidelines on limits of exposure to static magnetic fields'. *Health Physics* 96.4 (2009), pp. 504–514. DOI: `10.1097/01.HP.0000343164.27920.4a`.

[114] Kaliyan Anandhan and Thilak Kumar. 'Synthesis, FTIR, UV-Vis and Photoluminescence characterizations of triethanolamine passivated CdO nanostructures'. *Spectrochimica Acta - Part A: Molecular and Biomolecular Spectroscopy* 149 (2015), pp. 476–480. DOI: `10.1016/j.saa.2015.04.035`.

[115] Perry Lim et al. ‘Study of interaction between cetyltrimethylammonium bromide and poly(acrylic acid) by rheological measurements’. *Journal of Physical Chemistry B* 107.26 (2003), pp. 6491–6496. DOI: `10.1021/jp027864m`.

Appendix A

Fourier Transformation Infrared Spectroscopy

This appendix contains the FTIR results of the synthesized NGs, for the purpose of comparing any differences in chemical groups for samples incorporated with different inorganic NPs. The observed peaks correspond to C-N bending at 1100-1200 cm^{-1}, $-\mathrm{CH}_2$ stretching vibration at 1300-1400 cm^{-1}, C=O stretching at 1600-1700 cm^{-1}, $-$COOH stretching at 1700-1800 cm^{-1}, and N$-$H stretching at 3200-3300 cm^{-1} [82].

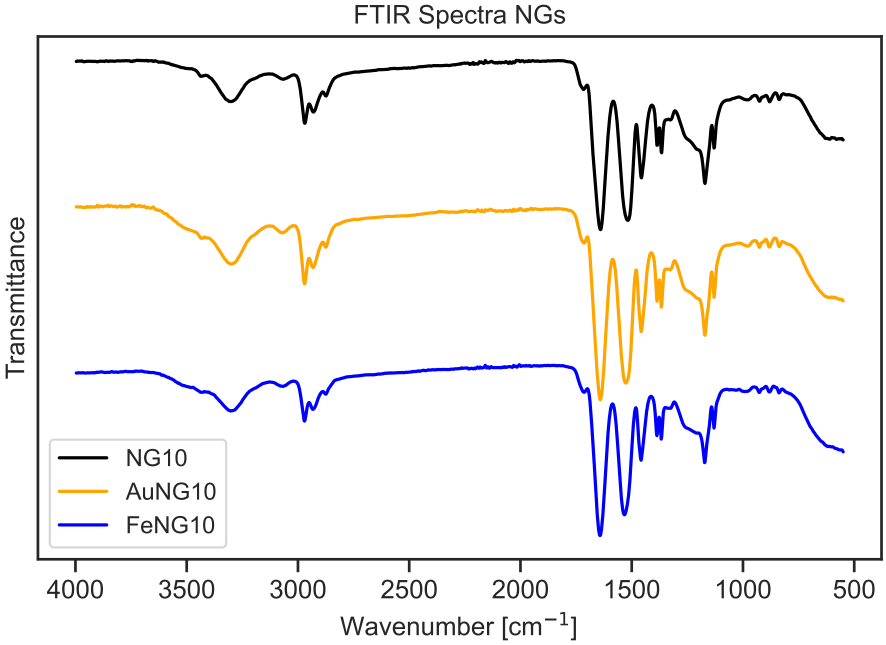

Figure A.1: FTIR spectra showing the transmission of NG10, AuER and AuNG10, and cNC and FeNG10 as a function of the wavenumber.

Appendix B

Scanning (Transmission) Electron Microscopy

This section provides additional data obtained using S(T)EM. Section B.1 presents additional micrographs of all the NP samples, and the histograms representing the measured particles used to calculate the L_{dry}, d_{dry}, and AR for the samples. Section B.2 provides the images obtained from the NG samples.

B.1 Nanoparticles

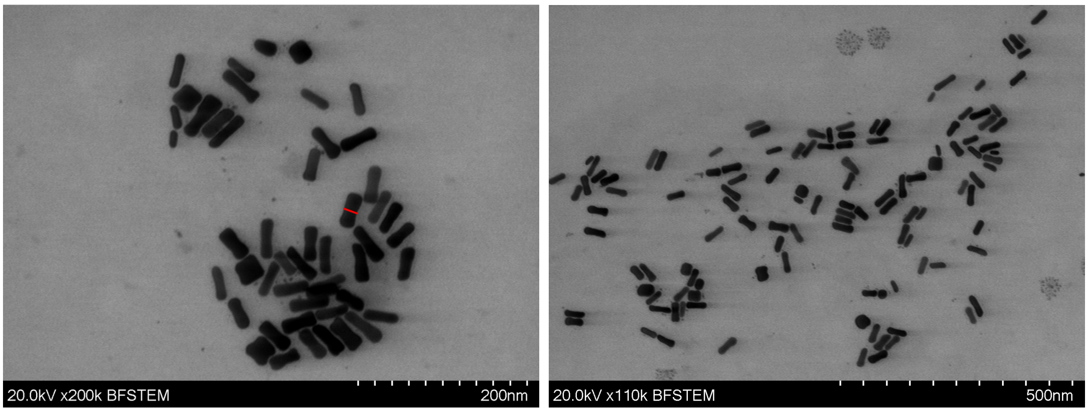

(a) (b)

Figure B.1: Additional S(T)EM micrographs of AuER. Figure a) shows how the diameter of the AuERs were measured, indicated by the red line.

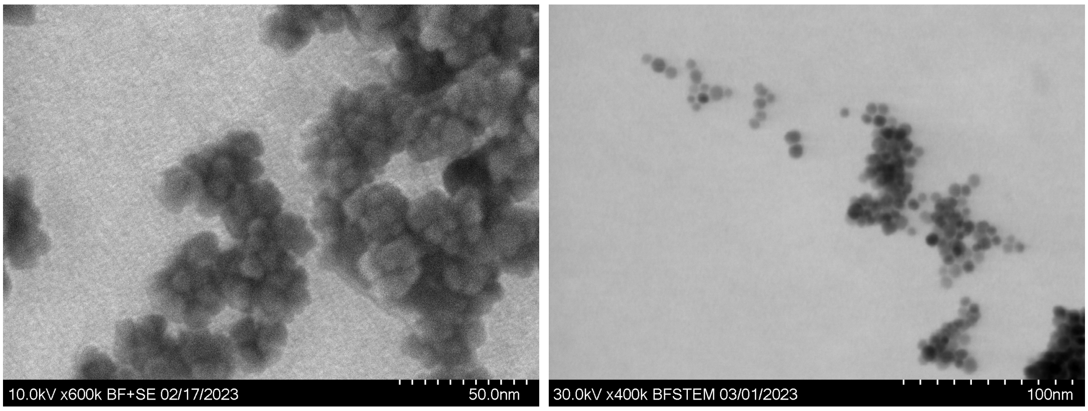

(a) (b)

Figure B.2: Additional S(T)EM micrographs of NS.

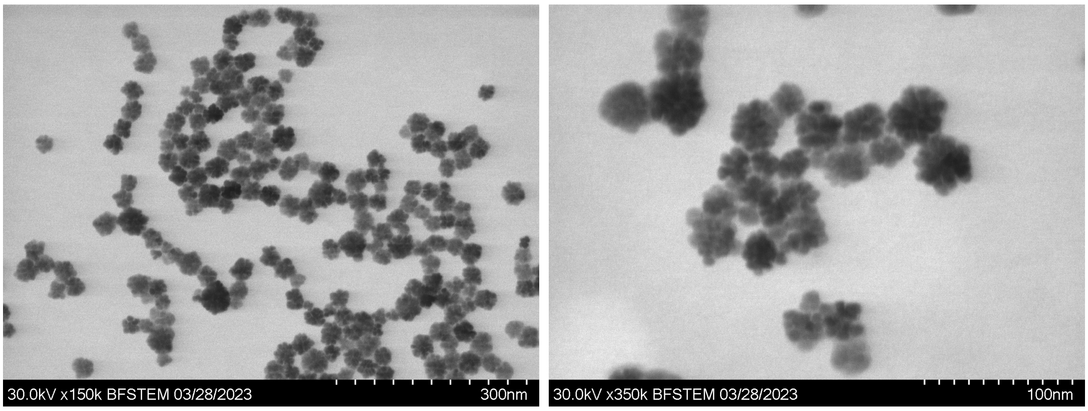

(a) (b)

Figure B.3: Additional S(T)EM micrographs of mNC.

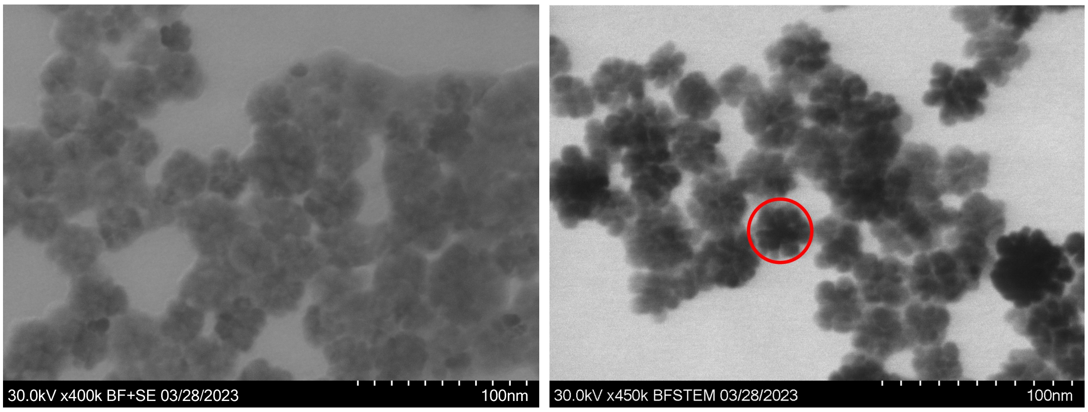

(a) (b)

Figure B.4: Additional S(T)EM micrographs of cNC. Figure b) shows how the diameter of the NCs were measured, indicated by a red circle.

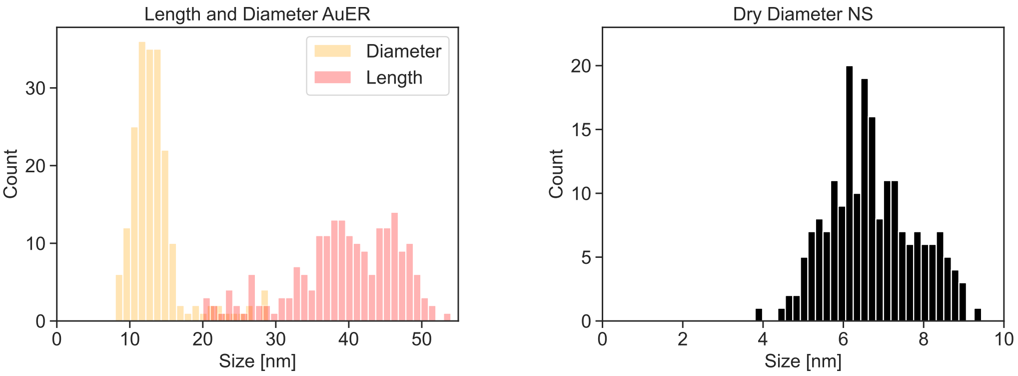

(a) AuER

(b) NS

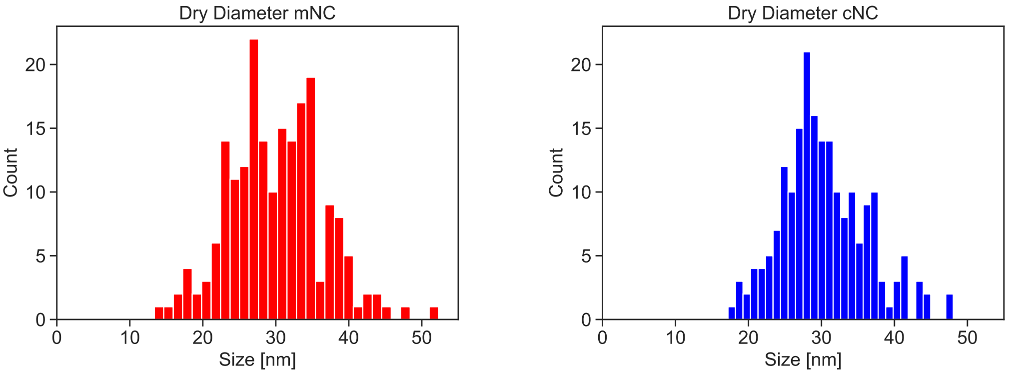

(c) mNC

(d) cNC

Figure B.5: Histograms illustrating the particle size distributions from S(T)EM images based on 200 particles per sample.

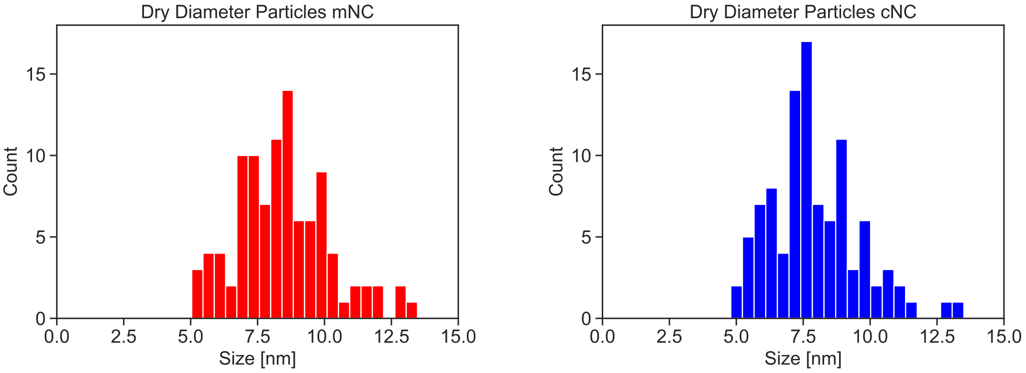

(a) Individual NPs mNC

(b) Individual NPs cNC

Figure B.6: Histograms showing the measured individual particles in the NCs based on 100 counted particles per sample.

B.2 Nanogels

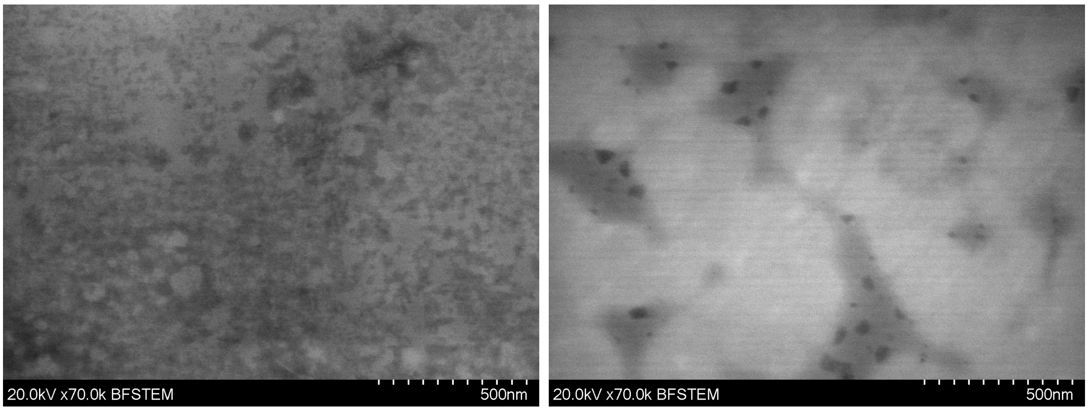

(a) NG10 (b) NG25

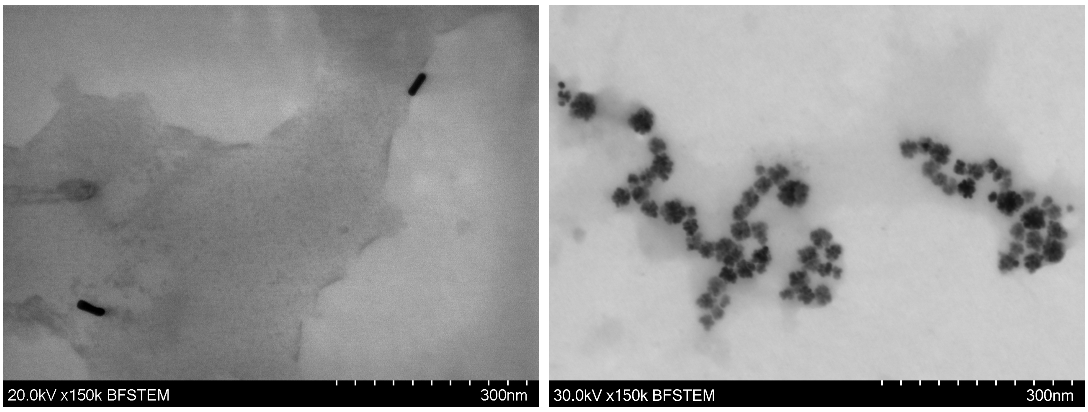

(c) AuNG10 (d) FeNG10

Figure B.7: S(T)EM images of NGs.

Appendix C

Vibrating Sample Magnetometer

This appendix provides additional information obtained using VSM. Section C.1 contains the normalized magnetization curves for the IONPs, used to compare the curve shapes. Section C.2 contains the fitted curves obtained for the Langevin function fitting of the magnetization curves.

C.1 Normalized Magnetization Curves

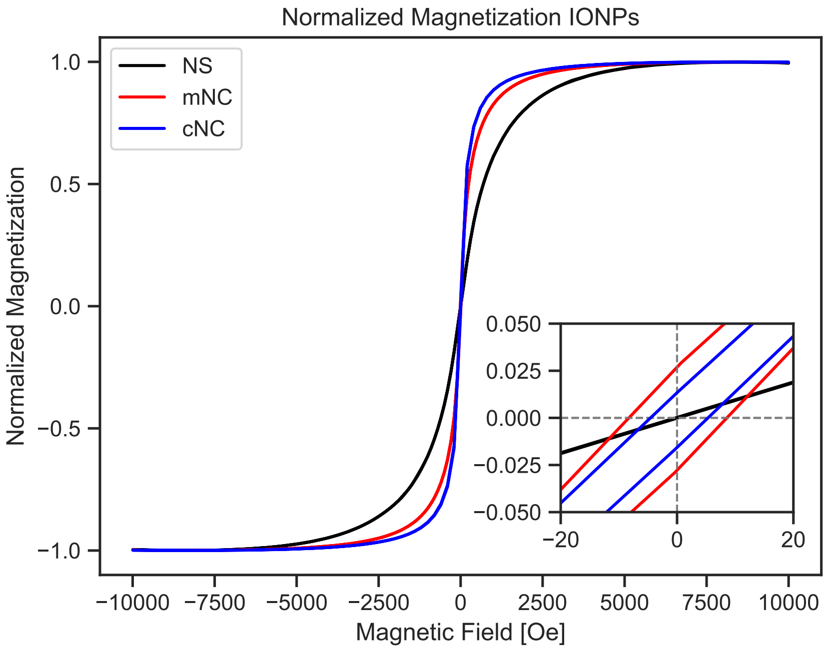

Figure C.1: Normalized magnetization curves for the IONPs.

C.2 Langevin Function Fitting

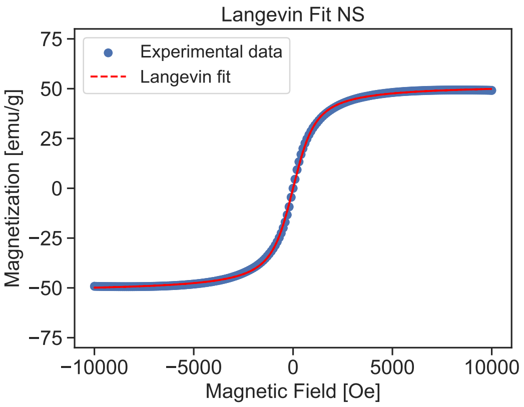

(a) NS

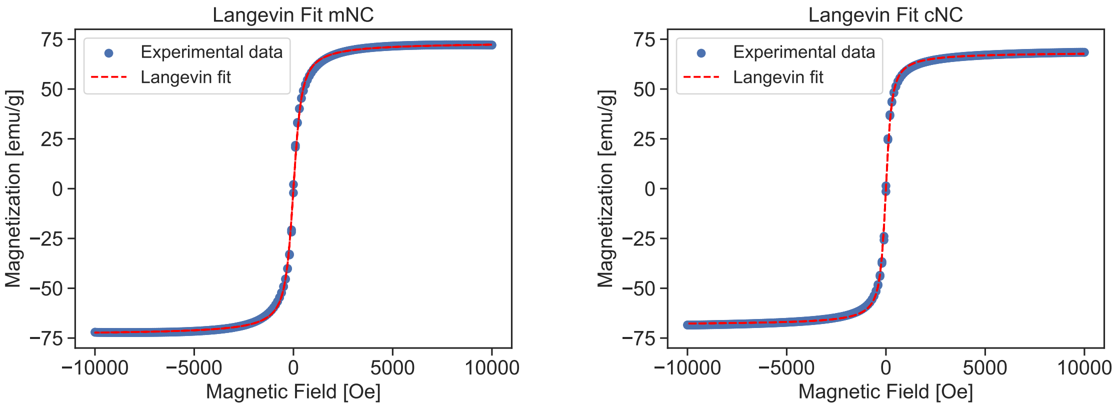

(b) mNC (c) cNC

Figure C.2: Curves obtained by Langevin fitting of the VSM measurements.

Appendix D

Dynamic Light Scattering

This appendix provides the additional information obtained using DLS. Section D.1 contains the hydrodynamic size distribution obtained for AuER. Section D.2 contains the swelling ratio as a function of temperature for the NG samples, used to determine the VPTT.

D.1 AuER Size Distribution

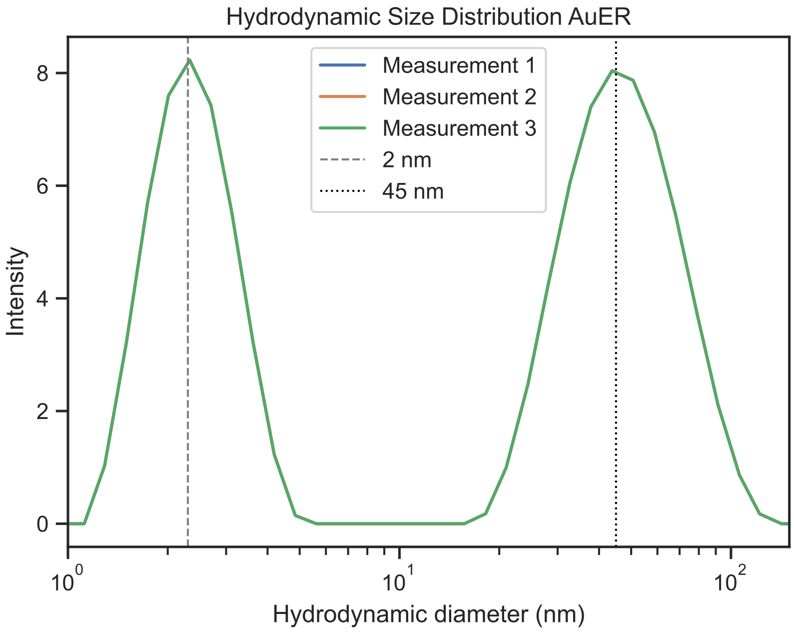

Figure D.1: Size distribution of AuER. Three measurements were formed, with identical distributions. Vertical lines indicate the size of the two observed distributions.

D.2 Volumetric Phase Transition Temperature

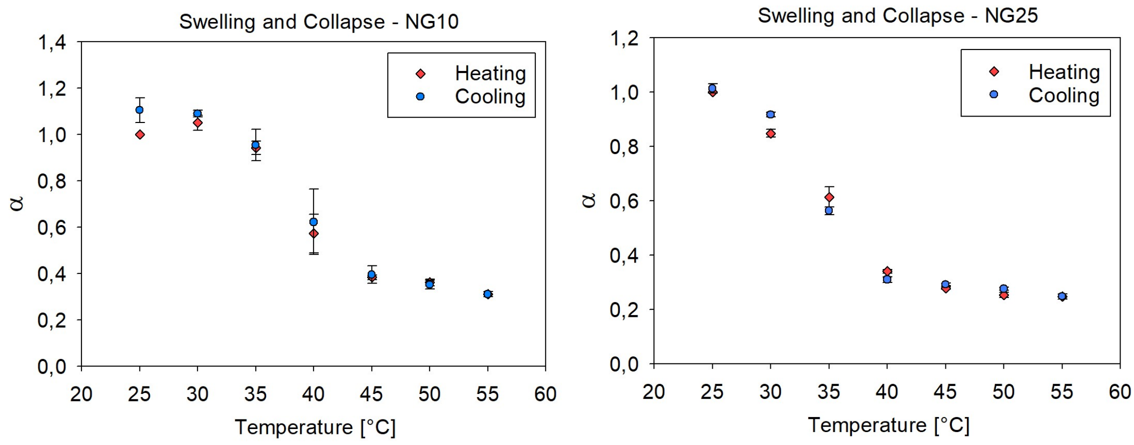

(a) NG10 (b) NG25

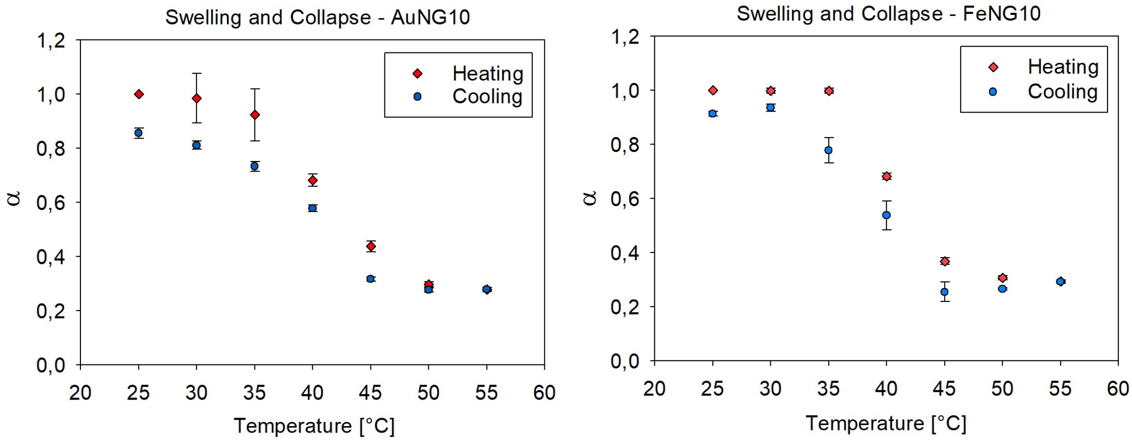

(c) AuNG10 (d) FeNG10

Figure D.2: Curves used to find the VPTT, using Equation 3.1. α is the swelling ratio.

Appendix E

Hyperthermia Studies

This appendix contains the additional information obtained for the hyperthermia measurements performed in the magneTherm. Section E.1 contains the calculated ILP values based on SAR, f, and H reported in the literature. Section E.2 contains the estimated relaxation times and hysteresis loss heating efficiency for the IONP samples.

E.1 Intrinsic Loss Power

Table E.1: The first three columns display the SAR values reported in the literature, together with the frequencies and fields used to obtain these values. The last column contains the ILP calculated from these values, using Equation 2.23 [73, 79]. Unni et al. and Kallumadil et al. reported their data using ILP, and are therefore not included in this table [65, 73].

Source	**SAR [W/g]**	**f [kHz]**	**H [kA/m]**	**ILP [nHm^{2}kg^{-1}]**
Maity [11]	500	240	89	0.26
Hergt [77]	1000	410	10	24.4
Hergt [77]	200	410	6.5	11.5
Narayanaswa [74]	146	766	28	0.24
Piñeiro-Redondo [75]	190	308	12	4.3

E.2 Approximated Relaxation Time and Hysteresis Loss

Table E.2: Approximated relaxation times were calculated from Equations 2.18, 2.17, and 2.19, using $\tau_0 = 10^{-10}$ s [68], $T = 310$ K, $K = 25$ kJ/m^3, and $\eta = 8.9 \cdot 10^{-4}$ kg/ms, along with the d_{dry} and d_{hyd} found from S(T)EM and DLS measurements [69]. $\omega \cdot \tau$ was found for 162 kHz. The SAR contribution from the hysteresis loss was approximated using M_R and H_C to estimate the hysteresis loop, and a frequency of 162 kHz [72].

Parameter	**NS**	**mNC**	**cNC**
τ_B [s]	$2.67 \cdot 10^{-2}$	$1.79 \cdot 10^{-1}$	$4.35 \cdot 10^{-4}$
τ_N [s]	$1.35 \cdot 10^{-7}$	$6.90 \cdot 10^{-6}$	$6.90 \cdot 10^{-7}$
τ [s]	$1.35 \cdot 10^{-7}$	$6.90 \cdot 10^{-6}$	$6.79 \cdot 10^{-6}$
$\omega \cdot \tau$	0.1	7.0	6.9
SAR$_{\text{hysteresis}}$ [W/g]	0	328	184

Appendix F

Drug Loading and Release Studies

This appendix provides the additional information obtained for the drug loading and release studies.

The first part contains results from additional drug loading experiments. Section F.1 contains the kinetic drug loading studies, where the absorbance was measured during the loading of the drugs to confirm that the absorbance of the loaded drugs remained the same as for the unloaded drugs. This data was used to confirm that the drug loading and release could be characterized by measuring the absorbance of the drug-loaded NGs. Section F.2 contains the drug loading for all the samples used in this work and the release study the sample was used for.

The second part contains results from additional drug release experiments. Section F.3 contains the calibration curve for SA obtained using the UV-vis connected to the magneTherm, which was used to calculate the release in the magneTherm release experiments. Section F.4 contains the kinetic studies of the drugs in a medium with pH 3 and a temperature of 45 °C. This data was used to confirm that the absorbance peak of the samples did not change in such a release medium. Finally, Sections F.5 and F.6 contain the additional drug release profiles obtained in the magneTherm and manual drug release studies. These figures were excluded from the results and discussion section as they did not provide any new information about the drug release.

F.1 Kinetic Study Drug Loading

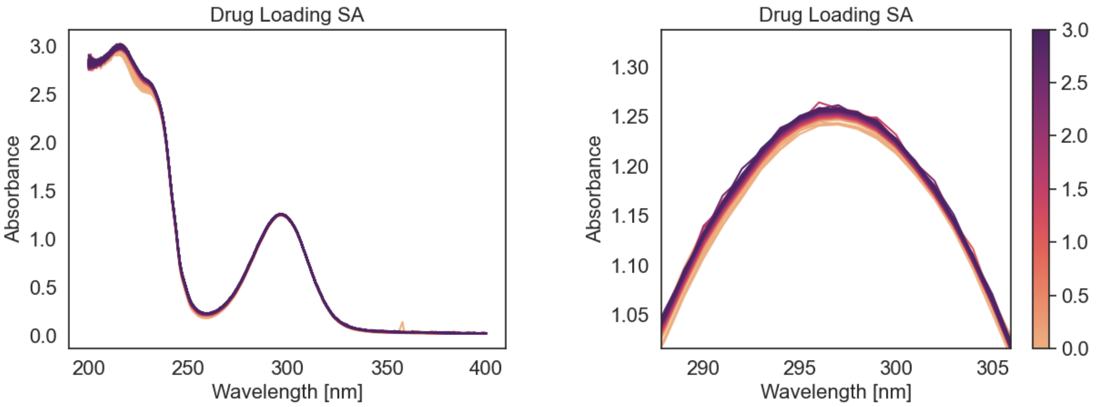

(a) Full spectrum

(b) Peak

Figure F.1: Kinetic absorbance during drug loading of SA. The measurement was performed for 3 hours, and the absorbance was measured every 30 seconds. 0.04 mg/mL of SA and 0.85 mg/mL of a NG was stirred at 800 rpm in the UV-Vis. The color goes from light to dark as the measurement passes, as shown in hours by the scale bar.

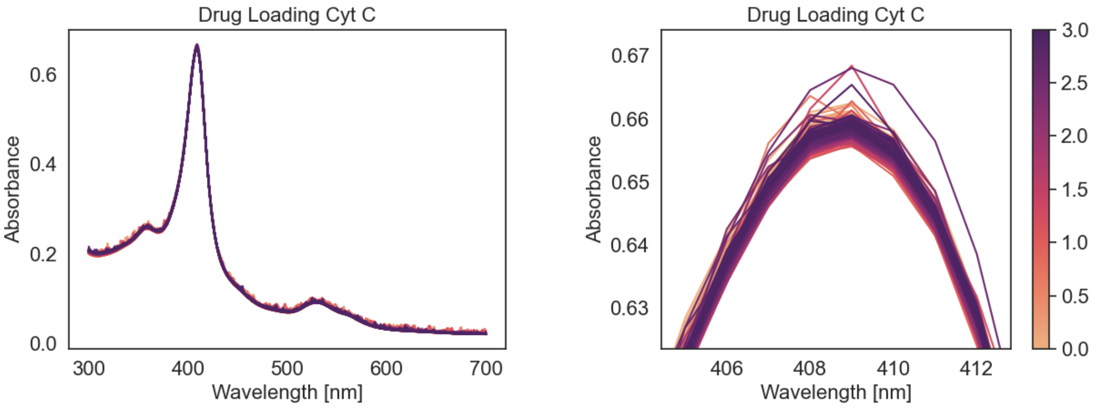

(a) Full spectrum

(b) Peak

Figure F.2: Kinetic absorbance during drug loading of Cyt C. The measurement was performed for 3 hours, and the absorbance was measured every 30 seconds. 0.1 mg/mL of Cyt C and 0.85 mg/mL of a NG was stirred at 800 rpm in the UV-Vis. The color goes from light to dark as the measurement passes, as shown in hours by the scale bar.

F.2 Complete Drug Loading

Table F.1: The complete drug loading results from the different NGs using different drugs. The drug concentration when loading was 1.5 mg/mL for SA and 0.5 mg/mL for Cyt C. LE and EE are calculated using Equations 2.24 and 2.25. The release study column shows the drug release study the sample used for. B indicates magnetic fields following the Brezovich limit, while I indicates magnetic fields following the Instrument limit. The R^2 indicates the goodness of fit of the release profile to a linear slope, i.e., zero-order release.

Sample	**Drug**	**LE [%]**	**EE [mg/mg]**	**Release Study**	$\boldsymbol{R^2}$
NG10	SA	28.7	0.51	magneTherm 25 °C pH 6	0.98
NG10	SA	17.1	0.30	magneTherm 25 °C pH 3	0.89
NG10	SA	16.8	0.28	magneTherm 45 °C pH 6	0.98
NG10	SA	21.9	0.39	magneTherm 45 °C pH 3	0.81
NG10	SA	27.5	0.41	manual 25 °C pH 6	0.92
NG10	SA	12.9	0.24	manual 25 °C pH 3	0.82
NG10	SA	12.7	0.22	manual 45 °C pH 6	0.88
NG10	SA	9.8	0.17	manual 45 °C pH 3	0.71
NG10	SA	17.9	0.30	manual pulsed	0.89
NG10	Cyt C	29.5	0.18	manual 25 °C pH 6	0.94
NG10	Cyt C	26.8	0.17	manual 25 °C pH 3	0.94
NG10	Cyt C	20.0	0.12	manual 45 °C pH 6	0.80
NG10	Cyt C	64.4	0.38	manual 45 °C pH 3	0.87
NG10	Cyt C	62.6	0.33	manual pulsed	0.95
NG25	SA	49.5	0.87	magneTherm 25 °C pH 6	0.90
NG25	SA	34.6	0.58	magneTherm 25 °C pH 3	0.89
NG25	SA	19.1	0.30	magneTherm 45 °C pH 6	0.98
NG25	SA	50.6	0.84	magneTherm 45 °C pH 3	0.87
NG25	SA	32.6	0.54	manual 25 °C pH 6	0.94
NG25	SA	12.7	0.20	manual 25 °C pH 3	0.89
NG25	SA	23.4	0.37	manual 45 °C pH 6	0.86
NG25	SA	41.8	0.71	manual 45 °C pH 3	0.83
NG25	SA	16.8	0.27	manual pulsed	0.83
NG25	Cyt C	52.9	0.27	manual 25 °C pH 6	0.93
NG25	Cyt C	22.5	0.13	manual 25 °C pH 3	0.96
NG25	Cyt C	15.2	0.09	manual 45 °C pH 6	0.98
NG25	Cyt C	67.2	0.37	manual 45 °C pH 3	0.97
NG25	Cyt C	19.7	0.09	manual pulsed	0.99

Table F.2

Sample	**Drug**	**LE [%]**	**EE [mg/mg]**	**Release Study**	**R^2**
AuNG10	SA	61.6	1.16	magneTherm 25 °C pH 6	0.94
AuNG10	SA	53.7	0.81	magneTherm 25 °C pH 3	0.86
AuNG10	SA	55.1	0.83	magneTherm 45 °C pH 6	0.98
AuNG10	SA	65.2	0.98	magneTherm 45 °C pH 3	0.89
AuNG10	SA	52.8	0.93	manual 25 °C pH 6	0.98
AuNG10	SA	61.9	1.09	manual 25 °C pH 3	0.89
AuNG10	SA	62.3	1.10	manual 45 °C pH 6	0.86
AuNG10	SA	61.7	1.16	manual 45 °C pH 3	0.84
AuNG10	SA	56.5	1.00	manual pulsed	0.94
AuNG10	Cyt C	37.7	0.20	manual 25 °C pH 6	0.99
AuNG10	Cyt C	32.1	0.16	manual 25 °C pH 3	0.98
AuNG10	Cyt C	27.9	0.14	manual 45 °C pH 6	0.95
AuNG10	Cyt C	12.7	0.06	manual 45 °C pH 3	0.97
AuNG10	Cyt C	37.3	0.20	manual pulsed	0.98
FeNG10	SA	16.6	0.26	magneTherm 25 °C pH 6	0.98
FeNG10	SA	17.3	0.29	magneTherm 25 °C pH 3	0.90
FeNG10	SA	39.1	0.69	magneTherm 45 °C pH 6	0.97
FeNG10	SA	19.9	0.31	magneTherm 45 °C pH 3	0.85
FeNG10	SA	52.5	0.93	magneTherm 37 °C pH 6	0.92
FeNG10	SA	54.2	0.96	magneTherm 37 °C pH 3	0.90
FeNG10	SA	46.8	0.83	magneTherm 25 °C pH 6 B	0.96
FeNG10	SA	51.5	0.91	magneTherm 25 °C pH 3 B	0.82
FeNG10	SA	23.8	0.42	magneTherm 25 °C pH 6 I	0.94
FeNG10	SA	17.8	0.27	magneTherm 25 °C pH 3 I	0.81
FeNG10	SA	29.5	0.52	magneTherm 37 °C pH 6 B	0.93
FeNG10	SA	15.8	0.24	magneTherm 37 °C pH 3 B	0.78
FeNG10	SA	53.0	0.84	magneTherm 37 °C pH 6 I	0.98
FeNG10	SA	53.8	0.95	magneTherm 37 °C pH 3 I	0.81
FeNG10	SA	51.3	0.91	magneTherm double conc. pH 6 I	0.99
FeNG10	SA	42.5	0.75	magneTherm double conc. pH 3 I	0.78
FeNG10	SA	55.0	0.97	manual 25 °C pH 6	0.90
FeNG10	SA	60.3	0.95	manual 25 °C pH 3	0.86
FeNG10	SA	35.2	0.41	manual 45 °C pH 6	0.84
FeNG10	SA	29.8	0.35	manual 45 °C pH 3	0.79
FeNG10	SA	43.7	0.73	manual pulsed	0.89
FeNG10	Cyt C	12.1	0.07	manual 25 °C pH 6	0.88
FeNG10	Cyt C	26.7	0.13	manual 25 °C pH 3	0.92
FeNG10	Cyt C	55.6	0.33	manual 45 °C pH 6	0.95
FeNG10	Cyt C	56.8	0.28	manual 45 °C pH 3	0.92
FeNG10	Cyt C	29.9	0.18	manual pulsed	0.98

F.3 Additional Calibration Curve magneTherm

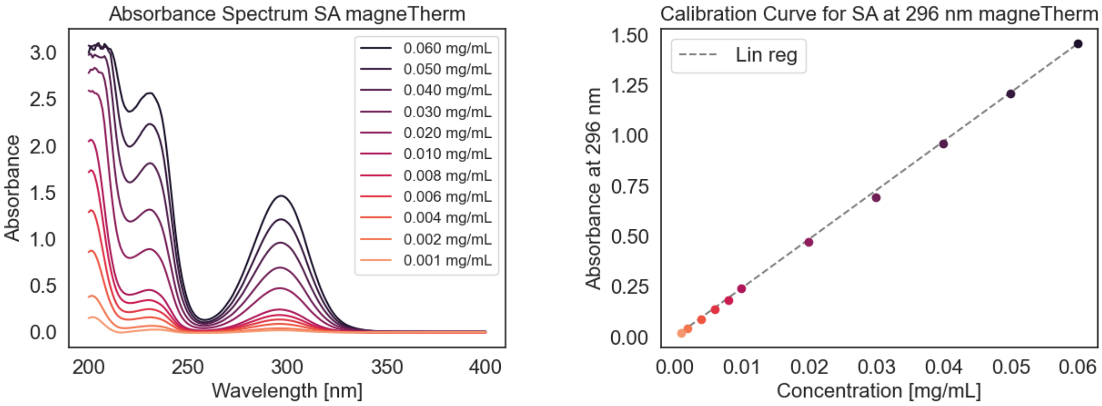

(a) Absorbance

(b) Calibration Curve

Figure F.3: Calibration curve SA magneTherm UV-vis. The slope was 24.28 and the R2 was 0.99.

F.4 Kinetic Study of Drugs at pH 3 and 45 °C

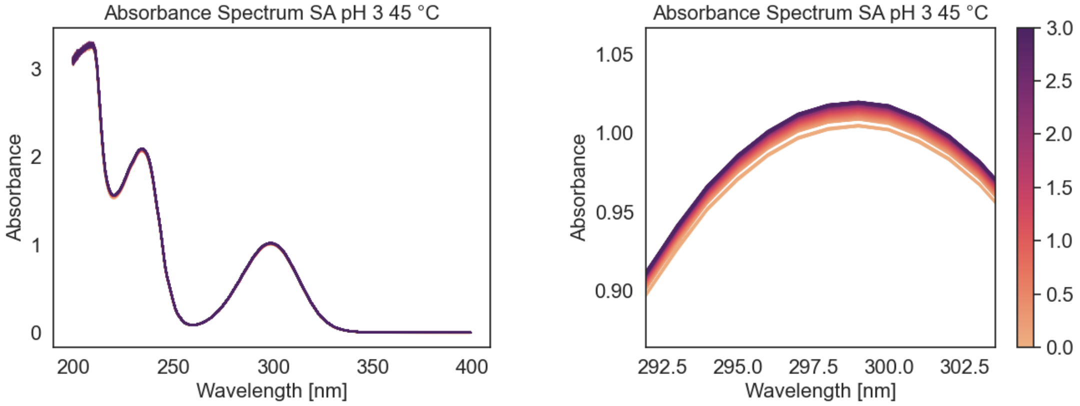

(a) Full spectrum

(b) Peak

Figure F.4: Kinetic study of 0.04 mg/mL SA at pH 3 and 45 °C. The measurement is performed for 3 hours, and the absorbance was measured every 30 seconds. Figure a) shows the full spectrum, while b) is zoomed in on the peak of SA, at 296 nm. The plot goes from light to dark, and the scale bar shows the time in hours.

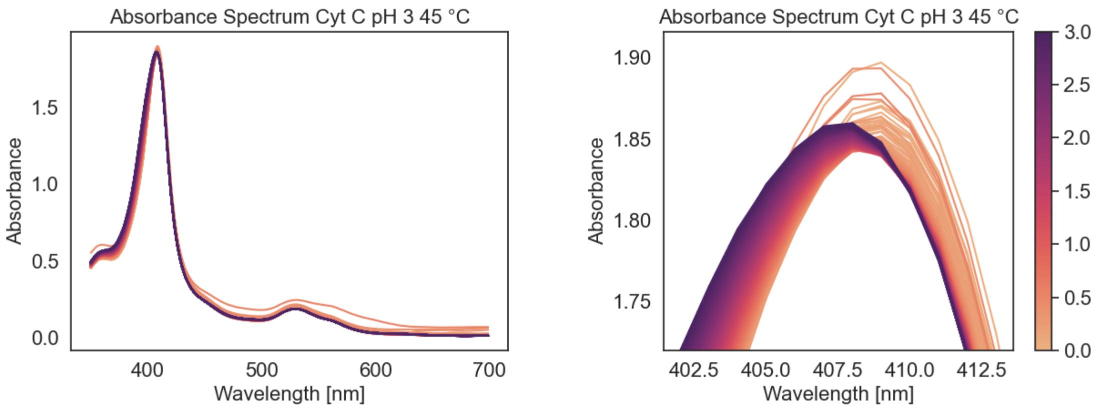

(a) Full spectrum

(b) Peak

Figure F.5: Kinetic study of 0.25 mg/mL Cyt C at pH 3 and 45 °C. The measurement is performed for 3 hours, and the absorbance was measured every 30 seconds. Figure a) shows the full spectrum, while b) is zoomed in on the peak of Cyt C, at 409 nm. The plot goes from light to dark, and the scale bar shows the time in hours.

F.5 Additional Release Results magneTherm

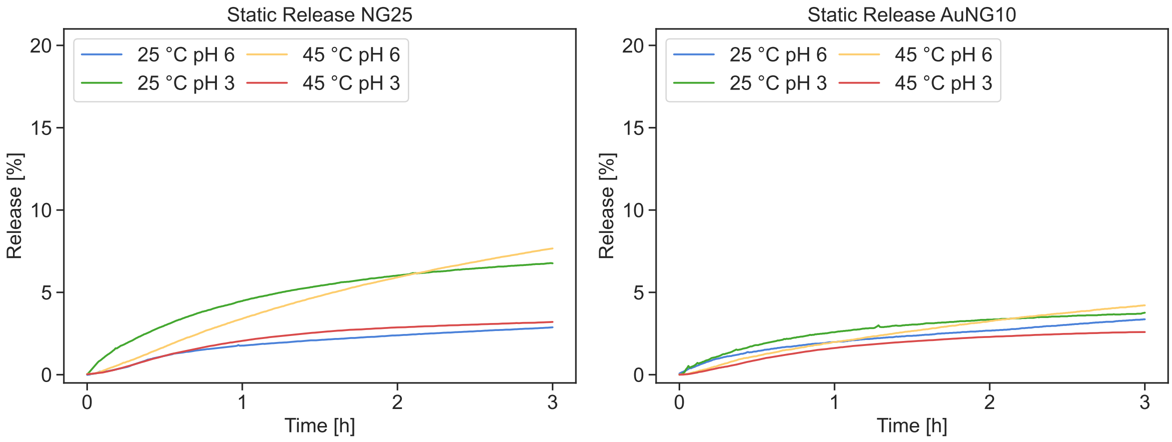

(a) NG25

(b) AuNG10

Figure F.6: mangeTherm release studies without application of an AMF for NG25 and AuNG10.

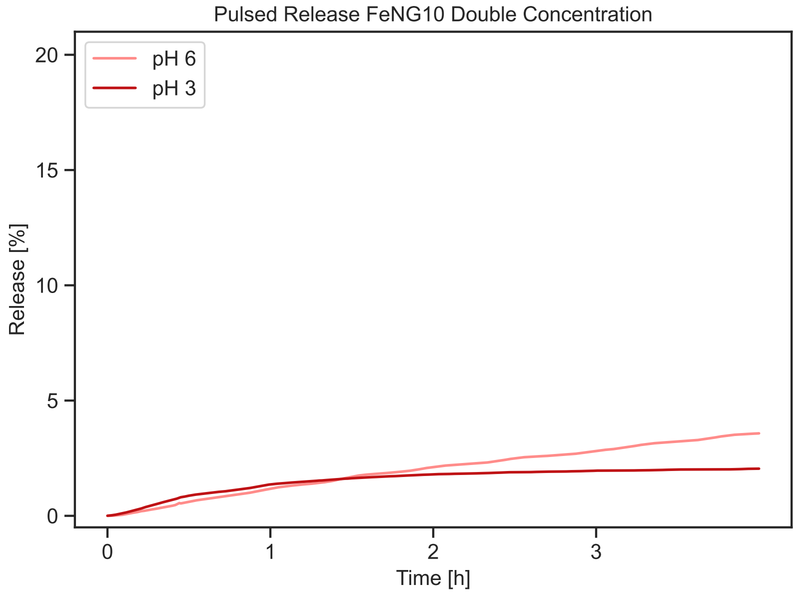

Figure F.7: Pulsed release conditions magneTherm, using FeNG10. The medium was 37 °C. An AMF was employed for 20 min at the time, with 10 min breaks between the exposures, and a field with 162 kHz and 190 Oe was used, i.e., using the Instrument limit.

F.6 Additional Release Results Manual

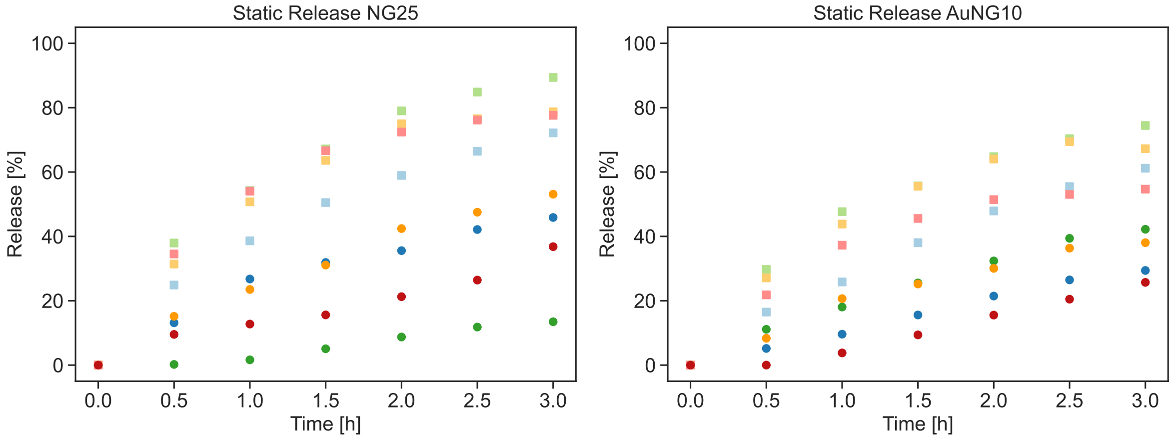

(a) NG25 (b) AuNG10

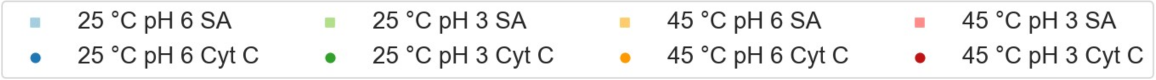

(c) Legend for all plots

Figure F.8: Static release experiments using the manual release method.

NTNU

Norwegian University of
Science and Technology